

NO-A179 908

WIDE AREA GUIDANCE AND CONTROL PROGRAM: INVESTIGATION
OF SCANNING IR SEEK. (U) JOHNS HOPKINS UNIV LAUREL MD
APPLIED PHYSICS LAB L M HOWSER NOV 86 JHU/APL/TG-1360

14

UNCLASSIFIED

NO0024-85-C-5301

ML



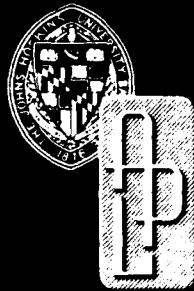
MI
P.

DTIC FILE COPY

12

JHU/APL
TG 1360
DECEMBER 1986
Copy No.

AD-A179 908



Technical Memorandum

**WIDE AREA GUIDANCE
AND CONTROL PROGRAM:
INVESTIGATION OF SCANNING IR SEEKER
PERFORMANCE IN BACKGROUND CLUTTER**

L.M. HOWSER

DTIC
ELECTE
APR 29 1987
S E D

THE JOHNS HOPKINS UNIVERSITY ■ APPLIED PHYSICS LABORATORY

Approved for public release: Distribution is unlimited.

87 4 26 001

JHU/APL

TG 1360

DECEMBER 1986

Technical Memorandum

**WIDE AREA GUIDANCE
AND CONTROL PROGRAM:
INVESTIGATION OF SCANNING IR SEEKER
PERFORMANCE IN BACKGROUND CLUTTER**

L.M. HOWSER

THE JOHNS HOPKINS UNIVERSITY ■ APPLIED PHYSICS LABORATORY
Johns Hopkins Road, Laurel, Maryland 20707
Operating under Contract N00024-35-C-5301 with the Department of the Navy

Approved for public release: Distribution is unlimited.

UNCLASSIFIED

SECURITY CLASSIFICATION OF THIS PAGE

REPORT DOCUMENTATION PAGE

1a. REPORT SECURITY CLASSIFICATION UNCLASSIFIED			1b. RESTRICTIVE MARKINGS		
2a. SECURITY CLASSIFICATION AUTHORITY			3. DISTRIBUTION/AVAILABILITY OF REPORT Approved for public release; distribution unlimited.		
2b. DECLASSIFICATION/DOWNGRADING SCHEDULE					
4. PERFORMING ORGANIZATION NUMBER(S) JHU/APL TG 1360			5. MONITORING ORGANIZATION REPORT NUMBER(S) JHU/APL TG 1360		
6a. NAME OF PERFORMING ORGANIZATION The Johns Hopkins University Applied Physics Laboratory		6b. OFFICE SYMBOL (If Applicable) TIR	7a. NAME OF MONITORING ORGANIZATION NAVPRO, Laurel, Maryland		
6c. ADDRESS (City, State, and ZIP Code) Johns Hopkins Road Laurel, Maryland 20707		7b. ADDRESS (City, State, and ZIP Code) Johns Hopkins Road Laurel, Maryland 20707			
8a. NAME OF FUNDING/SPONSORING ORGANIZATION Naval Surface Weapons Center		8b. OFFICE SYMBOL (If Applicable) G06	9. PROCUREMENT INSTRUMENT IDENTIFICATION NUMBER N00024-85-C-5301		
8c. ADDRESS (City, State, and ZIP Code) Dahlgren, VA 22448		10. SOURCE OF FUNDING NUMBERS			
		PROGRAM ELEMENT NO.	PROJECT NO.	TASK NO. A3D0	WORK UNIT ACCESSION NO.
11. TITLE (Include Security Classification) Wide Area Guidance and Control Program: Investigation of Scanning IR Seeker Performance in Background Clutter					
12. PERSONAL AUTHOR(S) Howser, L. M.					
13a. TYPE OF REPORT Technical Memorandum		13b. TIME COVERED FROM _____ TO _____		14. DATE OF REPORT (Year, Month, Day) 1986, November	15. PAGE COUNT 72
16. SUPPLEMENTARY NOTATION					
17. COSATI CODES			18. SUBJECT TERMS		
FIELD	GROUP	SUB-GROUP	Advanced, scanning IR seeker Clutter-limited performance Digital filtering		
			Pulse discrimination Point target detection		
19. ABSTRACT (Continue on reverse if necessary and identify by block number)					
<p>The clutter-limited performance of an advanced, scanning infrared seeker is investigated. A survey of infrared imagery lists data available for this investigation. Requirements of the study restrict the choice of imagery; three background-image data sets from Air Force and Navy collection programs are used. Artifacts in the selected data are examined and correction techniques are developed. The images are characterized by radiance statistics and power spectral densities. Detailed information on the data collection instruments and the scenes used are presented in appendixes.</p> <p>Seeker performance is determined using a number of techniques. Performance is measured both in terms of the required target irradiance and the false-alarm rate produced by the background scene. The three techniques compared are a matched-filter analysis using the image power spectral densities, a one-dimensional digital filter that approximates the matched filter, and the digital filter followed by a pulse-width discriminator. Finally, a cross-scan comparison between the output of adjacent channels is shown to be useful in further rejecting extended background features. Implementation of the final algorithm in a missile seeker is discussed.</p>					
20. DISTRIBUTION/AVAILABILITY OF ABSTRACT <input checked="" type="checkbox"/> UNCLASSIFIED/UNLIMITED <input type="checkbox"/> SAME AS RPT. <input type="checkbox"/> DTIC USERS			21. ABSTRACT SECURITY CLASSIFICATION UNCLASSIFIED		
22a. NAME OF RESPONSIBLE INDIVIDUAL NAVPRO Security Officer			22b. TELEPHONE (Include Area Code) (301) 953-5403		22c. OFFICE SYMBOL NAVPRO SE

ABSTRACT

The clutter-limited performance of an advanced, scanning infrared seeker is investigated. A survey of infrared imagery lists data available for this investigation. Requirements of the study restrict the choice of imagery; three background-image data sets from Air Force and Navy collection programs are used. Artifacts in the selected data are examined and correction techniques are developed. The images are characterized by radiance statistics and power spectral densities. Detailed information on the data collection instruments and the scenes used are presented in appendixes.

Seeker performance is determined using a number of techniques. Performance is measured both in terms of the required target irradiance and the false-alarm rate produced by the background scene. The three techniques compared are a matched-filter analysis using the image power spectral densities, a one-dimensional digital filter that approximates the matched filter, and the digital filter followed by a pulse-width discriminator. Finally, a cross-scan comparison between the output of adjacent channels is shown to be useful in further rejecting extended background features. Implementation of the final algorithm in a missile seeker is discussed.

Accession For	
NTIS GRA&I	<input checked="" type="checkbox"/>
DTIC TAB	<input type="checkbox"/>
Unannounced	<input type="checkbox"/>
Justification	
By	
Distribution/	
Availability Codes	
Dist	Avail and/or Special
A-1	



1 2 3 4 5 6 7 8 9 10 11 12 13 14 15 16 17 18 19 20 21 22 23 24 25 26 27 28 29 30 31 32 33 34 35 36 37 38 39 40 41 42 43 44 45 46 47 48 49 50 51 52 53 54 55 56 57 58 59 60 61 62 63 64 65 66 67 68 69 70 71 72 73 74 75 76 77 78 79 80 81 82 83 84 85 86 87 88 89 90 91 92 93 94 95 96 97 98 99 100 101 102 103 104 105 106 107 108 109 110 111 112 113 114 115 116 117 118 119 120 121 122 123 124 125 126 127 128 129 130 131 132 133 134 135 136 137 138 139 140 141 142 143 144 145 146 147 148 149 150 151 152 153 154 155 156 157 158 159 160 161 162 163 164 165 166 167 168 169 170 171 172 173 174 175 176 177 178 179 180 181 182 183 184 185 186 187 188 189 190 191 192 193 194 195 196 197 198 199 200 201 202 203 204 205 206 207 208 209 210 211 212 213 214 215 216 217 218 219 220 221 222 223 224 225 226 227 228 229 230 231 232 233 234 235 236 237 238 239 240 241 242 243 244 245 246 247 248 249 250 251 252 253 254 255 256 257 258 259 260 261 262 263 264 265 266 267 268 269 270 271 272 273 274 275 276 277 278 279 280 281 282 283 284 285 286 287 288 289 290 291 292 293 294 295 296 297 298 299 300 301 302 303 304 305 306 307 308 309 310 311 312 313 314 315 316 317 318 319 320 321 322 323 324 325 326 327 328 329 330 331 332 333 334 335 336 337 338 339 340 341 342 343 344 345 346 347 348 349 350 351 352 353 354 355 356 357 358 359 360 361 362 363 364 365 366 367 368 369 370 371 372 373 374 375 376 377 378 379 380 381 382 383 384 385 386 387 388 389 390 391 392 393 394 395 396 397 398 399 400 401 402 403 404 405 406 407 408 409 410 411 412 413 414 415 416 417 418 419 420 421 422 423 424 425 426 427 428 429 430 431 432 433 434 435 436 437 438 439 440 441 442 443 444 445 446 447 448 449 450 451 452 453 454 455 456 457 458 459 460 461 462 463 464 465 466 467 468 469 470 471 472 473 474 475 476 477 478 479 480 481 482 483 484 485 486 487 488 489 490 491 492 493 494 495 496 497 498 499 500 501 502 503 504 505 506 507 508 509 510 511 512 513 514 515 516 517 518 519 520 521 522 523 524 525 526 527 528 529 530 531 532 533 534 535 536 537 538 539 540 541 542 543 544 545 546 547 548 549 550 551 552 553 554 555 556 557 558 559 560 561 562 563 564 565 566 567 568 569 570 571 572 573 574 575 576 577 578 579 580 581 582 583 584 585 586 587 588 589 590 591 592 593 594 595 596 597 598 599 600 601 602 603 604 605 606 607 608 609 610 611 612 613 614 615 616 617 618 619 620 621 622 623 624 625 626 627 628 629 630 631 632 633 634 635 636 637 638 639 640 641 642 643 644 645 646 647 648 649 650 651 652 653 654 655 656 657 658 659 660 661 662 663 664 665 666 667 668 669 670 671 672 673 674 675 676 677 678 679 680 681 682 683 684 685 686 687 688 689 690 691 692 693 694 695 696 697 698 699 700 701 702 703 704 705 706 707 708 709 710 711 712 713 714 715 716 717 718 719 720 721 722 723 724 725 726 727 728 729 730 731 732 733 734 735 736 737 738 739 740 741 742 743 744 745 746 747 748 749 750 751 752 753 754 755 756 757 758 759 760 761 762 763 764 765 766 767 768 769 770 771 772 773 774 775 776 777 778 779 780 781 782 783 784 785 786 787 788 789 790 791 792 793 794 795 796 797 798 799 800 801 802 803 804 805 806 807 808 809 810 811 812 813 814 815 816 817 818 819 820 821 822 823 824 825 826 827 828 829 830 831 832 833 834 835 836 837 838 839 840 841 842 843 844 845 846 847 848 849 850 851 852 853 854 855 856 857 858 859 860 861 862 863 864 865 866 867 868 869 870 871 872 873 874 875 876 877 878 879 880 881 882 883 884 885 886 887 888 889 890 891 892 893 894 895 896 897 898 899 900 901 902 903 904 905 906 907 908 909 910 911 912 913 914 915 916 917 918 919 920 921 922 923 924 925 926 927 928 929 930 931 932 933 934 935 936 937 938 939 940 941 942 943 944 945 946 947 948 949 950 951 952 953 954 955 956 957 958 959 960 961 962 963 964 965 966 967 968 969 970 971 972 973 974 975 976 977 978 979 980 981 982 983 984 985 986 987 988 989 990 991 992 993 994 995 996 997 998 999 1000 1001 1002 1003 1004 1005 1006 1007 1008 1009 1010 1011 1012 1013 1014 1015 1016 1017 1018 1019 1020 1021 1022 1023 1024 1025 1026 1027 1028 1029 1030 1031 1032 1033 1034 1035 1036 1037 1038 1039 1040 1

CONTENTS

List of Figures.....	6
List of Tables.....	7
1.0 Introduction.....	9
1.1 Background.....	9
1.2 Missile Infrared Seekers.....	9
1.3 Approach to Algorithm Development.....	10
2.0 Background Data.....	11
2.1 Data Requirements.....	11
2.2 Data Survey.....	11
2.3 Selected Data.....	14
3.0 Characterization of Data.....	19
3.1 Data Artifacts and Corrections.....	19
3.2 Radiance Statistics.....	20
3.3 Power Spectral Density.....	20
4.0 Scene Clutter Processing.....	24
4.1 Approach.....	24
4.2 Matched-Filter Performance Analysis.....	25
4.3 Digital-Filter Performance Analysis.....	28
4.4 Filtering and Pulse Discrimination Performance Analysis.....	33
4.5 Cross-Scan Comparison.....	43
4.6 Comparison of Processing Techniques.....	43
4.7 Implementation of the Scanning Sensor Processing.....	48
5.0 Conclusions.....	49
References.....	51
Appendix A: BMAP Data Description.....	52
Appendix B: AFGL Data Description.....	56
Appendix C: ERIM Data Description.....	60
Appendix D: Power Spectral Density of Background Data.....	65
Appendix E: Power Spectral Density of Filtered Scenes.....	69

LIST OF FIGURES

1. Images from each of the sets of data used in this study.....	17
2. Image showing bad data in ERIM scene S23CH2.....	20
3. Power spectral density of BMAP Montauk Point middle- wavelength and long-wavelength background data.....	22
4. Power spectral density of AFGL cloud and terrain background scene I05.....	22
5. Power spectral density of ERIM Port Hueneme scene in 2.0 to 2.6 μm spectral band (scene S23CH1).....	22
6. Fourier transform of point source as seen by the BMAP instrument.....	23
7. Required target irradiance for detection as a function of seeker resolution for AFGL and BMAP data.....	27
8. Comparison of required target irradiance for ideal band- pass filters to the matched-filter result using BMAP data.....	28
9. BMAP bandpass filter: second-order low-pass and first-order high-pass (corner = 1.5 cycles/mrad).....	29
10. AFGL first-order high-pass filter (cut-on = 0.25 cycle/mrad).....	29
11. ERIM first-order high-pass filter (cut-on = 0.1 cycle/mrad).....	30
12. Power spectral density of BMAP Montauk Point long-wave- length background data after bandpass filter.....	30
13. Power spectral density of AFGL cloud and terrain back- ground scene I05 after high-pass filter.....	30
14. Power spectral density of ERIM Port Hueneme scene in 2.0 to 2.6 μm spectral band (scene S23CH1) after high-pass filter.....	31
15. Line 471 of ERIM Camp A.P. Hill morning scene in 2.0 to 2.6 μm spectral band (scene S01CH1).....	31
16. Line 471 of ERIM Camp A.P. Hill morning scene in 8.0 to 14.0 μm spectral band (scene S01CH3).....	31
17. Images after filter and threshold.....	34
18. Pulse width discrimination algorithm for BMAP data.....	35
19. Line 1 of BMAP Montauk Point long-wavelength back- ground data.....	37
20. Typical derived NE Δ T values for the ERIM M-7 line scanner.....	39
21. Images after filter, pulse discrimination, and threshold.....	42
22. Comparison of processing techniques.....	45
23. Histograms of BMAP mid-IR Bedford scene.....	46
24. Cumulative histograms showing reduction of maximum irradiance and NEI from filtering and pulse discrimination.....	46
25. Lines of images from ERIM Port Hueneme scene in 4.5 to 5.5 μm spectral band (scene S23CH3) showing bad scan lines.....	47
26. Implementation of the scanning sensor processing.....	48
A-1. Spectral response of BMAP mid- and long-wave channels.....	54
A-2. Point-source response of BMAP detector channels.....	54
B-1. Spectral response of AFGL FLIR with 7.84 to 13.16 μm filter.....	59
C-1. Spectral characteristics of ERIM M-7 detector channels.....	63

D-1. Power spectral densities of AFGL scenes, 7.84 to 13.16 μm spectral band (0.5 mrad sample size).....	65
D-2. Power spectral densities of AFGL scenes, 7.84 to 13.16 μm spectral band (0.1 mrad sample size).....	65
D-3. Power spectral densities of ERIM scenes of Camp A.P. Hill, 2.0 to 2.6 μm spectral band.....	66
D-4. Power spectral densities of ERIM scenes of Camp A.P. Hill, 4.5 to 5.5 μm spectral band.....	66
D-5. Power spectral densities of ERIM scenes of Camp A.P. Hill, 8.0 to 14.0 μm spectral band.....	67
D-6. Power spectral densities of ERIM scenes of Port Hueneme (port and water).....	67
D-7. Power spectral densities of ERIM scenes of Port Hueneme (port, water, and sun).....	68
D-8. Power spectral densities of ERIM scenes of mountains near Nellis AFB (F08).....	68
E-1. Power spectral density of BMAP mid-IR scene from Montauk Point after bandpass filter.....	69
E-2. Power spectral density of AFGL terrain scene (104) after high-pass filter.....	69
E-3. Power spectral densities of ERIM afternoon scene of Camp A.P. Hill after high-pass filter.....	70
E-4. Power spectral density of ERIM scene of Port Hueneme, spectral band 4.5 to 5.5 μm , after high-pass filter (scene S23CH3).....	70

LIST OF TABLES

1. Requirements for wide-area missile IR background data.....	12
2. Summary of available background data.....	13
3. Characteristics of instruments used to collect background data used in this study.....	16
4. Summary of data used in this study.....	18
5. Statistics of background data in units of $\text{W}/\text{cm}^2/\text{sr}$	21
6. PSD noise level.....	23
7. Required target irradiance for matched filter detection in several AFGL cloud scenes.....	26
8. Digital filters used in the performance analysis.....	29
9. Statistics of background data after filtering in units of $\text{W}/\text{cm}^2/\text{sr}$	32
10. Thresholds used in Fig. 17.....	35
11. Results of processing impulses with BMAP filters.....	36
12. Results of processing impulses with AFGL filter.....	38
13. Thresholds of AFGL images for pulse discrimination.....	38
14. Results of processing impulses with ERIM filter.....	39
15. ERIM NEIs and thresholds.....	40
16. Pulse discrimination parameters.....	40
17. Statistics of data after filtering and pulse discrimination in units of $\text{W}/\text{cm}^2/\text{sr}$	41
18. Filtering output-to-input ratios.....	43
19. Minimum detectable signal in units of $\text{W}/\text{cm}^2/\text{sr}$	44

A-1. Characteristics of the BMAP dual-band IR measurement system.....	53
A-2. Summary of BMAP data.....	55
B-1. Characteristics of the AFGL-FLIR.....	56
B-2. Summary of AFGL infrared imagery characteristics.....	57
B-3. Calibration and spectral band data for AFGL infrared imagery.....	58
C-1. Characteristics of the ERIM M-7 scanner.....	60
C-2. Summary of ERIM infrared imagery characteristics.....	61
C-3. Calibration and spatial registration for ERIM infrared imagery.....	62
C-4. ERIM middle-infrared detector arrays.....	64

1.0 INTRODUCTION

1.1 Background

Advanced antiair missile guidance systems will make extensive use of infrared (IR) sensors to counter radar cross-section reduction and standoff jamming, to achieve lower miss distance, and to increase high-altitude missile dynamic performance. IR sensors will also provide an added discrimination capability to defeat self-screening countermeasures and select targets from closely spaced formations. The Wide-Area Guidance and Control Program is tasked with developing guidance technology for use in advanced, long-range, surface-to-air missiles (SAM). Such missiles must be "self-targeting," that is, the missile guidance conducts wide-field angle search to compensate for poor targeting (i.e., midcourse flight) accuracy against long-range targets. While advances in detector technology potentially offer very sensitive IR seeker systems, detection performance will most likely be limited by the background clutter.

An investigation of clutter-imposed limitations to missile IR seeker performance is being conducted to determine the likely performance of a guidance sensor that could be used on long-range SAMs. The objective of this effort is to develop clutter processing algorithms and to apply those processing techniques to data in order to determine the clutter-limited performance of advanced IR seekers. The principal clutter processing technique investigated here is a combination of digital filtering followed by a pulse discrimination algorithm.

1.2 Missile Infrared Seekers

A long-range SAM with IR guidance has several unique requirements that dictate the choice of signal processing. First, an IR seeker must acquire and track the target autonomously. Potential false alarms, if not immediately rejected, result in the waste of an expensive missile. Second, an IR seeker must be capable of rapid, wide-field search to compensate for significant targeting and midcourse guidance errors that may occur when targets are engaged at long range. Third, the long-range nature of the missile requires sufficient seeker acquisition range to acquire targets from the optimum flight altitude to allow time for descent to target altitude. Hence, the capability to detect small signature targets in terrain and cloud background clutter at long range is crucial for mission success.

Achievement of high IR seeker performance will become significantly more important as enemy capabil-

ities evolve. Autonomous IR seeker acquisition becomes more important as target radar cross section is reduced and the IR mode assumes greater initial detection responsibility. Initially, the IR seeker will have primary acquisition responsibility against high-speed, higher altitude (i.e., higher IR signature) targets with the missile seeker radar having the primary responsibility for detecting lower speed and lower altitude (i.e., lower IR signature) targets. Ultimately, an IR seeker capability against low-signature targets is desired.

Because of the severity of the targeting and midcourse guidance requirements for a long-range mission, the enemy will develop tactics and electronic countermeasures (ECM) to degrade these functions. As targeting and midcourse guidance quality is reduced, the search capability of all missile guidance modes must be increased. Increases in the size of the search field of regard, the search angular scan rate, and acquisition range are needed to offset the effects of poorer target localization. The long-range missile must have acquisition and intercept capability even in situations when target range is unknown or external communications (for midcourse guidance) are lost. Uncertainties in range also require longer search time, hence a lower false-alarm rate.

As external targeting becomes poorer, particularly when target range information is degraded or unavailable, the need for the missile to fly a propulsion-efficient trajectory increases. Since propulsion-efficient trajectories result in high-altitude flight, range to potential targets is increased. The increased range requirement, coupled with the need for more search capability and the need to detect lower signature targets, results in an IR seeker requirement for significantly greater sensitivity.

Advances in detector technology offer large increases in sensor sensitivity, e.g., two orders of magnitude over current systems. Increased IR sensitivity offers the potential for the needed long-range detection of low-signature targets. However, actual capability depends on the development of satisfactory techniques for clutter suppression.

In addition to the unique long-range mission requirements discussed above, all IR seekers have common constraints that affect their clutter discrimination capability. Most important are resolution, stabilization, and high closing velocity. Typically, IR seekers have an aperture of about 5 cm resulting in a typical minimum resolution of 0.5 mrad at 5 μm and 1.0 mrad at 10

μm . Current IR seekers have a typical stabilization drift rate of ~ 0.1 degree/sec.

There are three basic techniques for point-target discrimination in clutter. The first is the use of a reticle to encode point-target data in a background scene. This approach allows continual observation of a wide field with a single detector while a spatially small target is tracked. The technique is used in most current IR seekers. Unfortunately, the reticle modulates any background structure within the field of view (FOV). This unwanted modulation can interfere with target detection, particularly if greater seeker sensitivity is required. An even greater drawback to reticle-based systems is the great difficulty in separating multiple targets or targets and decoys.

The drawbacks of the first technique are mitigated by the second technique, i.e., scanning a larger FOV with small instantaneous field-of-view (IFOV) detectors. Scanning systems can be implemented with single detectors or multiple detectors up to large arrays. Detector size is matched to optical resolution (i.e., to the size of the blur circle). Discrimination is based on the fact that most of the scene power is concentrated in large features. Small features, on the scale of the blur circle size, remain a source of clutter. As resolution increases (blur circle and detector size decrease), the clutter power entering the system is reduced. Hence detection capability is improved as resolution increases.

The third technique is the staring system. Again, small IFOV detectors are used. Discrimination is based on moving target detection. Each detector looks (stares) at a portion of the background. Successive frames are subtracted to detect the motion of a target from one pixel to the next. Ideally, all background power is removed in the subtraction process, leaving a result that is corrupted only by system noise. Unfortunately, there are practical implementation problems, including changes in background power during the stare period, caused by missile motion relative to the background (e.g., projected velocity on the three-

dimensional scene), by seeker stabilization (drift) errors resulting in pixel misregistration, and by temporal variations in the scene. The relatively large IFOV of a missile seeker (compared to advanced search set) requires a longer stare time for detection. The longer stare time, coupled with background changes, drift, and the need to scan a wide search field rapidly, makes implementation of staring processing unlikely in a long-range missile IR seeker.

For the reasons shown, this report concentrates on development and test of clutter suppression algorithms for scanning IR seekers.

1.3 Approach to Algorithm Development

The background data used in this study are described first. A characterization of the background imagery is then provided. The processing techniques used in the analysis are then described, followed by the results of processing the data by these techniques.

The description of background data includes a summary of data requirements and a survey of available IR clutter data. Reasons for selecting the background imagery used in this study and a detailed description of that data are provided.

Background data are then characterized and artifacts in the data examined and corrected. The characterization is used to guide the implementation of signal processing algorithms. In some cases, the background characterization can be used to estimate seeker performance directly and to make a comparison between scenes and spectral bands.

Finally, the original background data are directly processed with clutter-suppression algorithms to determine the effectiveness of the algorithm and ultimate clutter-limited performance of an advanced seeker. These algorithms are described and the reasons for their selection explained. Comparisons of sensor performance are made between different spectral bands and different scene types. Conclusions are in the form of expected sensor performance.

2.0 BACKGROUND DATA

2.1 Data Requirements

Background data needed to support a wide-area missile IR seeker are desired in the form of high spatial resolution, two-dimensional, contiguous background maps (scenes). Since the data support the evaluation of a scanning system, high relative radiometric accuracy along one of the scene dimensions (scan direction) is needed. Oversampled data in this direction are needed so filtering can be applied. Absolute radiometric accuracy, to within 20%, is required to provide a good estimate of sensor performance. Scanning background measurement sensors are most likely necessary to provide the radiometric accuracy and oversampling needed to predict performance of a scanning system.

The wide-area missile mission requires scenes with down-looking geometries. Typical seeker search is from high altitude, looking below the horizontal at depression angles of 5 to 20°. Since a representative set of all scenes of interest is an enormous quantity of data, this study concentrates on cloud scenes. Clouds present a variety of difficult clutter conditions, particularly over water.

Background data in two spectral bands are needed: middle-wavelength data and long-wavelength data. The middle-wavelength data, nominally 4 to 5 μm , require an angular spatial resolution of approximately 0.5 mrad. Long-wavelength data, nominally 8 to 12 μm , require an angular spatial resolution of about 1.0 mrad. Data taken at altitudes lower than typical wide-area missile search altitude (60,000 to 100,000 ft) can be obtained with lower resolution instruments, i.e., instruments that have the equivalent linear spatial resolution. Acquisition of simultaneous middle- and long-wavelength data is preferred to make a side-by-side comparison of performance between these two major spectral bands.

The noise in the background measurement sensor must be below that expected for advanced sensors. Sensor radiometric accuracy of 10^{-5} W/cm²/sr (middle wavelength) and 10^{-6} W/cm²/sr (long wavelength) is needed. The data resolution (digital sample increment) must be less than or equal to the rms noise requirements so that the sensor noise rather than digitizing noise is the predominant noise source.

Each scene should have sufficient samples to provide an estimate of false-alarm rate. A minimum of 10^6 pixels is necessary; 10^8 pixels or more are desired.

Table 1 summarizes the requirements for background data. These requirements, while designed to support development of a scanning IR seeker for a wide-area missile, are believed to be equally applicable to scanning infrared surveillance from aircraft.

2.2 Data Survey

A survey of available IR background data was conducted to gain an understanding of the available background data and to guide selection of the data for use in this study. Table 2 summarizes some of the available data sources. Comments on these sources are given below.

The Armament Laboratory at Eglin Air Force Base maintains two databases: BASES and TABILS. The BASES system is designed to support the development of missile seekers. It consists of a pod mounted on an F4 aircraft with 3 to 5 and 8 to 12 μm imagery (1.0 mrad) capabilities. These data are collected for a specific program, or SPO, and are not well cataloged. Targets are primarily tactical aircraft (all aspects) at close range. The background data, at ranges of interest, do not have sufficient signal-to-noise ratio for use in this study.

The second source is the Target and Background Information Library System (TABILS), which is accessible through remote computer terminals to DoD agencies and contractors. This database was developed to support air-to-ground tactical battlefield programs such as Assault Breaker, Tank Breaker, etc. A user's manual is available.¹

The Environmental Research Institute of Michigan (ERIM) has collected a large volume of airborne imagery with their M5 and M7 line scanners as part of the Navy Optical Signatures Program as well as for other sponsors. This work started in 1976 with an extensive survey of available background data,² followed by data collection of ground scenes from low altitude. Typical data are collected at 1000 to 2000 ft altitude in three IR spectral bands. Detector resolution of 2 to 2.5 mrad gives high spatial resolution on the ground. A summary of the data collected for

¹ Air Force Armament Laboratory, *Target and Background Information Library System (TABILS) User's Manual* (May 1, 1982).

² J. Beard, J. Braitwaite, and R. Turner, *Infrared Background Survey and Analysis*, ERIM 118000-1-F (Jun 1976).

Table 1 Requirements for wide-area missile IR background data.

Parameter	Requirement	
Geometry	60,000-100,000 ft altitude 5-20° depression angle	
Scenes	Cloud: solid layers multiple layers broken clouds storms and thunderheads Land	
Spectral bands	4.0-5.0 μm	8.0-12 μm
Angular resolution	0.5 mrad	1.0 mrad
Sensitivity	10^{-7} W/cm ² /sr	10^{-6} W/cm ² /sr
Radiometric dynamic range (from zero)	12 bits	12 bits
Radiometric accuracy	better than 20%	
Oversampling (scan direction)	2:1 or greater	
Number of pixels per scene	$\geq 10^6$	

1978-1979, as well as earlier data, is given in Ref. 3. More recently (1983), long-wavelength European terrain background data were collected.

A number of government agencies and contractors are tasked to collect data for the long-range detection of air targets. General Electric and ITT, under contract to the Air Force Weapons Laboratory, have developed middle-wavelength airborne IR search and track systems. These systems were tested at Eglin Air Force Base in the summer of 1985. Data produced by the tests were not available for this analysis. The Navy is planning to continue the development with full-scale engineering, starting in late 1986.

The Navy Background Measurements and Analysis Program (BMAP) is being conducted as a succe-

sor to the background portion of the Optical Signatures Program. The program is tasked with collecting data needed to design surface- and air-based IR search and track systems. The initial instrument is a high-spatial-resolution, high-sensitivity device with simultaneous 4 to 5 μm and 8 to 11 μm coverage.^{4,5} Initial data collection began with surface measurements in 1984 (Ref. 6) and has continued with airborne (P3 aircraft) measurements. A follow-on instrument

⁴R. L. Lucke, et al., "The Navy's Infrared Background Measurement and Analysis Program," in *Proc. IRIS Specialty Group Meeting on Targets, Background, and Discrimination*, San Diego (Feb 11-14, 1986).

⁵R. A. Steinberg, "Navy IR Background Measurements and Analysis Program," in *Proc. Tri-Service Infrared Backgrounds Symp.*, Oct 18-20, 1983, Mitre Corporation, pp. 216-223.

⁶A. Hirschman, "BMAP Surface-Based Background Measurement Activities at Montauk Point, New York, August 1983," Naval Surface Weapons Center, White Oak, Silver Spring, Md., draft report (Nov 1984).

³J. J. LaRocca and D. J. Witte, *Handbook of the Statistics of Various Terrain and Water (1a) Backgrounds from Selected U.S. Locations*, ERIM 139900-1-X (Jan 1980).

Table 2 Summary of available background data.

Source agency	Database	Platform	Sensors
AFATL	BASES TABILS	F4	AGA 3-5, 8-12 μm
		Various	Imagery
AFFTD		KC-135	Spectrometer, 3-5 μm FLIR, 8-12 μm
AFWAL			FLIR, 8-12 μm
AFGL		NKC-135	Spectrometer, 3-5 μm NORELCO, 3-5 μm FLIR, 8-12 μm
NSWC/DL		Ground-based	Spectrometer, 3-5 μm FLIR, 3-5 and 8-12 μm
NRL	BMAP	P-3	Radiometer, 3-5 and 8-12 μm
NWC	Target Signatures Program		Various
DARPA/Lockheed (ERIM library)	BMP, CAMP HICAMP	U2	Scanner; several staring imagers, 10-12 μm
General Dynamics		Ground-based	Spectrometer, 3-5 and 10-12 μm
Block Engineering		Ground-based	Spectrometer, 3-5 μm
General Electric Syracuse		C-54	Imager, 8-12 μm
ERIM		C-47	M-5 and M-7 multi- spectral scanner
MIT/LL			FLIR, 3-5 and 8-17 μm
JHU/APL		P-3	Radiometer, 3-4 and 10-12 μm

with an expanded number of detectors per spectral band (from 16 to 120) and higher spatial resolution (0.25 mrad) is under development.

General Dynamics, NSWC/DL, and Block Engineering have ground-based measurement systems. These organizations maintain excellent calibrated signature libraries of tactical aircraft flown at low altitudes. A summary of spectral background measure-

ments made by General Dynamics is given in Ref. 7, and a compendium of their target signatures library is given in Ref. 8.

⁷General Dynamics/Pomona Division, *Background Spectral Radiance and Contrast in the Near-UV, Mid-IR, and LWIR Regions*, TM6-125PH-438 (Oct 1976).

⁸General Dynamics/Pomona Division, *Available Target Infrared Spectral Signature Data*, TM6-125PH-450 (Sep 1981).

The Applied Physics Laboratory has measured the radiometric properties of sea surface with low-altitude (500 to 3000 ft) flights of a line-scanning, dual-band (3.6 to 4.1 μm and 10.1 to 11.1 μm radiometer. This instrument has high sensitivity ($\text{NE}\Delta\text{T}$ of 0.003 K in each band) and low spatial resolution (10 to 200 mrad). An instrument description and typical data are given in Ref. 9.

Another major source of target and background data is the DARPA Infrared Data Library located at ERIM. This library serves as the archival collection of data with secret security classification. Major programs represented in the library are the DARPA-sponsored Background Measurements Program (BMP), the Calibrated Airborne Measurements Program (CAMP), and the Highly-Instrumented, Calibrated Airborne Measurements Program (both HICAMP and HICAMP-II). A report on library holdings¹⁰ lists the contents of the library.

The Air Force Geophysics Laboratory (AFGL) operates an instrumented NKC-135 aircraft to acquire target and background signature data. Over the past 10 years AFGL has collected in-flight spectral and spatial data on several tactical and strategic aircraft (e.g., T-38, F4, F5, F14, F15, A4, A7, B1, B52, C140, KC135, etc.). The measurement aircraft typically flies at 6 km (20,000 ft) altitude, but is capable of acquiring data at altitudes ranging from 0.3 to 13 km (1000 to 42,000 ft). Data can be taken in the down-, side-, forward-, and rear-looking modes.

This aircraft contains a number of IR measurement instruments for various purposes. Spectral measurements are made with Michelson interferometers having spectral resolution of 0.1 (for plume) to 32 cm^{-1} . Imagery data are taken in two broad spectral bands (3 to 5, 8 to 12 μm) and subbands within these intervals. The mid-wave IR (MWIR) imagery data are taken at 1 mrad resolution using an AC-coupled system. Consequently, the data only provide differential radiance values. The 8 to 12 μm forward-looking IR (FLIR) system consists of two 9-element HgCdTe detectors with serial scan at TV-compatible rates.¹¹ The IFOV is approximately 0.5 mrad, and a typical image consists of 192×256 pixels. Individual frames can be spliced together to form a long-track mosaic on the order of 0.75 km by 40 km. Two such tracks have been constructed: one in the American West (near

Santa Cruz, California) and the other in northern-latitude ice fields.

The AFGL has not been specifically tasked to acquire data for the IR search and track (IRST) (long range detection) problem. However they have acquired data relevant to this effort in the course of scheduled missions. These include horizontal viewing, 2° above and below the horizon, cloud orbits, and cloud fly-throughs. These data have not been cataloged.

2.3 Selected Data

Selected data were based on criteria of (a) availability, (b) measurement with a scanning instrument, and (c) no classification restrictions. Once algorithms are developed, they will be tested on classified as well as unclassified data.

Three data sets are used in this study: images from AFGL, ERIM, and BMAP. AFGL scenes are all long-wavelength scenes of clouds or clouds and terrain viewed from high altitude. ERIM scenes are short-, middle-, and long-wavelength scenes of many types of terrain as well as of water taken from low altitude. BMAP data consist of middle- and long-wavelength scenes taken from the ground. Airborne BMAP data have been taken and are expected to be used for future work. Each of these data sets is described in the following paragraphs.

Two sets of BMAP data were supplied by the Naval Research Laboratory. The BMAP instrument consists of 16 middle-wavelength and 16 long-wavelength detectors each with a 0.33 by 0.33 mrad IFOV. Data in the scan direction are sampled every 0.096 mrad resulting in an oversampling of 3.3 to 1. The data are stored as 16-bit words. To convert the data to radiance, the data were multiplied by the multiplicative factor (MF) corresponding to the correct IR band. (For the BMAP data, the MF equaled the noise equivalent irradiance (NEI) of the system.) Appendix A contains more detailed information on the BMAP instrument and imagery including the spectral response and the impulse response of the sensor.

The BMAP sensor has two modes of operation. Data can be collected in a format of 8 lines of long-wavelength IR followed by 8 middle-wavelength IR lines per frame. In this 8/8 format, the data are extracted from coincident detectors. The second format is 16 lines of either middle- or long-wavelength IR data per frame. In this mode, the frames usually alternate between the spectral bands.

APL has received data in both of the formats. Fifty frames of data were collected at Montauk Point, Long Island in the 8 long-wavelength 8 middle-wavelength format. The background scene for these data was overcast sky.

⁹K. Peacock, *Radiometric Temperature Characteristics of the Ocean Surface*, JHU/APL STD-R-377 (Oct 1980).

¹⁰A. J. LaRocca and B. A. Whaley, *DARPA Infrared Data Library*, ERIM 155300-24-X (Jul 1984).

¹¹J. Shumsky and J. H. Schummers, *AFGL FLIR NKC-135 Aircraft Instrument*, AFGL TR-82-0031 (Jan 26, 1982).

The second set of BMAP data received by APL was collected at Bedford, Massachusetts. These data were in the format of 16 lines of alternating spectral bands per frame. APL used the first 61 frames of these data. Thirty-one frames were mid IR and 30 frames were long IR. Long-wavelength IR frames only had 15 lines of data per frame. A hole in a cloud deck was the background scene for these frames. More detail on the images is included in Appendix A.

Data from AFGL were the second set used in this study. The instrument is a two-detector array, serial scan, FLIR unit with a 10-position filter wheel that can select various spectral bands. All data supplied to APL were taken with filter I9005A (7.84 to 13.16 μm). The FOV on this seeker was 0.36 (H) \times 0.43 (V) mrad, but the digitizing sample size was 0.52 (H) by 0.45 (V) mrad. Eight of the frames have an additional telescope decreasing the IFOV to less than 0.1 mrad. The sample size means that these images were slightly undersampled (as opposed to the BMAP images). Video data (EIA RS-170) are recorded and subsequently digitized before distribution to APL. A more detailed description of the AFGL data is included in Appendix B.

The AFGL scenes are stored on tape in an 8-bit format (1 pixel = 1 byte). Because of this, the data were scaled to range from 0 to 255. To recover radiance, a multiplicative factor and an additive factor (AF) were applied to the data. Each scene has a unique MF and AF. These factors are listed in Appendix B. Thirty scenes were available for analysis; the four primary AFGL scenes used in this analysis were 101R, 104R, 105R, and 109R.

The third set of data used in this study was from ERIM. The data collection instrument is a line scan-

ner flown at low altitude. Ten spectral bands were available with the ERIM scanner. At most, four bands were scanned for a scene. The size of the scenes was variable. The FOV of the scanner also varied slightly. Appendix C has more detailed information on the ERIM data.

Six ERIM scenes are used in this study. These are denoted S01, S02, S03, S23, S24, and F08. There were three or four channels for each of these scenes. The first three of these scenes are from Camp A.P. Hill, Virginia. These images provide morning, afternoon, and evening data of one scene. S23 and S24 are of Port Hueneme, California. S23 is of the port and water; sunglint is added to this in S24. The last image, F08, is of the mountains by Nellis AFB.

Table 3 compares the characteristics of the BMAP, AFGL, and ERIM data.

Figure 1 shows an image from each of the sets of data used in this study. Part A shows middle-wavelength BMAP data from Bedford (31 frames of data are shown). Part B of the figure shows the AFGL scene 109R. The remainder of the images in this figure are ERIM images. Part C is S01CH2, part D is S02CH2, and part E is S03CH2. These three are middle-wavelength images from Camp A.P. Hill at different times of day. Part F of the figure is S23CH3 from Port Hueneme. Finally, part G of the figure is F8CH1, a mountain scene from Nellis AFB. These images will be shown after each of the processing steps to show the effect of the processing.

Table 4 summarizes the data used in this study. All of the images used, IFOV, size, spectral band, and descriptive comments are included in this table.

Table 3 Characteristics of instruments used to collect background data used in this study.

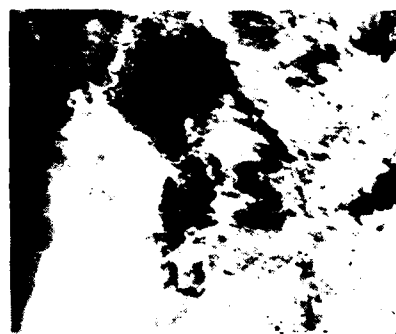
Parameter	BMAP sensor	AFGL sensor	ERIM sensor
Platform	Ground	NKC-135 @ 35,000 ft	C-47
Viewing geometry	5° elevation	Typically small depression angles	90° depression (nadir) ±45° scan or 35° depression with ±45° scan
Sensor band (μm)	3.9-4.8 7.6-11.3	7.84-13.16	various bands: 2.0-2.6 3.0-4.6 3.5-3.9 3.9-4.7 4.5-5.5 8.0-14.0 9.0-11.4
Instantaneous field of view (mrad)	0.33 × 0.33 (azimuth resolution = 0.096)	0.36 (H) × 0.43 (V) (digitized sample size = 0.5 × 0.5)	2.0 or 2.5 (circular)
Sensitivity NEI (W/cm ²)	Long 1.1 × 10 ⁻¹³ Mid 6.1 × 10 ⁻¹⁵	5.5 × 10 ⁻¹²	2.0-2.6 μm 4.91 × 10 ⁻¹² 3.5-3.9 μm 8.83 × 10 ⁻¹² 3.9-4.7 μm 3.40 × 10 ⁻¹² 4.5-5.5 μm 4.47 × 10 ⁻¹² 8.0-14.0 μm 2.45 × 10 ⁻¹¹ 9.0-11.4 μm 4.63 × 10 ⁻¹¹
NEΔT (°C)	Long 0.02 Mid 0.01	0.40	3.5-3.9 μm 3.0 3.9-4.7 μm 0.25 4.5-5.5 μm 0.2 8.0-14.0 μm 0.1 9.0-11.4 μm 0.25
Scene size	8 scans mid-IR and 8 scans long-IR per frame or 16 scans mid-IR per frame and 15 scans long-IR per frame 373 pixels per scan line oversampled at 3.3:1	256 (H) × 192 (V) pixels	855 or 646 pixels (H); number of lines per scene varies from 700 to 2000



(a)



(b)



(c)



(d)



(e)

ERIM images of Camp A.P. Hill (4.5-5.5 μm).



(f)



(g)

Figure 1 Images from each of the sets of data used in this study. (a) BMAP middle-wavelength image from Bedford. (b) AFGL scene 109 of Monument Valley. (c) Morning (scene S01CH2). (d) Afternoon (scene S02CH2). (e) Evening (scene S03CH2). (f) ERIM image of Port Hueneme (4.5-5.5 μm spectral band) (scene S23CH2). (g) ERIM image of mountains by Nellis AFB (3.9-4.7 μm spectral band) (scene F8CH1).

Table 4 Summary of data used in this study.

Data source	Scan IFOV (H) (mrad)	Image size (H) (V)		Comments		
BMAP	0.33	373	8	Montauk (50 frames); long- and mid-IR: overcast sky; sample spacing: 0.1 mrad		
BMAP	0.33	372	15 16	Bedford1 (61 frames) Long-IR: hole in cloud deck Mid-IR: hole in cloud deck Sample spacing: 0.1 mrad		
AFGL	0.5	256	192	<u>File</u>	<u>Description</u>	
				101R	clouds, down viewing	
				104R	terrain, down viewing	
				105R	horizon, clouds, terrain	
				109R	Monument Valley, clouds	
ERIM1	2.0	855	700	<u>File</u>	<u>Band</u>	<u>Camp A.P. Hill</u>
				S01CH1	2.0-2.6	Morning
				S01CH2	4.5-5.5	"
				S01CH3	8.0-14.0	"
				S02CH1	2.0-2.6	Afternoon
				S02CH2	4.5-5.5	"
				S02CH3	8.0-14.0	"
				S03CH1	Bad data	Evening
				S03CH2	4.5-5.5	"
				S03CH3	8.0-14.0	"
ERIM3	2.5	646	1982	<u>File</u>	<u>Band</u>	<u>Port Hueneme</u>
				S23CH1	2.0-2.6	Port/water
				S23CH2	Bad data	"
				S23CH3	4.5-5.5	"
				S23CH4	9.0-11.4	"
				S24CH1	2.0-2.6	Port/water/sun
				S24CH2	3.0-4.2	"
				S24CH3	4.5-5.5	"
				S24CH4	9.0-11.4	"
ERIM5	2.5	646	1541	<u>File</u>	<u>Band</u>	<u>Nellis AFB</u>
				F08CH1	3.9-4.7	Mountains
				F08CH2	3.5-3.9	"
				F08CH3	9.0-11.4	"

3.0 CHARACTERIZATION OF DATA

3.1 Data Artifacts and Corrections

There are a number of data artifacts and characterization uncertainties that limit the usefulness of scene data to background investigations. All data used in this investigation have one or more of the following unwanted artifacts: (a) significant sensor noise, (b) data errors, (c) calibration uncertainty, (d) imprecisely known sensor characteristics, and (e) sensor-induced scene artifacts.

When the sensor noise masks part of the scene-clutter power spectrum, the high-spatial-frequency component of the background clutter is lost and the full spatial resolution of the collection sensor cannot be used in evaluating the effect of clutter. Data errors can include poorly performing detectors, recording errors, and externally produced noise (e.g., from vibration). Such errors can produce target-like signals that significantly degrade usefulness in determining the effectiveness of an algorithm that uses spatial extent as the discriminant.

Calibration errors include radiometric inaccuracy that causes a significant variation in the predicted performance in clutter and calibration imbalance between detectors that degrades the scene in the cross-channel direction. This latter effort is not especially significant if all processing is done using data from the collection instrument scan direction only. Uncertainty in the clutter processing results is also introduced by unknown or imprecise description of the instrument and its functioning. Accurate knowledge of the spectral response, and optical and electrical transfer functions are frequently imprecise or unknown.

Finally, the data collection geometry can adversely affect the data by introducing aperture vignetting (i.e., lower scene variations) or geometric distortion (such that the pixel footprint on the scene varies significantly across a scan line). These effects are particularly noteworthy in wide FOV instruments. Another geometric effect is imprecise or changing registration between detectors making simultaneous measurements in multiple spectral bands. Registration between spectral bands becomes particularly significant if multiple colors are part of the discrimination processes.

All data sets used in this investigation had artifacts and, to some extent, imprecise knowledge of the sensor characteristics. A description of the major artifacts in each data set is given below.

The BMAP data had some defective data points caused by the data acquisition system. Software creat-

ed at the Naval Research Laboratory (NRL) located the bad data points in the BMAP images and corrected them by linearly interpolating from adjacent good data points.^{12,13} These interpolated points were identified in the data supplied to APL by assigning them a negative value. When the data are used, these negative values are changed back to positive values. (For this study, we did not need to keep track of the bad data points.) Correcting these data recording errors was all that had to be done to the BMAP data.

When the BMAP Montauk images were first received at APL some of the recording errors had not been corrected by the NRL software. The errors were detected after the images were processed through the clutter-suppression algorithm. (The clutter-suppression algorithm passed many of the bad data points as possible targets.) NRL then sent a corrected set of the images to APL. The performance of the clutter-suppression algorithm was much better on these updated images than on the original images.

Both the AFGL and some ERIM images were significantly affected by noise within the sensor. This noise masks the highest frequencies of the background clutter. The effect of this noise will be discussed when the power spectral densities (PSD) are presented. Methods of reducing the effect of this noise will also be discussed later in this report.

AFGL images were formed by a TV-like raster scan, with alternate lines produced by separate detector arrays. The two detector arrays produced alternating lighter and darker scan lines when the response of the two arrays had drifted out of calibration. Reference 14 describes how the images were corrected. First, the mean of each line was computed. Half of the difference of the mean values was then added to pixels in the darker lines and half the difference was subtracted from pixels in the lighter lines. All of the AFGL scenes shown in this study have been corrected.

There were multiple problems with the ERIM data. The main problem was that images obtained with a depression angle less than 90° suffered from vignet-

¹²R. A. Steinberg, *Elimination of Sensor Artifacts from Infrared Data*, NRL Report 8861 (Dec 11, 1984).

¹³R. A. Steinberg and M. J. McHugh, *An Error Detection and Smoothing Algorithm for Infrared Data*, JHU APL TG 1355 (Apr 1986).

¹⁴A. N. Vavreck, *AFGL Infrared Image Restoration*, JHU APL FID(1983)-079.

ting by part of the aircraft fuselage. Reference 15 describes how this problem was corrected. A downscan average of all of the lines in the scene was computed. The mean and standard deviation of the left and right edges of the scene were then adjusted to create a constant mean and standard deviation for the downscan average. This restoration improved the images but some bright and dark bands still remained on the edges of the restored images.

In addition to the vignetting problem, there were some other problems with particular scenes. These problems were found while analyzing the scenes during the study. All three channels of S01 had 10 bad scan lines. These lines were found because they had pixel values of 0 or 255. No other lines in the scene had these pixel values. This artifact (see Fig. 1c) was corrected by simply skipping the 10 bad lines.

Channel 1 of S03 was not processed. ERIM reports analyzing these data never included this scene in the analysis. A PSD plot of the scene differed from PSDs of all of the other scenes. Most likely, the sensor was not able to acquire background data because the signal-to-noise ratio was too low. The image is essentially featureless. This scene was therefore excluded from the study.

Channel 2 of S23 was also excluded from the study. While analyzing this image (shown in Fig. 2) some unexpected results were obtained. Examination of the digital data of this scene showed that the pixel values were mostly 0 and 255. Since the data showed that there was a problem with this image, it was excluded.

3.2 Radiance Statistics

Before any of the IR data were processed certain characteristics of the data were needed. A histogram of each image was computed. From this histogram the maximum and minimum in the scene were obtained. The mean and variance were also calculated for each image. Table 5 lists the radiance values (mean, variance, maximum, and minimum) for most of the images used in this investigation.

The radiance statistics are needed to assess the performance of the processing techniques used. The maximum and minimum irradiance (with mean removed) will be compared to the maximum and minimum after processing. This comparison provides a measure of the performance of the processing techniques.



Figure 2 Image showing bad data in ERIM scene S23CH2.

3.3 Power Spectral Density

In addition to calculating the moments of the images, the PSDs were also computed because they were needed in selecting the appropriate filters for the images. Figure 3 shows the PSDs of the BMAP Montauk long- and mid-IR bands. Figure 4 shows the PSD of one of the AFGL scenes. Figure 5 shows the PSD of an ERIM scene. Appendix D has the PSDs of many of the remaining scenes. From Figs. 3 through 5, it is seen that all of the PSDs have approximately the same slope. The power falls off as the inverse of the square of the spatial frequency ($1/k^2$). Such a frequency dependence is often observed in background data. Figures 3 through 5 also show that at the higher frequencies all of the PSDs begin to flatten.

The level at which a PSD flattens is the noise level of the system. All three figures show the flattening. These figures and the additional power spectral density data given in Appendix D show that all of the AFGL and some of the ERIM PSDs have this flattening. BMAP data also show some change in slope at high frequencies.

The flattening of BMAP PSDs occurs because of the oversampling of the scene. The BMAP detector

¹⁵ A. N. Vavreck, *ERIM Infrared Image Restoration*, JHU/APL FID(1)84-U-003.

Table 5 Statistics of background data in units of W/cm²/sr.

Scene	Spectral band (μm)	Image Statistics				
		Mean	Variance	Max	Min	Δ (max - min)
BMAP-Montauk (long IR)	7.6-11.3	1.93×10^{-3}	1.43×10^{-9}	2.04×10^{-3}	1.84×10^{-3}	0.20×10^{-3}
BMAP-Montauk (mid IR)	3.9-4.8	7.35×10^{-5}	2.17×10^{-13}	9.10×10^{-5}	6.41×10^{-5}	2.69×10^{-5}
BMAP-Bedford (long IR)	7.6-11.3	1.66×10^{-3}	5.09×10^{-8}	1.76×10^{-3}	1.30×10^{-3}	0.46×10^{-3}
BMAP-Bedford (mid IR)	3.9-4.8	1.05×10^{-4}	3.12×10^{-5}	1.92×10^{-4}	7.26×10^{-5}	1.19×10^{-4}
AFGL I01R	7.84-13.16	2.87×10^{-3}	5.01×10^{-8}	3.87×10^{-3}	2.42×10^{-3}	1.45×10^{-3}
AFGL I04R	7.84-13.16	3.81×10^{-3}	1.36×10^{-7}	4.43×10^{-3}	2.74×10^{-3}	1.69×10^{-3}
AFGL I05R	7.84-13.16	3.01×10^{-3}	2.69×10^{-8}	3.42×10^{-3}	2.44×10^{-3}	0.98×10^{-3}
AFGL I09R	7.84-13.16	2.80×10^{-3}	3.57×10^{-8}	3.46×10^{-3}	2.32×10^{-3}	1.14×10^{-3}
ERIM F8CH1	3.9-4.7	5.2×10^{-5}	7.8×10^{-11}	7.2×10^{-5}	2.5×10^{-5}	4.7×10^{-5}
ERIM F8CH2	3.5-3.9	1.2×10^{-5}	2.0×10^{-11}	2.8×10^{-5}	2.3×10^{-5}	2.8×10^{-5}
ERIM F8CH3	9.0-11.4	1.8×10^{-3}	2.8×10^{-8}	2.3×10^{-3}	1.4×10^{-3}	0.9×10^{-3}
ERIM S01CH1	2.0-2.6	3.6×10^{-5}	2.6×10^{-10}	1.0×10^{-4}	0.0	1.0×10^{-4}
ERIM S01CH2	4.5-5.5	1.5×10^{-4}	2.1×10^{-10}	2.7×10^{-4}	1.2×10^{-4}	1.5×10^{-4}
ERIM S01CH3	8.0-11.4	4.2×10^{-3}	2.8×10^{-8}	6.0×10^{-3}	3.1×10^{-3}	2.9×10^{-3}
ERIM S02CH1	2.0-2.6	3.7×10^{-5}	2.2×10^{-10}	1.3×10^{-4}	0.0	1.3×10^{-4}
ERIM S02CH2	4.5-5.5	1.6×10^{-4}	1.8×10^{-10}	2.8×10^{-4}	1.3×10^{-4}	1.5×10^{-4}
ERIM S02CH3	8.0-11.4	1.9×10^{-3}	8.1×10^{-9}	3.1×10^{-3}	1.5×10^{-3}	1.6×10^{-3}
ERIM S03CH2	4.5-5.5	1.5×10^{-4}	5.3×10^{-11}	1.9×10^{-4}	1.3×10^{-4}	0.6×10^{-4}
ERIM S03CH3	8.0-11.4	4.0×10^{-3}	1.4×10^{-8}	4.9×10^{-3}	3.6×10^{-3}	1.3×10^{-3}
ERIM S23CH1	2.0-2.6	3.8×10^{-5}	1.1×10^{-9}	2.6×10^{-4}	0.0	2.6×10^{-4}
ERIM S23CH3	3.0-4.2	2.1×10^{-4}	1.3×10^{-9}	4.5×10^{-4}	1.4×10^{-4}	3.1×10^{-4}
ERIM S23CH4	9.0-11.4	2.3×10^{-3}	1.0×10^{-7}	4.5×10^{-3}	1.5×10^{-3}	3.0×10^{-3}

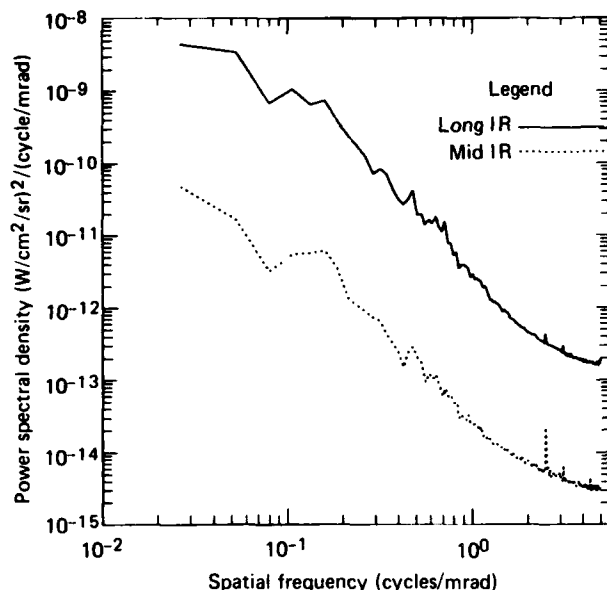


Figure 3 Power spectral density of BMAP Montauk Point middle-wavelength and long-wavelength background data.

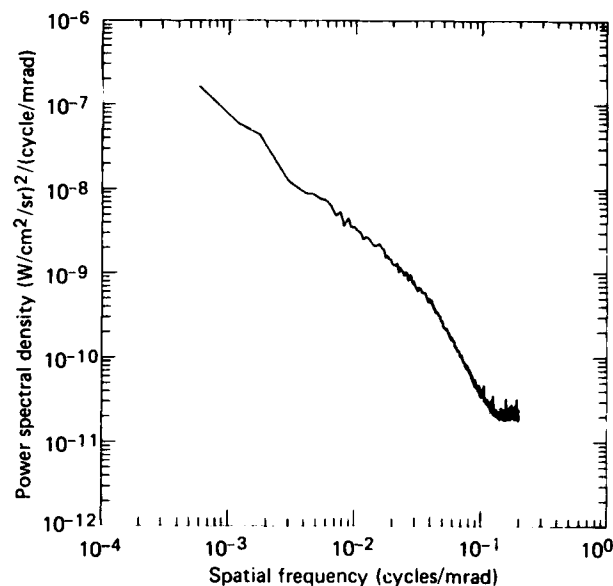


Figure 5 Power spectral density of ERIM Port Hue-neme scene in 2.0-2.6 μm spectral band (scene S23CH1).

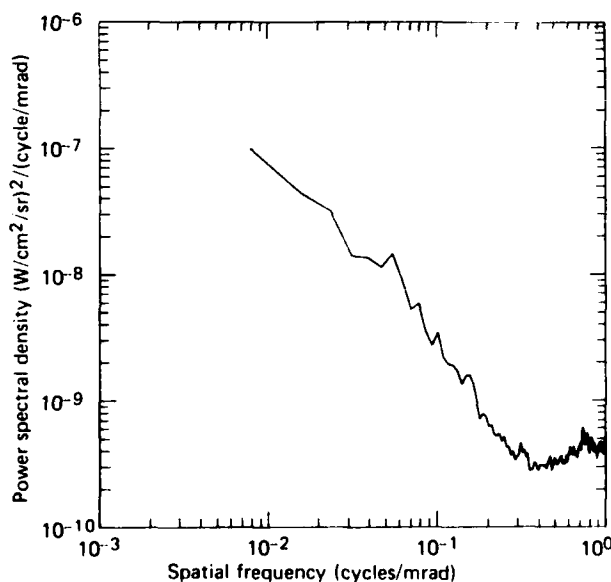


Figure 4 Power spectral density of AFGL cloud and terrain background scene 105.

has a resolution of 0.33 mrad, giving a maximum spatial frequency of about 1.5 cycles/mrad. However, the scene is sampled at 0.1 mrad resolution, giving a max-

imum Nyquist frequency of 5 cycles/mrad. Since the detector limits the frequency to 1.5 cycles/mrad, data between 1.5 cycles/mrad and 5 cycles/mrad are principally sensor noise.

All of the AFGL PSDs show the flattening because at high spatial frequencies the power of the noise within the sensor is greater than the power from the scene. Without the sensor noise, the PSDs are expected to maintain the $1/k^2$ slope up to 1.0 cycle/mrad. Several AFGL scenes with higher spatial resolution (~ 0.1 mrad) were also analyzed and show that the $1/k^2$ slope continues to at least this spatial frequency (see Appendix D).

Table 6 lists the levels at which the four PSDs flatten and the frequencies where they begin to flatten. These values are also listed for some of the PSDs given in Appendix D. Also listed in Table 6 are the cut-off frequencies of the sensors. The roll-off of the PSDs, the noise level, and the cutoff frequency are used in the analysis.

The point-source characteristic of the BMAP data is included in Appendix A. Since the BMAP scenes are oversampled, a point target in the scene will spread into many pixels in the resulting image. The Fourier transform of the point-source characteristic was computed for both the long- and mid-IR bands. Figure 6 shows the Fourier transform of the point-source

Table 6 PSD noise level.

Scene	Power spectral density at noise level ($(W/cm^2/sr)^2/(cycles/mrad)$)	Flattening frequency (cycles/mrad)	System cutoff frequency (cycles/mrad)
BMAP (long IR)	1.5×10^{-13}	3.0	1.5
BMAP (mid IR)	3.0×10^{-15}	3.0	1.5
AFGL (I01R)	3.3×10^{-10}	0.35	1.0
AFGL (I04R)	2.0×10^{-9}	0.35	1.0
AFGL (I05R)	3.0×10^{-10}	0.30	1.0
AFGL (I09R)	4.0×10^{-10}	0.30	1.0
ERIM (S01CH1)	6.0×10^{-12}	0.15	0.25
ERIM (S01CH2)	1.5×10^{-12}	0.17	0.25
ERIM (S23CH1)	2.0×10^{-11}	0.15	0.20

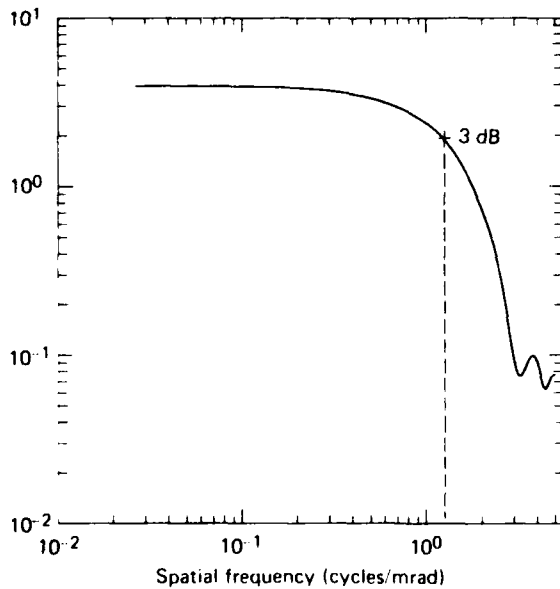


Figure 6 Fourier transform of point source as seen by the BMAP instrument.

characteristic of the long-IR band. The plot looks like a low-pass filter with a cutoff at about 1.5 cycles/mrad.

Point-source characteristics of the AFGL data were not available. Some ERIM frequency response data are included in Appendix C. Since there was no oversampling in either of these data sets, it was assumed that the point-source target is an impulse. The PSD of an impulse is a flat spectrum with a cutoff at the Nyquist frequency. Therefore, while the PSD of the BMAP point-source characteristic looks like a real low-pass filter, the PSDs of the AFGL and ERIM point-source characteristics are assumed to be ideal low-pass filters.

4.0 SCENE CLUTTER PROCESSING

4.1 Approach

The first technique examined uses the PSD of the scene to give an estimate of the required target signal for detection. A signal-to-noise criterion was selected to produce a nominal false-alarm level. The target is modeled as a point source with unknown irradiance in the spectral band. A matched filter is then applied to the signal and noise spectra to estimate the required target irradiance for detection. The target irradiance required for detection and the false-alarm rate are the primary measures of performance, both in this study and for tactical sensors. This technique is well-established and often used to estimate IR sensor performance.^{16,17}

A matched-filter approach offers a number of advantages. Foremost is that this approach allows one to make performance estimates for a scanning sensor in the presence of background clutter rather than on sensor noise alone. Since the matched-filter technique gives the maximum achievable performance, this method sets a limit (or standard) on sensor detection capability. The matched-filter approach can be used to compare clutter-limited performance in different scenes and in different spectral bands when the same scene is measured in multiple colors.

The matched-filter approach to predicting clutter-limited performance has well-known disadvantages. Results of the method are incorrect because real scenes do not meet the assumptions of the matched-filter analysis (see below). Even so, a processing filter that is approximately "matched" to the signal and clutter spectrum approximately minimizes the clutter power into the sensor. Hence the matched-filter method "designs" a real filter that can be applied directly to the raw scene data. Directly filtering the raw scene provides a measure of false-alarm rate as a function of detection threshold. The threshold can then be used to estimate the required target irradiance.

Therefore, the second approach is directly filtering the raw scene with a digital filter that approximates a matched filter. Raw data is processed with a first-order high-pass filter that approximately "whitens" the clutter spectrum. Results of this filtering process can be compared to that of the matched-filter analysis. Several methods of comparison are possible: one

is to determine the threshold required to give no false alarms in the filtered data and then compare the results with the threshold that would be required to give no false alarms (e.g., false alarm probability of ≤ 0.5) in the matched-filter analysis.

Thresholding the filtered data at various levels gives the number of false alarms (i.e., false-alarm rate) as a function of threshold (hence, target signal). After filtering, the scene has the mean background level removed and large, low-frequency features are suppressed. Unfortunately, large features with sharp edges will also produce a significant filter output that is indistinguishable from that produced by a target. Real scenes have a number of these boundaries such as cloud edges against sky, terrain, or other cloud layers, terrain crests and valleys, and boundaries between woods and fields.

Further discrimination is obtained by examining the differences in high-pass filter response to point objects and to extended objects. Since the high-pass filter acts as a differentiator, a filtered positive point feature produces a positive pulse immediately followed by an approximately equal-amplitude negative pulse. (The reverse is true for a negative point feature.) On the other hand, a sharp edge will only produce a positive (or negative) pulse, not a pair of pulses. Therefore a pulse-width discriminator can be developed to separate small point features from edges.

Implementation of the pulse-width discriminator requires that a negative crossing of a specially set confirmation threshold will follow a positive crossing of the detection threshold. Similarly, crossings of the negative detection threshold (i.e., to detect a negative contrast target) must be followed by a crossing of the positive confirmation threshold. The confirmation thresholds are only active for a short time after a crossing of the detection threshold.

This pulse-width discriminator rejects sharp edges and therefore enhances the discrimination provided by the high-pass digital filter. Performance is again measured in terms of number of detections as a function detection threshold level (i.e., false-alarm rate). However, the high-pass filter plus pulse-width discriminator is still not sufficient to eliminate extended scene features totally. Linear features such as roads and sun-enhanced cloud edges will pass the processing tests. If the sensor has multiple parallel detection channels, near simultaneous detections in adjacent channels can be used to reject features with extent in the cross-scan direction.

¹⁶ H. Samuelson, "Infrared Systems: I. Expressions for Signal and Background Induced Noise with Space Filters," *IEEE Trans. Aerosp. Electron. Syst.* **AES-7**, 27-33 (1971).

¹⁷ R. Yoshitani, "Signal Processing Theory for Linearly Scanning Rectangular Detector," *Proc. IRIS* **18**, 117-148 (1973).

This post-detection adjacent-channel logic will allow discrimination against linear features whose length extends across three or four contiguous channels. The combination of high-pass filtering, pulse-width discrimination, and adjacent-channel logic provides a complete set of spatial-discrimination techniques that allow separation of point features from larger features with significant in-scan or cross-scan extent (or both). The nature of the scanning geometry provides better discrimination in the in-scan direction because of over-sampling.

Even implementation of the above combination of techniques cannot eliminate all potential false alarms. Background features whose spatial extent is ≤ 2 detector widths (or pixels or resolution cells) in the scan direction and ≤ 3 detector widths in the cross-scan direction cannot be distinguished from targets. As sensor sensitivity is improved, the number of these small features that pass all point source discrimination tests will increase and clutter will limit the sensor performance. When this fundamental limit is encountered, other discrimination techniques such as improved spatial resolution (unlikely in a missile seeker) or color (multiple-spectral-band) tests must be investigated. Such an investigation requires a database beyond the scope of this investigation.

The following sections describe the analyses and results of these discrimination techniques as applied to the available background scenes.

4.2 Matched-Filter Performance Analysis

Using the PSDs of the AFGL, BMAP, and ERIM images, a matched filter was applied to the data.^{18,19} The signal was assumed to be an impulse (flat spectrum to the cutoff frequency), and the cutoff frequency (i.e., spatial resolution) was varied up to the sensor resolution-limited Nyquist maximum value to determine the effect of spatial resolution. A minimum target irradiance required for detection was determined as a function of the cutoff frequency assuming a target irradiance to rms clutter noise irradiance of $\sqrt{50}$. Hence, the detection threshold is 7.07 times the rms clutter noise. Assuming that the noise is Gaussian, the false-alarm probability is 0.5 after about 10^{12} independent looks (resolution cell).

From the above discussion, the signal-to-noise ratio (SNR) is given as

$$SNR = \frac{|s(0)|^2}{\sigma_N^2} \quad (1)$$

where $s(0)$ is the peak signal output and σ_N^2 is the variance of the noise output. For a system with a filter transfer function $H(f)$ the peak signal and noise variance are

$$s(0) = \int_{-\infty}^{\infty} H(f) s(f) df \quad (2a)$$

and

$$\sigma_N^2 = \int_{-\infty}^{\infty} |H(f)|^2 N(f) df \quad (2b)$$

where $s(f)$ is the signal spectrum and $N(f)$ is the noise (internal plus scene) PSD. For a matched filter

$$SNR^2 = \int_{-\infty}^{\infty} \frac{|s(f)|^2}{N(f)} df \quad (3)$$

and when the target is an impulse, the signal spectrum (for AFGL and ERIM data) is assumed to be generated from an impulse:

$$S(k) = E_t \Delta x \quad (4)$$

where E_t is the target irradiance (in W/cm^2) and Δx is the sample interval. Table 7 gives seeker performance results in terms of required target irradiance for detection using the above method for all available AFGL scenes.²⁰ Three cases are given. The first uses the PSDs of the original data (background-plus-noise case that includes the collection scenes). The second performance result is the required target irradiance if only sensor noise from the forward-looking IR (FLIR) were present (FLIR-noise-only case). The AFGL FLIR internal noise is approximated by a flat PSD with a magnitude equal to the high spatial frequency portion of the PSD. Since the AFGL data always show sensor noise at high spatial frequencies, this internal noise estimate gives the sensor limitation. Finally, the third column (background-only case) gives an estimate of the background clutter limitation, assuming that the clutter PSD continues to decrease as $1/k^2$. Averages

¹⁸J. Schroeder, J. H. Schummers, B. P. Sandford, and W. J. Tropf, "Infrared Cloud Backgrounds," in *Proc. Tri-Service Infrared Background Symposium*, AFGL-TR-84-0094 (Mar 16, 1984).

¹⁹L. M. Howser and W. J. Tropf, "Investigation of Infrared Background Clutter," in *Research and Development Programs at The Johns Hopkins University Applied Physics Laboratory*, JHU APL Quarterly Report RQR 85-1 (Jan-Mar 1985).

²⁰W. J. Tropf, A. N. Vavreck, B. J. Sandford, J. H. Schummers, and J. Schroeder, "Infrared Cloud Backgrounds and Sensor Performance," in *Presentations at the Second Tri-Service Cloud Modeling Workshop*, IDA Report M-9, I, pp. 199-248 (Aug 1, 1984).

Table 7 Required target irradiance for matched filter detection in several AFGL cloud scenes.

Image	IFOV	Scene description	Required Target Irradiance (10^{-11} W/cm ²)		
			Background plus noise	FLIR noise only	Background only
I01	0.5 mrad	Down viewing cloud	3.98	2.96	1.81
I02		Down viewing and water	3.46	2.67	1.53
I03		Down viewing and terrain	8.36	6.46	4.80
I04		Down viewing and terrain	8.67	6.82	4.67
I05		Clouds and horizon	3.53	2.73	1.73
I06		Cloud deck	4.97	3.68	2.95
I07		Cloud structure	5.53	4.22	3.70
I08		Clouds and horizon	9.81	8.14	2.94
I09		Monument Valley	4.17	3.21	2.34
I10		Monument Valley	4.09	3.12	2.23
I11		Close clouds	3.39	2.71	1.50
I12		Close clouds	3.38	2.72	1.63
I13		Clouds and horizon	5.29	4.36	2.62
I14		Clouds and horizon	5.75	4.65	3.01
I16		Horizon and clouds	6.20	4.62	3.26
I17		Clouds and terrain	5.20	4.35	2.07
I18		Clouds and horizon	5.95	4.57	3.02
I19		Clouds and horizon	5.64	4.34	3.36
I20		Down viewing clouds	3.32	2.69	1.40
I31		Clouds below horizon	4.54	3.55	3.23
I32		Down viewing clouds	4.96	3.86	3.70
21-scene, 0.5-mrad average			5.23	4.12	2.74
I21	0.1 mrad	Structured clouds	0.147	0.110	0.070
I22		Structured clouds	0.152	0.107	0.083
I23		Structured clouds	0.175	0.131	0.106
I24		Structured clouds	0.150	0.122	0.072
I25		Structured clouds	0.171	0.134	0.084
I26		Structured clouds	0.154	0.118	0.077
I27		Structured clouds	0.165	0.125	0.084
I28		Structured clouds	0.160	0.127	0.077
I29		Structured clouds	0.144	0.114	0.063
9-scene, 0.1-mrad average			0.157	0.121	0.080

of the results for 21 AFGL scenes sampled at 0.5 mrad and for 9 AFGL scenes sampled at 0.1 mrad are given.

Similar matched-filter estimates were made using BMAP Montauk Point and Bedford No. 1 data. Since scanning seeker performance is dependent on resolution (i.e., IFOV), a matched-filter analysis with a variable seeker IFOV was conducted. Results for AFGL and BMAP cloud scenes are given in Fig. 7. The target irradiance required for detection is proportional

to the sensor instantaneous solid-angle FOV (square of linear FOV dimension). AFGL results for the 21 scenes with 0.5 mrad resolution and 9 scenes with 0.1 mrad resolution are shown as a shaded range of values. Results of two BMAP scenes are shown for comparison. Long-wavelength BMAP data are shown as thick solid lines and middle-wavelength results as thick dashed lines. The Montauk Point scene is overcast and has low contrast. The Bedford No. 1 is a hole in the

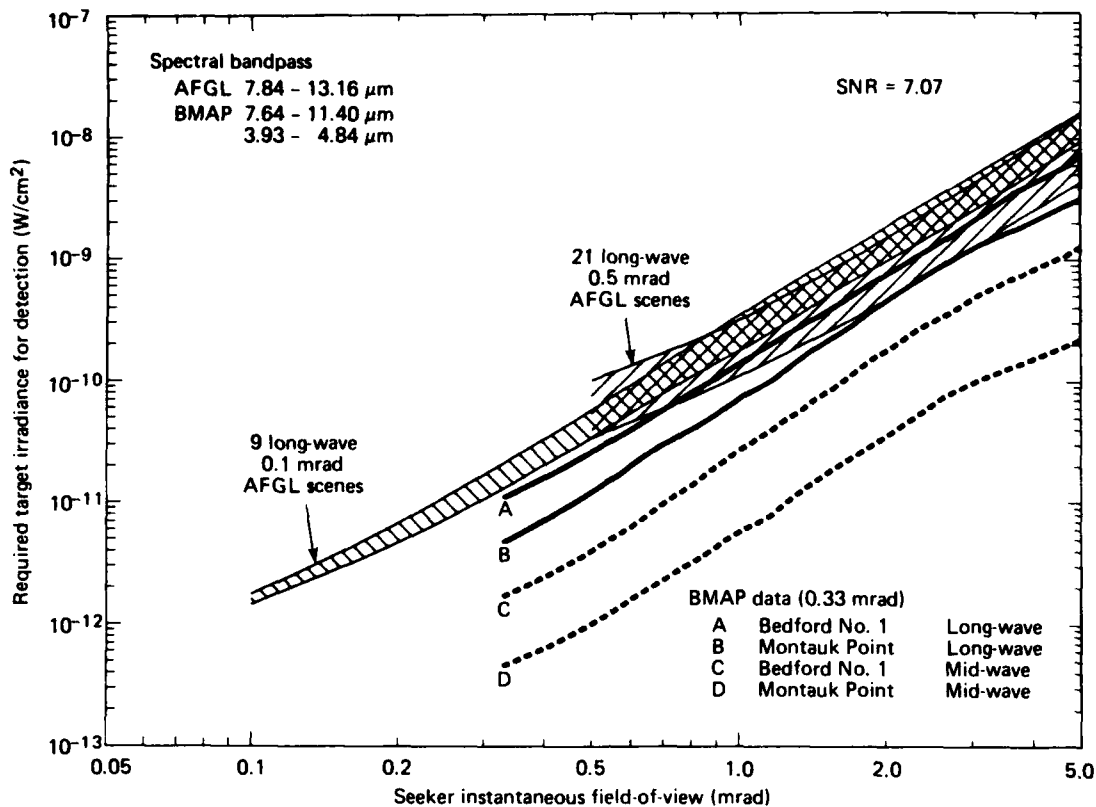


Figure 7 Required target irradiance for detection as a function of seeker resolution for AFGL and BMAP data.

clouds near the sun and has significantly higher contrasts. Note that long-wavelength clutter-limited results from both AFGL and BMAP data are comparable, although the overcast sky at Montauk Point gives lower clutter results.

A typical middle-wavelength seeker will have a spatial resolution of 0.5 to 1.0 mrad while the resolution of a long-wavelength seeker will be 1 to 2 mrad. Combining the difference in minimum detectable target signature and resolution results in approximately two orders of magnitude difference between the clutter noise of the middle- and long-wavelength bands.

An ideal bandpass filter was also applied to the Montauk data using the PSDs.²⁰ The response of an ideal bandpass filter is zero up to the cut-on of the filter. After the cut-on, the filter response is unity up to the cutoff. The cutoff of this bandpass was chosen to be the sensor-limited maximum frequency (1.5 cycles/mrad). The cut-on of the filter was varied from just above DC to the sensor-limited maximum frequency. The minimum detectable signal (or required target irradiance) was computed as a function of cut-

on frequency, assuming a signal-to-noise ratio of 7.07. Figure 8 shows a comparison of the matched-filter performance versus the ideal bandpass filter performance. Figure 8a is from the mid-IR data and 8b is from the long-IR data. Both parts of the figure show that the matched filter requires a lower target irradiance than the ideal bandpass filter. However, the ideal bandpass filter performance approaches the matched-filter performance for a bandpass cut-on that is approximately one-half of the cutoff frequency of the system.

Using the PSDs of some of the AFGL scenes, an ideal high-pass filter was applied to AFGL images.¹⁸ A high-pass filter was used for the AFGL data because the scene was sampled at the Nyquist rate. Therefore, the sensor-limited maximum frequency equaled the sampling frequency, and the higher frequencies did not need to be rejected. The results of the procedure were the same. The matched filter performed better than the ideal high-pass filter, but the performance of the high-pass filter again approached the matched-filter performance for a cut-on frequency of about one-half the cutoff frequency of the system.

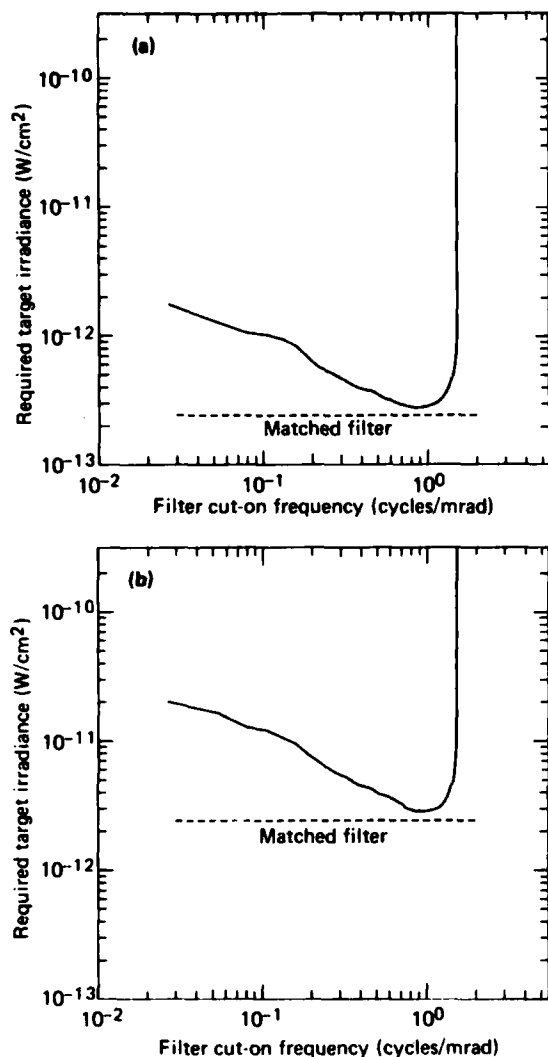


Figure 8 Comparison of required target irradiance for ideal bandpass filters to the matched-filter result using BMAP data. (a) Required target irradiance for BMAP mid-IR images. (b) Required target irradiance for BMAP long-IR images.

The matched filter and ideal high-pass or bandpass filter results give a first-order approximation to seeker performance. However, these results assume that the scene is Gaussian and stationary. The stationary assumption requires that the power spectrum and statistics of the scene are independent of the location within the scene. If the PSD is dependent on the location within the scene, then the scene average PSD is not a valid representation. Also, the PSD characterization of the scene only includes a measure of the

scene mean and variance, not higher moments. If the scene is Gaussian the mean and variance of the scene totally describe the scene statistics. However, if the scene is not Gaussian (as is usually the case), higher moments are needed.

Since real scenes violate the Gaussian and stationary assumptions, actual performance (e.g., true-false alarm rate) must be determined by direct processing of the raw background data. The following sections of the report describe a procedure used to process the raw background images.

4.3 Digital-Filter Performance Analysis

In theory, a matched filter applied to the IR data would maximize the signal-to-noise ratio of a point target in the scene. Since the assumptions on which matched-filter theory is based do not apply to IR clutter, direct filtering of the raw scene data with a digital filter that approximates a matched filter can be used to estimate detection system performance.

Since the signal (point-source) spectrum is approximately white, the input clutter is whitened by a digital high-pass filter that approximately whitens the clutter and therefore represents a matched filter.²¹

Since the BMAP frequency data extend beyond the signal (point-source) spectrum, an additional low-pass filter is needed to eliminate sensor noise. The additional filter was applied to the BMAP data to eliminate data lying between 1.5 and 5.0 cycles/mrad spatial frequency.

It was mentioned earlier that the PSDs of the point-source characteristics of the AFGL and ERIM data collection instruments were close to flat spectrums because the data were taken at the Nyquist frequency; therefore, no filtering beyond the clutter-matched filter was needed with the AFGL and ERIM data.

The matched filters needed for these images were applied to the PSDs shown in Figs. 3 to 5. A Butterworth digital filter was selected to evaluate the IR images.²² A first-order high-pass filter was used because it approximately matched the rolloff of the background PSDs and therefore approximated the matched filter of the previous section. PSDs of the AFGL and ERIM filtered images are approximately flat. The BMAP PSDs were not completely flat because of the second-order, low-pass filter that was also applied.

The cut-on of the filters was chosen on the basis of the point where the PSDs of the images began to

²¹L. M. Howser, *Analysis of Background Measurement and Analysis Program (BMAP) IR Images*, JHU/APL FIF(2)85-U-035, Rev 1.

²²G. L. Turin, "An Introduction to Matched Filters," *IEEE Trans. Information Theory* IT 6, 311-329 (Jun 1960).

flatten. Table 6 lists the system cutoff frequencies for the data and the frequencies at which the PSDs begin to flatten for a number of scenes. These frequencies were used to choose the cut-on of the highpass filters. For the BMAP data, the system Nyquist sampling spatial frequency of 1.5 cycles/mrad was chosen as the cut-on frequency. Since the AFGL image flattened at 0.3 cycles/mrad, 0.25 was chosen as the filter cut-on frequency. (Since the specified cut-on frequency is 3 dB down for a first-order high-pass filter, by choosing the cut-on frequency to be slightly less than the

frequency at which the PSD is flat, the output PSD should be approximately flat.) The ERIM cut-on frequencies were chosen for the same reasons. That is, knowing the frequencies where the input PSDs flattened, the cut-on frequencies were chosen to whiten the output PSD.

Table 8 lists the filters and the corner frequencies used. Figures 9 through 11 show the filters used in this analysis. Figure 9 shows the BMAP bandpass filter, Fig. 10 shows the AFGL high-pass filter, and Fig. 11 shows the ERIM high-pass filter.

Table 8 Digital filters used in the performance analysis.

Data source	HFOV (mrad)	Low-pass filter	High-pass filter	Corner (cycles/mrad)
BMAP	0.33	2nd order	1st order	1.5
AFGL	0.5	None	1st order	0.25
ERIM	2.0	None	1st order	0.1
ERIM	2.5	None	1st order	0.07

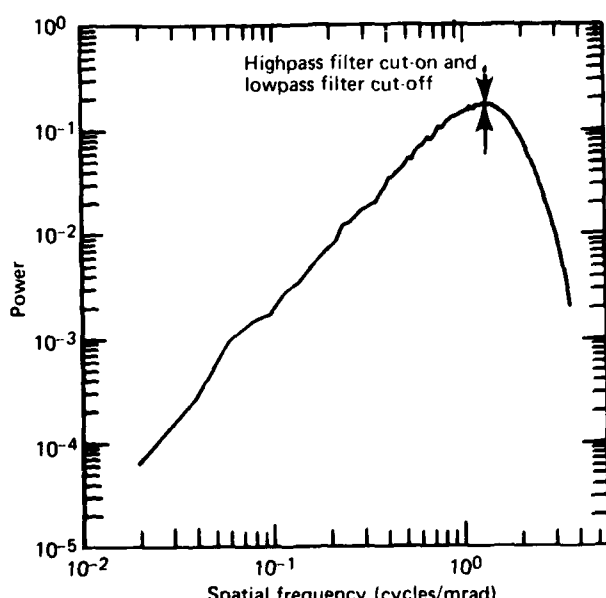


Figure 9 BMAP bandpass filter: second-order low-pass, and first-order high-pass (corner = 1.5 cycles/mrad).

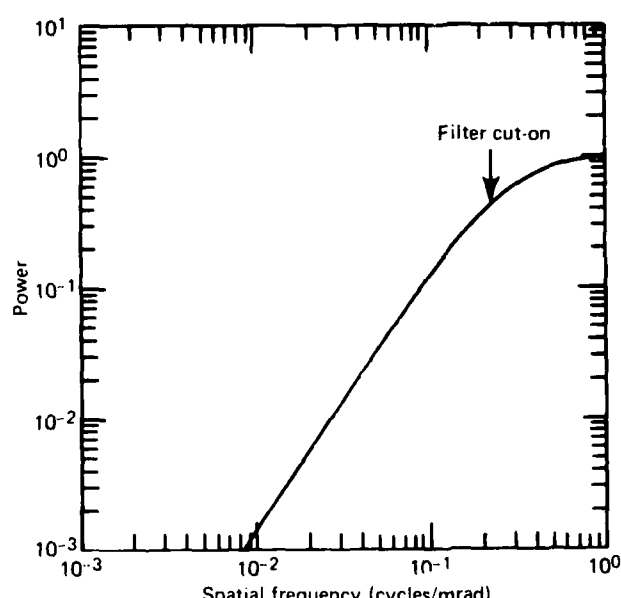


Figure 10 AFGL first-order high-pass filter (cut-on = 0.25 cycle/mrad).

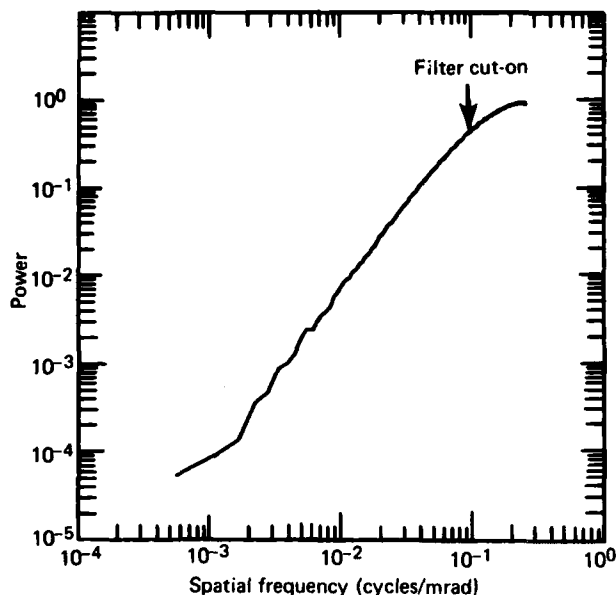


Figure 11 ERIM first-order high-pass filter (cut-on = 0.1 cycle/mrad).

Figures 12 through 14 show the PSDs of three images after filtering. Figure 12 shows the PSD of the BMAP Montauk long-IR data after filtering with the combination of a second-order, low-pass filter and a first-order, high-pass filter. This PSD can be compared to the long-IR PSD in Fig. 3 and the PSD of the point-source characteristic in Fig. 6. The comparison with Fig. 6 shows that the filtered PSD does look like the Fourier transform of the point-source characteristic, as expected after applying the matched filter. Figures 13 and 14 show the PSDs of the AFGL and ERIM images. These PSDs can be compared to the PSDs in Figs. 4 and 5. The two figures show that the high-pass filters did approximately flatten the background PSDs. Appendix E shows the PSDs of the remaining images.

The reason for applying the filtering was to maximize the signal-to-noise ratio by minimizing the clutter. Flattening the PSD of the background image reduces the energy of the low-frequency objects and does not affect the high-frequency objects. Point target signals, which are predominately of high-frequency content, therefore remain almost unaffected.

Figures 15 and 16 demonstrate the effect of the filtering. Figure 15a shows line 471 of ERIM scene S01CH1. This line contains no point targets. Figure 15b shows the same line after filtering, now all of the low-frequency features in the line have been attenuated. Figure 16a shows line 471 from ERIM scene

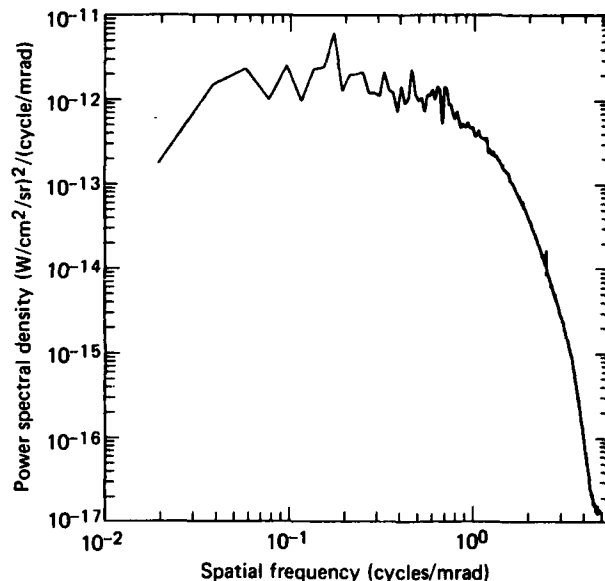


Figure 12 Power spectral density of BMAP Montauk Point long-wavelength background data after bandpass filter.

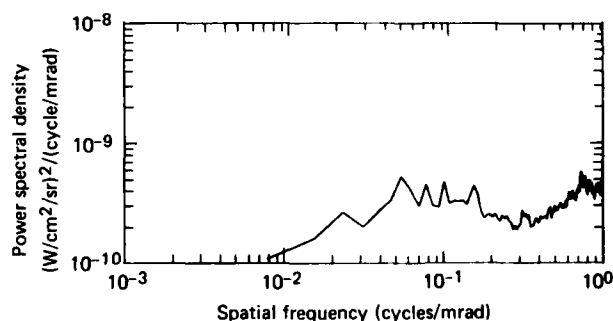


Figure 13 Power spectral density of AFGL cloud and terrain background scene 105 after high-pass filter.

S01CH3. This line has some possible point targets present. Figure 16b shows the same line after filtering; most of the image features have been attenuated, but the possible point targets are almost unaffected by the filter. Figure 16c shows an enlargement of the area around the possible point targets, giving a better view of the filtered output.

The previous figures have shown that the filtering applied to the background images reduce the amplitude of image features when possible targets are not present. Also, the mean of all of the images are removed when high-pass filters are applied.

Table 9 shows the maximum and minimum radiance of the scenes used in this study, after filtering. The values can be compared to the values in Table 5. A comparison of the tables shows that except for two scenes, the difference between the maximum and minimum scene radiance values before filtering is greater than the difference after filtering. Figures 15 and 16 show that this result is expected.

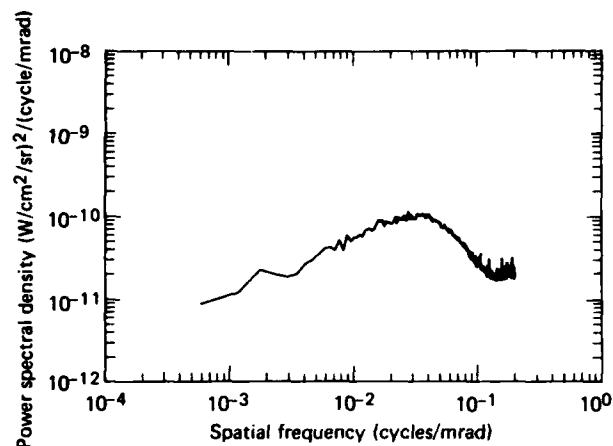


Figure 14 Power spectral density of ERIM Port Hue-neme scene in 2.0-2.6 μm spectral band (scene S23CH1) after high-pass filter.

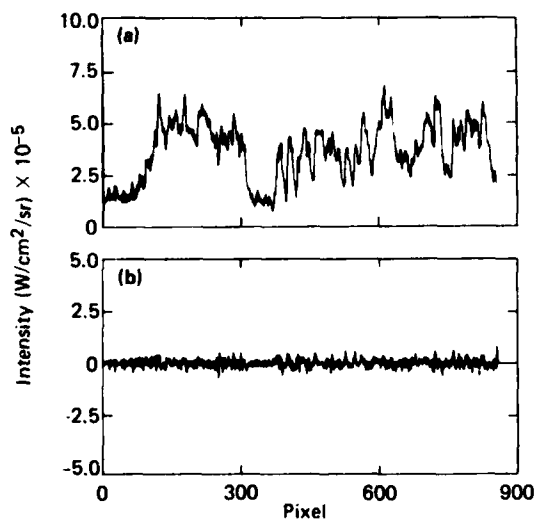


Figure 15 Line 471 of ERIM Camp A.P. Hill morning scene in 2.0-2.6 μm spectral band (scene S01CH1). (a) Unprocessed line of scene. (b) Line of scene after high-pass filter.

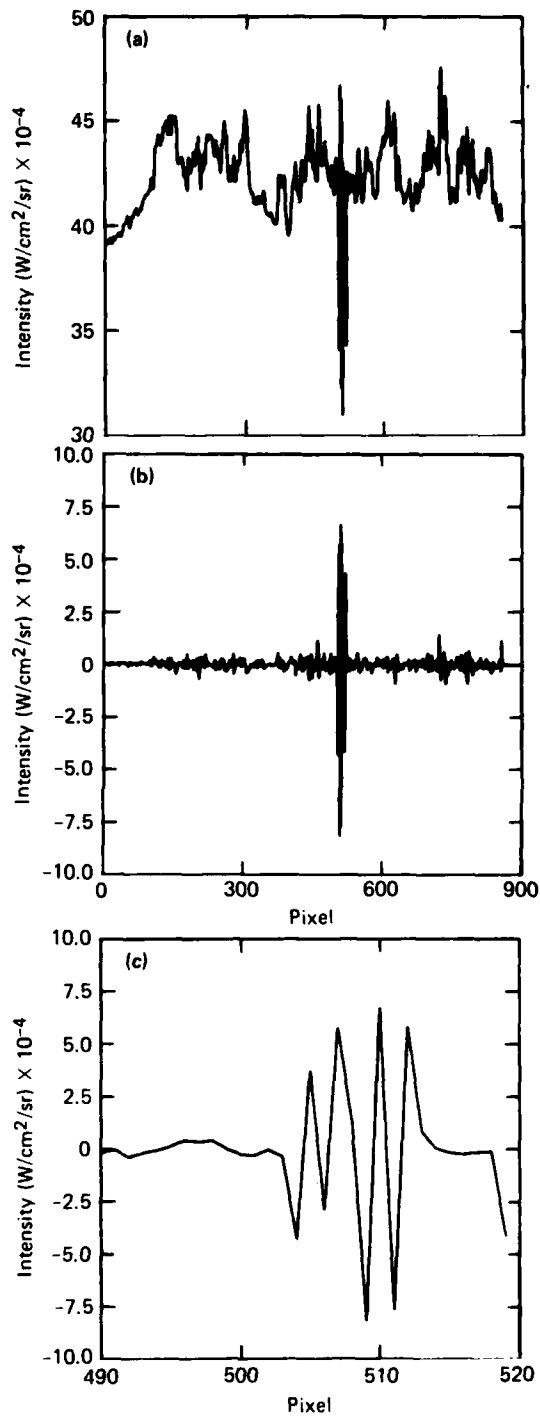


Figure 16 Line 471 of ERIM Camp A.P. Hill morning scene in 8.0-14.0 μm spectral band (scene S01CH3). (a) Unprocessed line of scene with data artifact. (b) Line of scene after high-pass filter. (c) Expanded line of scene after high-pass filter.

Table 9 Statistics of background data after filtering in units of $W/cm^2/sr$.

Scene	Maximum	Minimum	Δ (max - min)
BMAP-Montauk (long IR)	1.93×10^{-5}	-0.94×10^{-6}	2.87×10^{-5}
BMAP-Montauk (mid IR)	1.27×10^{-6}	-1.46×10^{-6}	2.73×10^{-6}
BMAP-Bedford (long IR)	2.46×10^{-5}	-2.75×10^{-5}	5.21×10^{-5}
BMAP-Bedford (mid IR)	1.18×10^{-5}	-4.30×10^{-6}	1.61×10^{-5}
AFGL I01R	2.14×10^{-4}	-3.91×10^{-4}	6.05×10^{-4}
AFGL I04R	6.13×10^{-4}	-2.39×10^{-4}	8.52×10^{-4}
AFGL I05R	3.56×10^{-4}	-2.76×10^{-4}	6.32×10^{-4}
AFGL I09R	2.48×10^{-4}	-2.67×10^{-4}	5.15×10^{-4}
ERIM F8CH1	2.81×10^{-5}	-2.88×10^{-5}	5.77×10^{-5}
ERIM F8CH2	1.48×10^{-5}	-1.53×10^{-5}	3.00×10^{-5}
ERIM F8CH3	1.86×10^{-4}	-1.71×10^{-4}	3.57×10^{-4}
ERIM S01CH1	2.52×10^{-5}	-2.92×10^{-5}	5.44×10^{-5}
ERIM S01CH2	3.96×10^{-5}	-3.46×10^{-5}	7.42×10^{-5}
ERIM S01CH3	8.31×10^{-4}	-8.22×10^{-4}	1.65×10^{-3}
ERIM S02CH1	4.49×10^{-5}	-3.19×10^{-5}	7.68×10^{-5}
ERIM S02CH2	4.22×10^{-5}	-3.58×10^{-5}	7.80×10^{-5}
ERIM S02CH3	3.77×10^{-4}	-3.86×10^{-4}	7.63×10^{-4}
ERIM S03CH2	3.01×10^{-5}	-2.34×10^{-5}	5.35×10^{-5}
ERIM S03CH3	3.32×10^{-4}	-2.66×10^{-4}	5.98×10^{-4}
ERIM S23CH1	1.21×10^{-4}	-8.08×10^{-5}	2.02×10^{-4}
ERIM S23CH3	1.55×10^{-4}	-9.49×10^{-5}	2.50×10^{-4}
ERIM S23CH4	1.11×10^{-3}	-1.20×10^{-3}	2.31×10^{-3}

Figure 17 shows each of the images in Fig. 1 after filtering was applied. To see the results of the processing clearly, only a portion of each image is displayed. A pixel area of about 300×300 is displayed for each image. For the AFGL scene this is the entire image.

The images were created by first taking the absolute value of the data. Each of the images was then scaled from 0 to 255 with 0 equal to $0.0 \text{ W/cm}^2/\text{sr}$, and 255 equal to the maximum filtered radiance in the image. Each image was then thresholded to be consistent with succeeding processing. All levels below the threshold were set to black; all levels above the threshold were set to white. The thresholds for the seven scenes are shown in Table 10 in terms of the noise equivalent irradiance. This thresholding will be discussed later.

Using this thresholding, any negative or positive outputs of the filter that are greater than the threshold are white in the images. The BMAP image in Fig. 17a shows that about 50% of the figure is greater than the threshold. Figure 17b is mostly black with a much smaller percentage of pixels greater than the threshold. Figure 17c, d, and e shows the morning, afternoon, and evening scenes of Camp A.P. Hill, after filtering. Figure 17c and d shows only a small percentage of pixels above the threshold. Only a very few pixels are above the threshold in Fig. 17e.

One bad line is visible in the Port Hueneme scene of Fig. 17f. The high-pass filtering and thresholding have accented this bad line since it was not visible in Fig. 1f. Also shown in Fig. 17f are strong edges from the buildings in the scene. The ridges in the mountains of Fig. 17g also give strong edges after high-pass filtering.

4.4 Filtering and Pulse Discrimination Performance Analysis

After applying the filters, the next step in the procedure is a pulse discrimination algorithm. This step adds an additional false-alarm-rejection capability to suppress sharp but extended features such as edges and boundaries.²¹

Figure 18 shows the pulse width discrimination algorithm for the BMAP images. The lower part of the figure shows a point target (a near impulse). After filtering, this target produces two pulses, one positive and one negative, which is the impulse response of the bandpass filter. The magnitude of the spikes and the delay between the maximum and minimum are func-

tions of the order and the cutoff frequency of the filter.

The upper part of Fig. 18 shows a step input. This is used to simulate the edge of a cloud as seen by the sensor. After filtering, this artifact also produces a positive pulse but no corresponding negative pulse. Similarly, a negative step would produce a negative pulse but not a corresponding positive pulse.

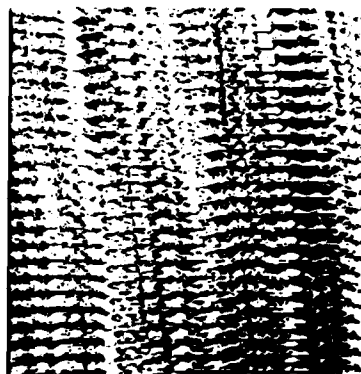
Any post-filtering threshold set to detect point targets could not distinguish between the point target and the step artifact impulses. To perform an additional discrimination between point and extended features, a pulse-width measurement algorithm is used. The pulse-width discrimination algorithm searches for any local maximum above a specified threshold. (The algorithm actually searches for a maximum or minimum since a target could be hotter or colder than the surrounding background. We will focus on the maximum in this discussion.) After finding a maximum, succeeding filter output is searched to find a corresponding minimum based on a given threshold. If a maximum and a corresponding minimum are both found, the point is declared to be a target; therefore, in Fig. 18 the point target would pass the discrimination logic and the step artifact would not pass.

Three parameters are needed for the pulse-discrimination algorithm. One parameter is the minimum-to-maximum ratio. This parameter requires that the absolute value of the minimum pulse that follows the local maximum passing the detecting threshold must be of some minimum size. The second parameter is the delay between the maximum and minimum values. Since this algorithm searches for point targets, the delay is small. The final parameter that must be specified is the detection threshold. To avoid processing sensor noise as possible targets, any pixel less than the detection threshold is not processed.

As discussed earlier, the selected filter determines the theoretical maximum for an impulse response and the delay between the maximum and minimum. For this reason the thresholds and delays used in this analysis varied depending on the filters used. In order to determine the appropriate thresholds and delays, various inputs were processed through the filters. The response of the filters to these inputs was used to determine the thresholds and delays. Since each set of data (BMAP, AFGL, and ERIM) had different filters this selection had to be performed for each data set.

Since the BMAP data were oversampled by the seeker, simply putting an impulse into the filtering would not be correct. Before filtering, the impulse was convolved with the point-source characteristic of the sensor, spreading the input into more than one output

²¹I. M. Howser, "Investigation of Infrared Background Clutter," in *Research and Development Programs at The Johns Hopkins University Applied Physics Laboratory*, JHU API Quarterly Report RQR/85-2 (Apr-Jun 1985).



(a)



(b)



(c)



(d)



(e)

ERIM images of Camp A.P. Hill (4.5-5.5 μm spectral band) after high-pass filter and 3.0 NEI threshold.



(f)



(g)

Figure 17 Images after filter and threshold. (a) BMAP middle-wave image from Bedford after bandpass filter and 1.5 NEI threshold. (b) AFGL scene 109 of Monument Valley after high-pass filter and 1.5 NEI threshold. (c) Morning (scene S01CH2). (d) Afternoon (scene S02CH2). (e) Evening (scene S03CH2). (f) ERIM image of Port Hueneme (4.5-5.5 μm spectral band) after high-pass filter and 10.0 NEI threshold (scene S23CH3). (g) ERIM image of mountains by Nellis AFB (3.9-4.7 μm spectral band) after high-pass filter and 3.0 NEI threshold (scene F8CH1).

Table 10 Thresholds used in Fig. 17.

Image	Maximum (W/cm ² /sr)	Threshold (W/cm ² /sr)	Threshold (LUT)	× NEI ¹
BMAP, Bedford, mid IR	1.18×10^{-5}	1.12×10^{-7}	2	1.5
AFGL (I09R)	2.67×10^{-4}	5.60×10^{-5}	53	1.5
ERIM1 (S01CH2)	3.96×10^{-5}	3.36×10^{-6}	22	3
(S02CH2)	4.22×10^{-5}	3.36×10^{-6}	20	3
(S03CH2)	3.01×10^{-5}	3.36×10^{-6}	29	3
ERIM3 (S23CH3)	1.55×10^{-4}	1.25×10^{-5}	21	10
ERIM5 (F8CH1)	2.88×10^{-5}	1.63×10^{-6}	14	3

¹ × NEI = times noise equivalent irradiance

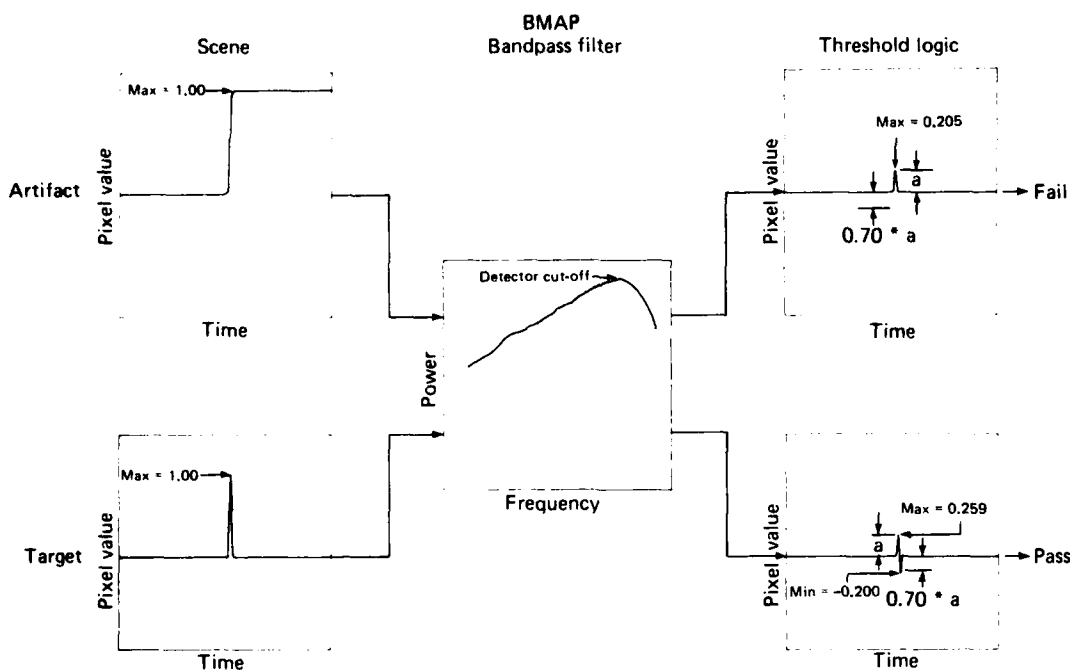



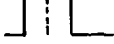
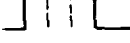
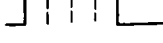
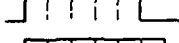
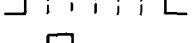
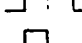
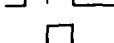
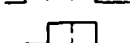
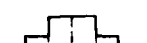


Figure 18 Pulse-width-discrimination algorithm for BMAP data.

point (performing a low-pass function on the impulse). The result of the convolution was filtered with the bandpass filter selected for the BMAP data. In addition to the impulse, other inputs were processed in the same way. After the inputs were processed, informa-

tion on the threshold and delays was obtained. Table 11 shows the results of this process.

Table 11 shows that an impulse that has been convolved with the BMAP point-source characteristic has a magnitude of about 0.25 times its original value af-

Table 11 Results of processing impulses with BMAP filters.

Input signal	Input max (convolved)	Output max	Output min	Max - min	Delay	Output min / Output max
	255.0	64.3	- 51.0	115.3	3	0.793
	468.7	125.9	- 91.2	217.0	4	0.724
	681.4	158.9	- 125.5	284.4	4	0.790
	793.6	186.7	- 145.7	332.4	4	0.780
	881.3	197.0	- 151.3	348.4	5	0.768
	921.6	200.0	- 150.7	350.7	6	0.754
	361.8	93.8	- 71.2	165.9	4	0.759
	362.3	95.2	- 68.2	163.4	3	0.716
	469.0	110.4	- 88.4	198.8	4	0.801
	575.4	139.8	- 105.5	245.3	3	0.755
	631.3	156.4	- 118.6	274.9	4	0.758
	574.9	142.4	- 108.4	250.9	4	0.761

ter filtering with the Butterworth bandpass filter. Also the ratio of the output minimum to maximum is 0.793. There is a 3-sample delay between the output maximum and minimum for the impulse input.

The second line of Table 11 shows the results for a two-pixel-wide input. For this input, the ratio of output minimum to maximum is 0.724 and the delay between the two is 4 samples.

The logic for the pulse discrimination algorithm was determined using the results in Table 11. A value of 0.70 was chosen for the ratio of the pulse-measuring threshold to the initial detected pulse. This value means that if a local maximum is found and the corresponding minimum is less than 0.70 times the maximum, that point will not be chosen as a target.

From Table 11 a delay of 3 or 4 samples was chosen for the algorithm. Any local maximum and minimum that is found that has a delay less than 3 or greater than 4 will not be chosen as a target. This restriction will eliminate wide artifacts (like the 5-sample-wide pulse in the table).

With the restrictions described, all of the wide features in Table 11 will not be chosen as targets. Only inputs less than 4 samples wide will pass this logic.

The only parameter that still needs to be defined for the BMAP images is the noise threshold. The threshold of images was set depending on the NEI of the seeker. The NEI of the system is, by definition, the irradiance required for a signal to have a magnitude equal to the rms noise within the system. The NEI of the BMAP, AFGL, and ERIM sensors are given in Table 3.

Since the threshold is defined in terms of the standard deviation of the noise of the system, the percentage of the image expected to be greater than the threshold can be computed using statistics tables. (This calculation assumes a normal distribution of the output levels.) If the threshold is set to be 3 NEI, 0.26% of the pixels are expected to be greater than the threshold. With a threshold of 1.5 NEI, 13.4% of the pixels would be expected to be greater than the threshold. For the analysis below, the detection threshold was

typically set at a low multiple of NEI to develop detection statistics in the small scenes that are available.

Figure 19 demonstrates the effect of pulse discrimination on one line of the Montauk long-IR image. Figure 19a shows the first line of the first frame of the long-IR Montauk image before any filtering. Figure 19b shows the same line of the image after the band-pass filter was applied. Notice that both axes have

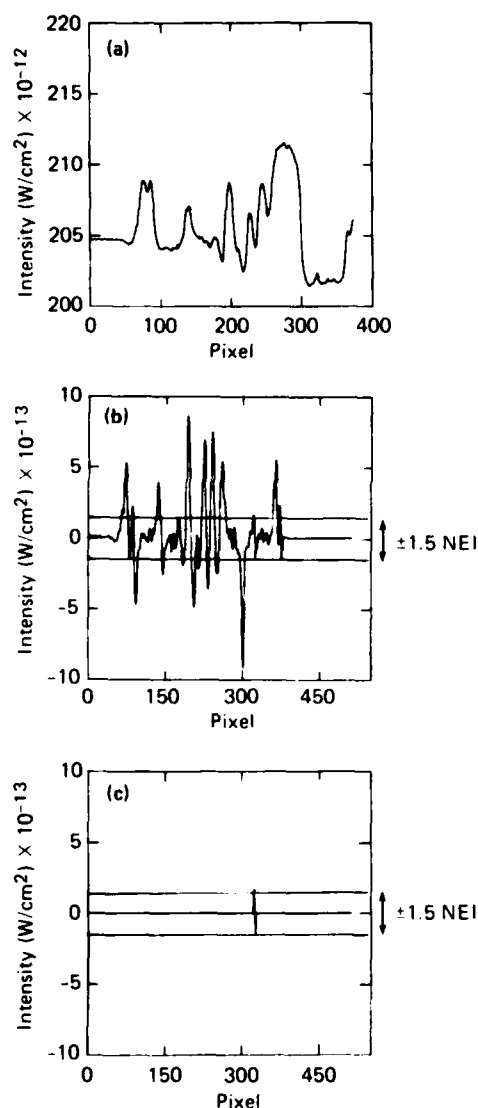


Figure 19 Line 1 of BMAP Montauk Point long-wavelength background data. (a) Unprocessed line of scene. (b) Line of scene after high-pass filter (with ± 1.5 NEI threshold). (c) Line of scene after high-pass filter and pulse discrimination (with ± 1.5 NEI threshold).

changed. The y-axis changed because the mean of the image was removed by the filtering. The x-axis changed because the image had to be padded with zeros to perform some of the processing. The horizontal lines in Fig. 19b show the ± 1.5 NEI threshold applied to the data, demonstrating that most of the pixels in the line are excluded from processing with a simple threshold. The pulse discrimination process is then needed to eliminate the remaining pixels. Figure 19c shows the same line of the image after pulse discrimination; all but one of the pulses that crossed the threshold have been eliminated by using the pulse discrimination. Also, the remaining pulse barely exceeds the threshold. If the threshold were increased to $2 \times$ NEI no pixels in this line would pass the discrimination logic.

No convolution of an input pulse with the sensor response function was needed for the AFGL data because no oversampling occurred with this seeker. Excluding this step, the same procedure was applied to the AFGL data as was applied to the BMAP data. Various inputs were processed with the AFGL high-pass filter and their results were tabulated. Table 12 shows the results.

Table 12 shows that the output minimum-to-maximum ratio was 0.586 for the impulse input. The delay between the maximum and minimum was 1 pixel (= one sample). These results show there is a large difference between the more realistic bandpass filter impulse of the oversampled BMAP data and the high-pass filtered impulse of data sampled at the Nyquist rate (i.e., AFGL and ERIM).

The parameters for the pulse discrimination algorithm were calculated from the results in Table 12. A ratio of 0.5 was selected for the minimum-to-maximum pulse height. A delay of 1 or 2 pixels was allowed between the maximum and minimum. This selection of parameters only passes 1- and 2-pixel-wide targets. No other features will pass this logic.

The threshold for the AFGL data was not as easy to pick as it was for the BMAP data. The scaling of the images was not set to the NEI of the system. The PSD of each image was needed to compute the NEI of the system. The PSD of each image flattened at the noise level of the system. The minimum value of each PSD in the flattened region was obtained from the plots. The threshold for the AFGL images was set at 3.0 NEI. Knowing the scaling of each of the images, the threshold in units of output levels was calculated. Table 13 lists the thresholds used for the AFGL images.

The filtering process was again repeated for the ERIM data. Two filters had to be applied to these images because the ERIM data had two spatial resolu-

Table 12 Results of processing impulses with AFGL filter.






Input signal	Input max	Output max	Output min	Max - min	Delay	Output min Output max
	256.0	181.0	-106.0	287.0	1	0.586
	256.0	181.0	-150.0	331.0	2	0.829
	256.0	181.0	-168.2	349.2	3	0.928
	256.0	181.0	-175.7	356.7	4	0.971
	256.0	181.0	-178.8	359.8	5	0.988

Table 13 Thresholds of AFGL images for pulse discrimination.

Scene	NEI (W/cm ²)	MF (W/cm ² /sr)	Threshold (3 × NEI) (output levels)
I01R	5.8×10^{-12}	8.4×10^{-6}	13.35
I04R	1.4×10^{-11}	2.1×10^{-5}	12.84
I05R	4.9×10^{-12}	8.4×10^{-6}	11.28
I09R	5.8×10^{-12}	1.1×10^{-5}	10.59



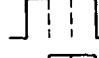
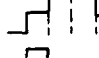
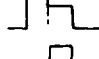
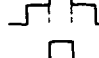


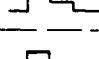
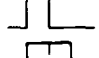


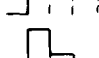
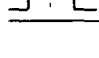
tions. Again, various inputs were processed through the filters and the results tabulated. Table 14 shows the results of the filtering. The first section of this table is for the ERIM1 data (filtered with a cut-on of 0.10); the second section is for the ERIM3 and ERIM5 data (filtered with a cut-on of 0.070).

The results in Table 14 were used to determine the parameters of the pulse-discrimination logic on the ERIM data. The ratios for ERIM3 images were slightly lower than the corresponding ratios for the ERIM1 images. For the impulse input, the ratio of the output minimum to output maximum was 0.84 for the ERIM1 filters and 0.75 for the ERIM3 and ERIM5 filters. Looking at Table 14 it can be seen that limiting the delay between maximum and minimum to 1 or 2 pixels eliminates some of the wider features from being considered a target. It would be desirable to set the minimum-to-maximum ratio to 0.70 (just below

the impulse ratio); however, this high threshold would eliminate the 2-pixel-wide pulse in line 5 of both sections of the table. The minimum-to-maximum ratio was therefore set to 0.50 in order to avoid eliminating possible targets from consideration.

The last parameter to be specified is the threshold for both sets of the ERIM data. Two methods were used in computing the NEI for these images. The first method used was the same as the AFGL calculation of the NEI. The minimum of the PSD was assumed to be the noise power. The NEI was computed from the power. The second method used the noise equivalent differential temperature of the sensor. Some of the ERIM spectral bands had a noise equivalent differential temperature (NE Δ T) already computed. Figure 20 shows a plot of the NE Δ T of some of the bands of ERIM data versus temperature. An average temperature of 285 K was assumed for the ERIM im-

Table 14 Results of processing impulses with ERIM filter.

Input signal	Input max	Output max	Output min	Max - min	Delay	$\frac{\text{Output min}}{\text{Output max}}$
	64.0	37.0	-31.0	68.0	1	0.84
	64.0	37.0	-36.0	73.0	2	0.97
	64.0	37.0	-37.0	74.0	3	0.99
	64.0	21.0	-21.0	42.0	3	0.995
	64.0	37.0	-20.0	57.0	2	0.55
	64.0	21.0	-20.0	51.0	2	0.97
	64.0	21.0	-33.0	54.0	1	1.57
	64.0	37.0	-28.0	65.0	2	0.76
	64.0	37.0	-22.0	59.0	1	0.59
	64.0	40.0	-30.0	70.0	1	0.75
	64.0	40.0	-37.0	77.0	2	0.93
	64.0	40.0	-39.0	79.0	3	0.98
	64.0	25.0	-24.0	49.0	3	0.96
	64.0	40.0	-22.0	62.0	2	0.55

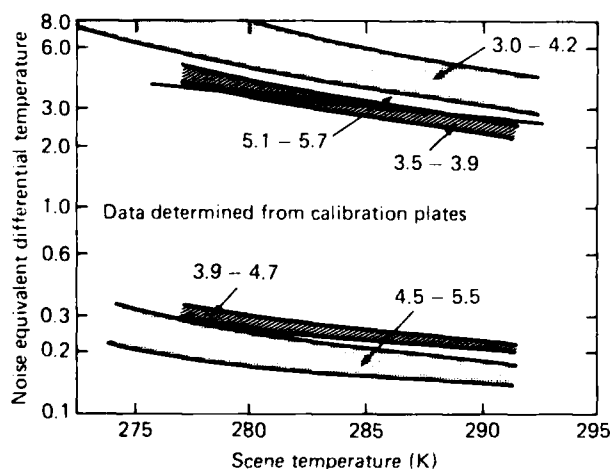


Figure 20 Typical derived $NE\Delta T$ values for the ERIM M-7 line scanner.

ages. Once the NEI was calculated for each image, the thresholds were computed. Table 15 shows the thresholds used for the ERIM images. The NEIs of the scenes marked were computed from the PSDs of the images. The remaining NEIs were computed from the $NE\Delta T$ of the image.

Each of the thresholds listed in Table 15 was a first choice in processing the data. For some scenes it was necessary to raise the threshold above 3 NEI/FOV to limit the number of pixels selected as targets. These cases will be discussed later.

The final parameters used for the pulse discrimination analysis are shown in Table 16, which lists the thresholds and delays used for each of the sets of data in this study.

All of the scenes were processed through the pulse-discrimination algorithm, using the parameters listed

Table 15 ERIM NEIs and thresholds.

Scene	NEI (W/cm ²)	FOV (circular) (mrad)	3 × NEI/(FOV) (W/cm ² /sr)	
S01CH1		2.0	3.68×10^{-6}	(from PSD)
S01CH2	4.47×10^{-12}	2.0	3.36×10^{-6}	
S01CH3		2.0	1.84×10^{-5}	
S02CH1		2.0	3.68×10^{-6}	(from PSD)
S02CH2	4.47×10^{-12}	2.0	3.36×10^{-6}	
S02CH3		2.0	1.16×10^{-5}	(from PSD)
S03CH2	4.47×10^{-12}	2.0	3.36×10^{-6}	
S03CH3		2.0	1.50×10^{-5}	(from PSD)
S23CH1		2.5	5.36×10^{-6}	(from PSD)
S23CH3	7.80×10^{-12}	2.5	3.74×10^{-6}	
S23CH4	4.63×10^{-11}	2.5	2.20×10^{-5}	
F8CH1	3.40×10^{-12}	2.5	1.63×10^{-6}	
F8CH2	8.83×10^{-12}	2.5	4.24×10^{-6}	
F8CH3	4.58×10^{-11}	2.5	2.20×10^{-5}	

Table 16 Pulse discrimination parameters.

Data source	Output min Output max	Delay (pixels)	Threshold (× NEI)
BMAP	0.70	3 or 4	1.5
AFGL	0.50	1 or 2	3.0
ERIM	0.50	1 or 2	3.0 ¹

¹Threshold started at 3.0 but had to be increased for some images.

in Table 16. The results of the processing are listed in Table 17, which lists the maximum and minimum of each of the images after this processing. Also list-

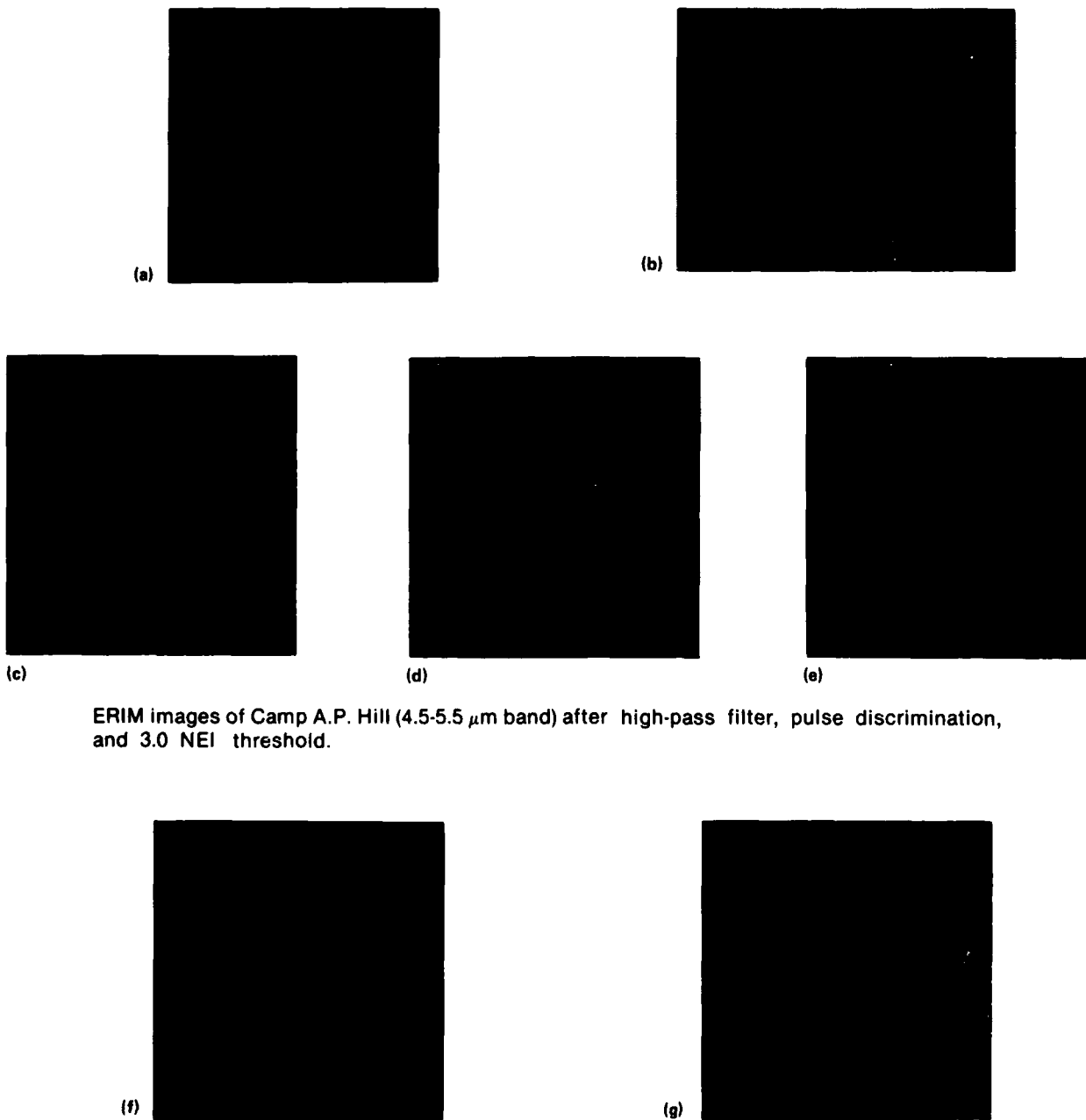
ed in Table 17 is the difference between the maximum and minimum. The threshold used (in W/cm²/sr) is listed in the following column. The threshold in NEI is listed in parentheses in the same column. The percentage of samples that passed this algorithm is listed in the last column.

Some of the images were processed twice through the pulse-discrimination algorithm. If too many pixels passed the logic the first time, the threshold was raised and the image was reprocessed. The results for all of these runs are also listed in Table 17.

Figure 21 shows the seven sample images after filtering and pulse discrimination. The same procedure as was used for the images in Fig. 17 was followed to threshold these images. Also, the same portion of each image was displayed to make possible direct comparisons between the images.

Table 17 Statistics of data after filtering and pulse discrimination in units of W/cm²/sr.

Image	Max	Min	Δ (max - min)	Threshold (\times NEI)	Pixels passed (%)
BMAP-Montauk (Far IR)	3.68×10^{-6}	-6.38×10^{-6}	1.01×10^{-5}	1.38×10^{-6} (1.5)	0.10
BMAP-Montauk (Mid IR)	1.23×10^{-6}	-6.0×10^{-7}	1.83×10^{-6}	2.75×10^{-7} (1.5)	0.10
BMAP-Bedford (Far IR)	6.18×10^{-6}	-5.44×10^{-6}	1.16×10^{-5}	1.5×10^{-6} (1.5)	0.04
BMAP-Bedford (Mid IR)	1.25×10^{-6}	-1.27×10^{-6}	2.52×10^{-6}	8.38×10^{-8} (1.5)	0.18
AFGL I01R	1.34×10^{-4}	-1.19×10^{-4}	2.52×10^{-4}	5.61×10^{-5} (1.5)	1.02
	1.34×10^{-4}	-1.19×10^{-4}	2.52×10^{-4}	1.12×10^{-4} (3.0)	0.01
AFGL I04R	1.80×10^{-4}	-2.43×10^{-4}	6.78×10^{-4}	1.35×10^{-4} (1.5)	0.07
	0	0	0	2.71×10^{-4} (3.0)	0
AFGL I05R	1.69×10^{-4}	-2.77×10^{-4}	4.46×10^{-4}	4.47×10^{-5} (1.5)	2.02
	1.69×10^{-4}	-2.77×10^{-4}	4.46×10^{-4}	0.48×10^{-5} (3.0)	0.05
AFGL I09R	1.37×10^{-4}	-1.29×10^{-4}	2.66×10^{-4}	5.61×10^{-5} (1.5)	1.6
	1.37×10^{-4}	-1.29×10^{-4}	2.66×10^{-4}	1.12×10^{-4} (3.0)	0.02
ERIM F8CH1	2.89×10^{-5}	-2.88×10^{-5}	5.77×10^{-5}	1.63×10^{-6} (3)	2.95
ERIM F8CH2	1.03×10^{-5}	-1.38×10^{-5}	2.41×10^{-5}	4.4×10^{-6} (3)	0.18
ERIM F8CH3	1.42×10^{-4}	-1.5×10^{-4}	2.92×10^{-4}	2.2×10^{-5} (3)	4.6
ERIM S01CH1	1.08×10^{-5}	-2.92×10^{-5}	4.0×10^{-5}	3.68×10^{-6} (3)	0.8
	1.08×10^{-5}	-2.92×10^{-5}	4.0×10^{-5}	4.91×10^{-6} (4)	0.14
ERIM S01CH2	1.56×10^{-5}	-1.07×10^{-4}	1.23×10^{-4}	3.36×10^{-6} (3)	0.31
ERIM S01CH3	8.31×10^{-4}	-8.22×10^{-4}	1.65×10^{-3}	1.84×10^{-5} (3)	3.1
	8.31×10^{-4}	-8.22×10^{-4}	1.65×10^{-3}	5.52×10^{-5} (9)	0.31
ERIM S02CH1	4.49×10^{-5}	-2.96×10^{-5}	7.45×10^{-5}	3.68×10^{-6} (3)	0.67
ERIM S02CH2	1.68×10^{-5}	-2.12×10^{-5}	3.80×10^{-5}	3.36×10^{-6} (3)	0.57
ERIM S02CH3	3.54×10^{-4}	-2.37×10^{-4}	5.91×10^{-4}	1.16×10^{-5} (3)	4.5
	3.54×10^{-4}	-2.37×10^{-4}	5.91×10^{-4}	5.0×10^{-5} (13)	0.11
ERIM S03CH2	1.13×10^{-5}	-4.08×10^{-6}	1.534×10^{-5}	3.36×10^{-6} (3)	0.01
ERIM S03CH3	2.99×10^{-4}	-9.57×10^{-5}	3.95×10^{-4}	1.5×10^{-5} (3)	1.8
	2.99×10^{-4}	-9.57×10^{-5}	3.95×10^{-4}	3.0×10^{-5} (6)	0.25
ERIM S23CH1	1.09×10^{-4}	-7.75×10^{-5}	1.86×10^{-4}	5.36×10^{-6} (3)	1.07
	1.09×10^{-4}	-7.75×10^{-5}	1.86×10^{-4}	1.07×10^{-5} (6)	0.19
ERIM S23CH3	1.05×10^{-4}	-9.16×10^{-5}	1.97×10^{-4}	1.25×10^{-5} (10)	0.33
ERIM S23CH4	1.11×10^{-3}	-1.20×10^{-3}	2.31×10^{-3}	2.2×10^{-5} (3)	3.8
	1.11×10^{-3}	-1.20×10^{-3}	2.31×10^{-3}	1.47×10^{-4} (20)	0.39



ERIM images of Camp A.P. Hill (4.5-5.5 μm band) after high-pass filter, pulse discrimination, and 3.0 NEI threshold.

Figure 21 Images after filter, pulse discrimination, and threshold. (a) BMAP middle-wave image from Bedford after bandpass filter, pulse discrimination, and 1.5 NEI threshold. (b) AFGL scene 109 of Monument Valley after high-pass filter, pulse discrimination, and 1.5 NEI threshold. (c) Morning (scene S01CH2). (d) Afternoon (scene S02CH2). (e) Evening (scene S03CH2). (f) ERIM image of Port Hueneme (4.5-5.5 μm spectral band) after high-pass filter, pulse discrimination, and 10.0 NEI threshold (scene S23CH3). (g) ERIM image of mountains by Nellis AFB (3.9-4.7 μm spectral band) after high-pass filter, pulse discrimination, and 3.0 NEI threshold (scene F8CH1).

The image in Fig. 21a shows that a very small percentage of the points passed the pulse-discrimination logic. The AFGL image (Fig. 21b) does not show a large reduction in the number of detected pixels; however, a reduction in the number of detected pixels is still evident. Figure 21c and d shows a large decrease in the number of pixels above the threshold. Only a very few pixels in Fig. 21e passed the threshold.

Figure 21f shows the same area as Fig. 17f. Only one or two of the building outlines passed the pulse discrimination. Many of the smaller points also passed the logic. The bad scan line is still visible in this figure.

Finally, Fig. 21g shows the mountains in the ERIM5 image. A comparison with Fig. 17g shows that some of the mountain ridges have been removed from the image. However, many of the single pulses were not removed from the image, a condition that would cause many false alarms with this algorithm.

4.5 Cross-Scan Comparison

The pulse-discrimination algorithm discussed in the previous section reduces the required target irradiance by analyzing the pulse shapes along the scan direction. A cross-scan comparison checks neighboring scan lines to find features that extend across several scan lines. If this analysis were performed, the number of false alarms could be reduced further.

A cross-scan comparison is more difficult to perform than the pulse-discrimination algorithm because the extended features could be at any angle relative to the scan direction. Only checking pixels perpendicular to the scan direction would not be sufficient. A method to recognize extended features at any angle would need to be developed.

No cross-scan algorithm was implemented for this analysis. The thresholded images in Fig. 21 were checked visually for any extended features. The inspection can tell qualitatively whether the required target irradiance would be reduced further by applying a cross-scan comparison after the pulse-discrimination algorithm.

For Fig. 21a through e, it is doubtful that a cross-scan comparison would further reduce the number of pixels that passed the discrimination logic. Few, if any, of the pixels in these images form a continuous line. However, in the port and mountain scenes in Fig. 21f and g the cross-scan comparison could eliminate some of the false alarms.

In Fig. 21f, one edge of each of two buildings is roughly outlined by false alarms. A cross-scan comparison could find these outlines and eliminate those samples from being considered possible targets.

A cross-scan comparison would also be useful in

Fig. 21g. Many short vertical lines are visible in this image. Also, a long, continuous feature is found on the right edge of the image. If these features could be removed from being considered possible targets, many of the false alarms in this image would be removed.

4.6 Comparison of Processing Techniques

The filtering and pulse discrimination logic were applied to these images to reduce the noise level of the background, thereby improving the signal-to-clutter ratio. One measure of the improvement is the minimum detectable signal. For the unprocessed images, the smallest signal that could be detected above the clutter would have to be greater than the maximum pixel in the image (or less than the minimum pixel if both a maximum and minimum threshold were set).

The minimum detectable signal for the images processed through only the filtering or processed through the filtering and pulse discrimination can be calculated from the maximum and minimum values of these images. It is shown in Tables 11, 12, and 14 that the maximum value of an impulse is reduced by the filtering. For example, in Table 11 the maximum of the input is 255.0 while the maximum of the output is 64.3. This gives an output-to-input ratio of about 0.25. Because of this effect, the minimum detectable signal for images that have been filtered is calculated by dividing the maximum (and minimum) values of the images by the ratio of maximum output to maximum input. This calculation produces the required signal into the filtering to produce the given maximum or minimum after filtering. Table 18 shows the factors used to calculate the minimum detectable signal. These values were computed from the impulse results in Tables 11, 12, and 14.

Table 19 lists the minimum detectable signal for each of the images in the study before any processing, af-

Table 18 Filtering output-to-input ratios.

Data source	Output/input
BMAP	0.252
AFGL	0.707
ERIM1	0.578
ERIM3, ERIM5	0.625

Table 19 Minimum detectable signal in units of $W/cm^2/sr$.

Image	Before processing		After filter		After filter and pulse discrimination	
	Max $-\mu$	Min $-\mu$	Max	Min	Max	Min
BMAP-Montauk (Far IR)	1.1×10^{-4}	-9.0×10^{-5}	7.66×10^{-5}	-3.72×10^{-5}	1.46×10^{-5}	-2.53×10^{-5}
BMAP-Montauk (Mid IR)	1.75×10^{-5}	-9.4×10^{-6}	5.04×10^{-6}	-5.79×10^{-6}	4.88×10^{-6}	-2.39×10^{-6}
BMAP-Bedford (Far IR)	1.0×10^{-4}	-3.6×10^{-4}	9.76×10^{-5}	-1.09×10^{-4}	2.45×10^{-5}	-2.16×10^{-5}
BMAP-Bedford (Mid IR)	8.7×10^{-5}	-3.24×10^{-5}	4.68×10^{-5}	-1.71×10^{-5}	4.96×10^{-6}	-5.04×10^{-6}
AFGL I01R	1.0×10^{-3}	-4.5×10^{-4}	3.03×10^{-4}	-5.53×10^{-4}	1.90×10^{-4}	-1.68×10^{-4}
AFGL I04R	6.2×10^{-4}	-1.07×10^{-3}	8.67×10^{-4}	-3.44×10^{-4}	2.55×10^{-4}	-3.44×10^{-4}
AFGL I05R	4.1×10^{-4}	-5.7×10^{-4}	5.04×10^{-4}	-3.91×10^{-4}	2.39×10^{-4}	-3.91×10^{-4}
AFGL I09R	6.60×10^{-4}	-4.8×10^{-4}	3.51×10^{-4}	-3.78×10^{-4}	1.93×10^{-4}	-1.82×10^{-4}
ERIM F8CH1	1.99×10^{-5}	-2.67×10^{-5}	4.62×10^{-5}	-4.61×10^{-5}	4.62×10^{-5}	-4.61×10^{-5}
ERIM F8CH2	1.59×10^{-5}	-1.27×10^{-5}	2.32×10^{-5}	-2.21×10^{-5}	1.65×10^{-5}	-2.21×10^{-5}
ERIM F8CH3	4.59×10^{-4}	-4.3×10^{-4}	2.98×10^{-4}	-2.74×10^{-4}	2.27×10^{-4}	-2.40×10^{-4}
ERIM S01CH1	6.4×10^{-5}	-3.6×10^{-5}	4.36×10^{-5}	-5.05×10^{-5}	1.87×10^{-5}	-5.05×10^{-5}
ERIM S01CH2	1.2×10^{-4}	-3.0×10^{-5}	6.85×10^{-5}	-5.99×10^{-5}	2.70×10^{-5}	-1.85×10^{-5}
ERIM S01CH3	1.8×10^{-3}	-1.1×10^{-3}	1.44×10^{-3}	-1.42×10^{-3}	1.44×10^{-3}	-1.42×10^{-3}
ERIM S02CH1	9.3×10^{-5}	-3.7×10^{-5}	7.77×10^{-5}	-5.25×10^{-5}	7.77×10^{-5}	-5.12×10^{-5}
ERIM S02CH2	1.2×10^{-4}	-3.0×10^{-5}	7.30×10^{-5}	-6.19×10^{-5}	2.91×10^{-5}	-3.67×10^{-5}
ERIM S02CH3	1.2×10^{-3}	-4.0×10^{-4}	6.52×10^{-4}	-6.68×10^{-4}	6.12×10^{-4}	-4.10×10^{-4}
ERIM S03CH2	3.8×10^{-5}	-1.9×10^{-5}	5.21×10^{-5}	-4.04×10^{-5}	1.96×10^{-5}	-7.06×10^{-6}
ERIM S03CH3	9.0×10^{-4}	-4.0×10^{-4}	5.74×10^{-4}	-4.60×10^{-4}	5.17×10^{-4}	-1.66×10^{-4}
ERIM S23CH1	2.22×10^{-4}	-3.8×10^{-5}	1.94×10^{-4}	-1.29×10^{-4}	1.74×10^{-4}	-1.24×10^{-4}
ERIM S23CH3	2.4×10^{-4}	-6.8×10^{-5}	2.48×10^{-4}	-1.5×10^{-4}	1.68×10^{-4}	-1.46×10^{-4}
ERIM S23CH4	2.2×10^{-3}	-7.5×10^{-4}	1.78×10^{-3}	-1.92×10^{-3}	1.78×10^{-3}	-1.92×10^{-3}

ter filtering, and after filtering and pulse discrimination. Since the means of the images are removed by the filtering the means of the before-processing images have been subtracted from the maximum and minimum values. Therefore, this table shows the spread about the mean radiance in the before-processing column and the spread about 0.0 in the remaining columns.

Figure 16 shows the relationship between the before-processing results and the after-filtering results. Since the low-frequency features are present in the original images, any spike present in the image might be hidden by the low-frequency features. Therefore, the maximum and minimum values in this column might not relate to spikes in the images. On the other hand, the low-frequency features are removed from the filtered images. The maximum and minimum values are necessarily from spikes in the image. For these reasons the maximum or minimum after filtering could be greater than in the original image.

Figure 22 displays the results of Table 19. The figure shows only the positive minimum required irradiance

ance values for the BMAP, AFGL, and ERIM images. The required irradiance before processing, after filtering, and after filtering and pulse discrimination are plotted with different symbols. Also plotted on this figure are the minimum required irradiance values from the application of the matched filter to the PSDs of the BMAP and AFGL images.

To analyze the results in Table 19 and Fig. 22 the data must first be broken into subsets. The BMAP images were all of cloud backgrounds. Table 19 shows that the minimum detectable signal of these images was reduced by the filtering. For all four of these images the pulse discrimination algorithm further reduced the required signal. Figure 23 shows a histogram of these results. Three histograms of the Bedford mid-IR data are presented in this figure—the original image (with the mean subtracted), the image after filtering with a first-order high-pass and a second-order low-pass filter, and the image after filtering and pulse discrimination. The figure shows a large reduction in the maximum and minimum owing to the filtering. The smaller reduction owing to the pulse discrimination is also seen.

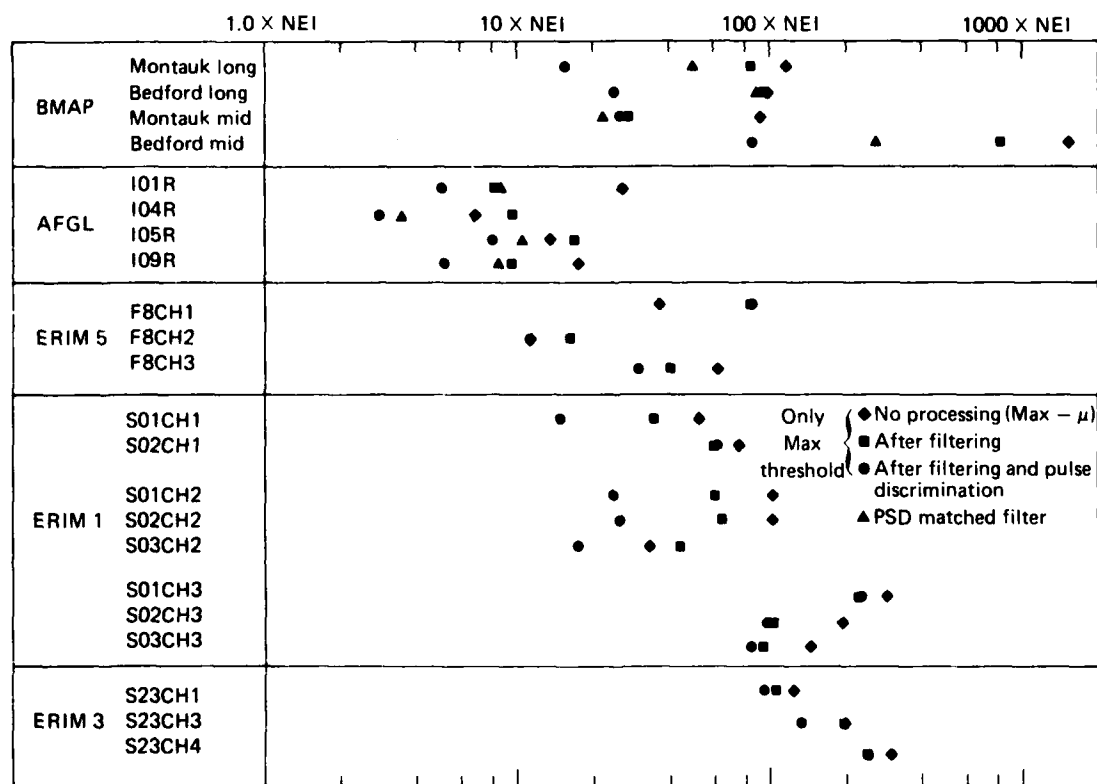


Figure 22 Comparison of processing techniques.

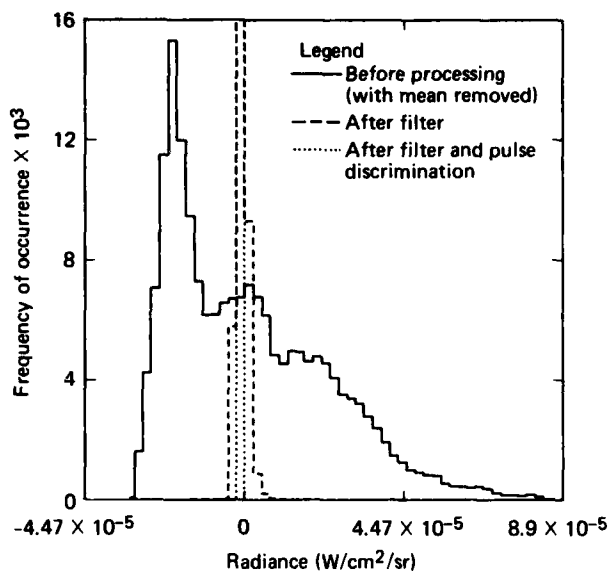


Figure 23 Histograms of BMAP mid-IR Bedford scene.

Figure 24a and b further demonstrates the effect of the pulse discrimination and filtering on the IR scenes. This figure shows a cumulative histogram for the unprocessed image, the image after filtering, and after filtering and pulse discrimination. Figure 24a shows these histograms for AFGL scene I09R and Fig. 24b shows the histograms for ERIM (S01CH2). The ordinate of these plots is the cumulative frequency of occurrence. Two scales are drawn along the abscissa—the irradiance and the NEI. This plot indicates where the NEI or irradiance threshold must be set to get no false alarms for these two scenes. These plots again show the decrease in the required irradiance owing to filtering and filtering with pulse discrimination.

Figure 22 shows that for the BMAP scenes the matched filter usually requires a lower target irradiance than is required by the Butterworth filter. However, the Butterworth filter followed by the pulse-discrimination algorithm usually performs better (i.e., requires a lower target irradiance) than the matched filter. This unexpected result is probably attributable to the higher threshold used in the matched filter analysis. The matched-filter threshold was much higher than needed to eliminate all false alarms in these small scenes.

Scene I01R was the only processed AFGL image that contained only clouds. The results in Table 19 show that the filtering and pulse discrimination did reduce the minimum detectable signal. The remaining AFGL

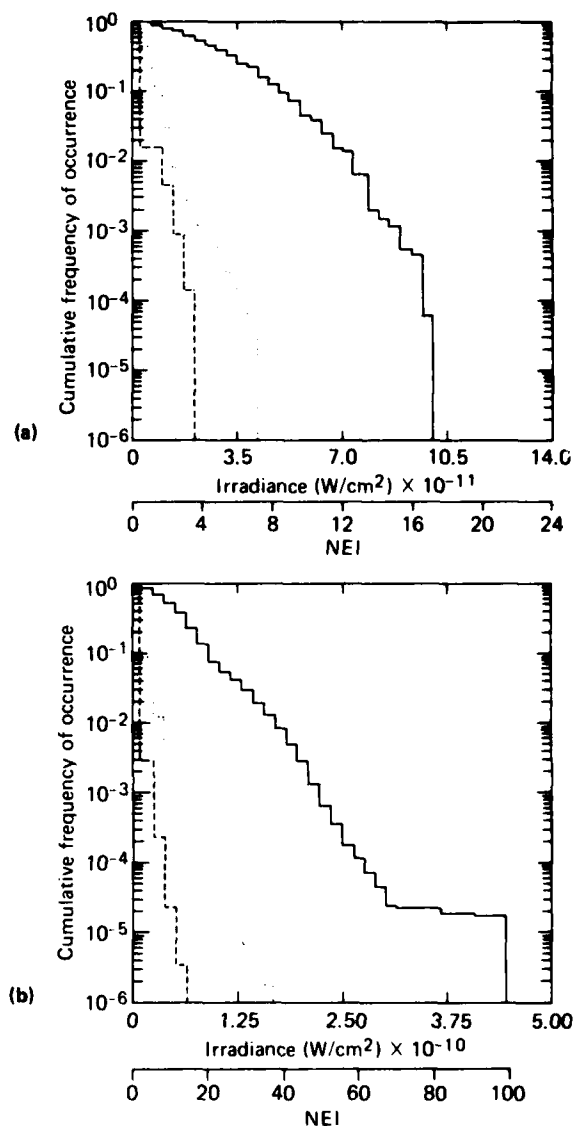


Figure 24 Cumulative histograms showing reduction of maximum irradiance and NEI from filtering and pulse discrimination. (a) Histograms of AFGL Monument Valley and cloud scene (I09R). (b) Histograms of ERIM Camp A.P. Hill morning scene 4.5-5.5 μm spectral band (scene S01CH2).

scenes had clouds and terrain in the images. Scene I09R shows a decrease in the required signal for the filtering and the pulse discrimination. Scenes I04R and I05R

show a reduction owing to the filtering, but the pulse discrimination does not further reduce the negative required signal. This result means that there were large negative pulses in the images that passed the filtering and the pulse discrimination. This result is expected to be more common for terrain images than for cloud images.

For all four of the AFGL scenes, the Butterworth filter followed by the pulse discrimination performed better than the matched filter applied to the PSD.

The ERIM data must be broken into many parts for analysis. The ERIM5 images used in this analysis (F8CH1, F8CH2, and F8CH3) were of mountains. The results in Table 19 show that in some cases the pulse discrimination further reduced the minimum required signal, but the value often remained almost the same.

The set of images from ERIM1 (S01 through S03) can be discussed by band. One of the channel 1 images shows very little decrease in the minimum detectable signal when pulse discrimination is added. Channel 2 images, on the other hand, all show a significant decrease in false alarms when the pulse discrimination is added. Some of the channel 3 images show a decrease in the maximum or minimum clutter pulses but other images show little or no change because of the pulse discrimination.

Scene 23 from ERIM3 had two bad lines in the image. Figure 25 shows three lines of the image. Figure 25a shows a normal line in channel 3 (line 1) of the image. Figure 25b and c shows lines 18 and 641 of channel 3. These plots show that there is something wrong with these two lines of data, a problem that was not found until after the pulse discrimination algorithm was applied and hundreds of points from each of these lines passed the discrimination logic. Channels 3 and 4 of scene 23 had bad data in both of these lines. Channel 1 had bad data in only line 641. Because of these bad data, the results in Table 19 and Fig. 22 are not expected to show a significant decrease resulting from the pulse discrimination.

The results from Table 19 can be related to the results from Table 17. In Table 19 the BMAP data (clouds) showed a large decrease in the minimum detectable signal owing to filtering and pulse discrimination. The results in Table 17 agree with these results in that less than 0.2% of the pixels in the images passed the discrimination logic with the threshold set at 1.5 NEI. Many more of the AFGL pixels passed the logic. This result can again be associated with the scene content.

Fewer points passed the pulse discrimination logic for channel 2 of ERIM scenes S01, S02, and S03 than

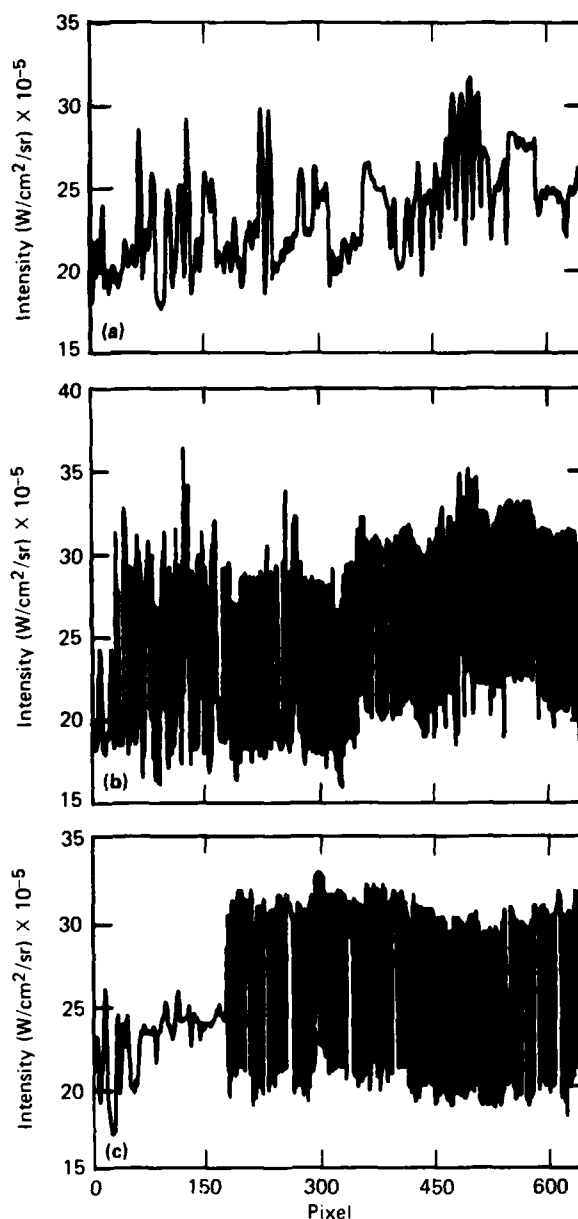


Figure 25 Lines of images from ERIM Port Hueneme scene in 4.5-5.5 μm spectral band (scene S23CH3) showing bad scan lines. (a) Line 1 of scene with no bad data. (b) Line 18 of scene with entire line of bad data. (c) Line 641 of scene with partial line of bad data.

for channels 1 and 3, consistent with the results in Table 19.

The bad scan lines in scene S23 affect the results in Table 17. To get about 0.3% of the points to pass

the logic, the threshold had to be raised to 20 NEI for one of the channels, agreeing with the results in Table 19 where little to no improvement was gained with the pulse discrimination. This result shows that most of the bad points passed the filtering and the pulse discrimination.

4.7 Implementation of the Scanning Sensor Processing

The previous sections of this report described the applications of clutter suppression algorithms to digital infrared images. This section briefly summarizes implementation of the algorithms in a missile guidance system.

Figure 26 shows a block diagram of one potential seeker-processing configuration that implements the scanning-sensor algorithms developed in this report. The detected scene (plus target) is preamplified and prefiltered. The prefilter suppresses high frequency (out of the seeker bandpass) and may also be used to suppress the detector DC output. The resultant video signal from each channel is then digitized in an A/D converter. The converter has a dynamic range of 14 to 16 bits (or as few as 8 bits for AC-coupled long-wavelength sensors), and samples at two to three times the Nyquist rate. The output digital signal is then available for clutter suppression algorithm implementation.

The digital signal is first processed with a bandpass filter that is matched to the clutter spectrum and the spatial filter at the scanning detector. Filtered output is then thresholded at approximately five to ten times the sensor NEI to eliminate most of the internal noise. Data above threshold are a detection. Data below

threshold are preserved for use in the pulse-width discrimination algorithm. In general, both positive and negative thresholds are implemented to detect targets of both contrasts.

After thresholding, each detection is pulse-width tested by looking for the corresponding pulse of the opposite sign, appropriate magnitude, and appropriate delay. The exact implementation of this pulse-width discriminator is dependent on the filtering and noise level. Tolerance on the magnitude of the second pulse for point-target confirmation can be computed readily from the measured first pulse magnitude and the known (or real-time measured) system noise. At this point the data are compressed and only detections are preserved.

The final step in the discrimination algorithm is comparison of the detected output at adjacent detector channels. Detections (passing threshold and pulse-width discrimination) that span typically three or more adjacent channels within two or three time samples of one another are declared false targets. If the detectors are offset and if they overlap across the scan direction, the detection of false targets is made easier. With this configuration, a false target would be detected in three or more contiguous channels. This would eliminate the necessity for checking channels two or three time samples apart.

Outputs of all the detector channels may also be used to raise the detection threshold adaptively, on the basis of occurrence of many false alarms within a scan frame (or segment thereof). When the number of detections per frame becomes large, a momentary increase in detection threshold may be necessary to

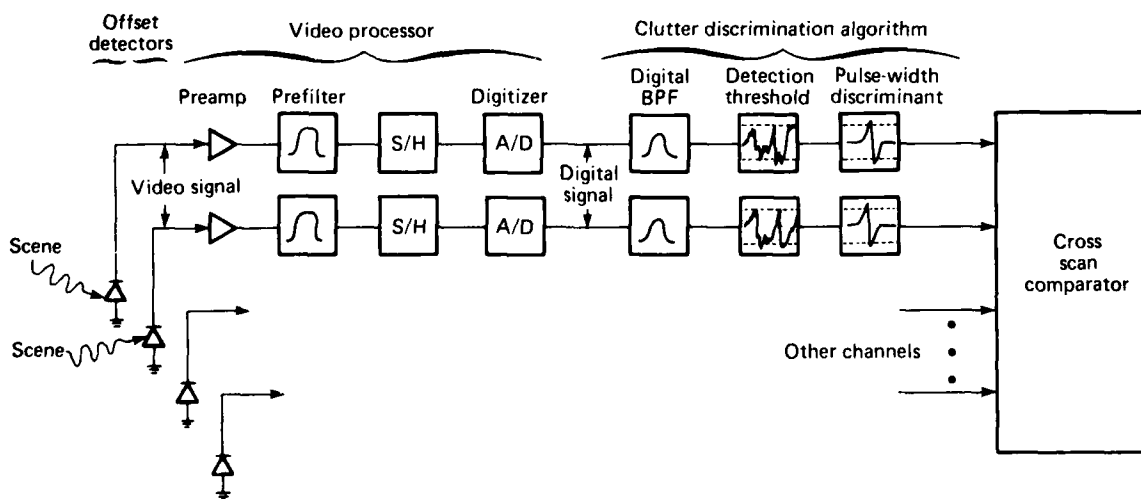


Figure 26 Implementation of the scanning sensor processing.

discriminate against clutter patches during search. Once in track, different algorithms would be used to discriminate against the appearance of decoys so as

to avoid the raising of the threshold while tracking a valid target.

5.0 CONCLUSIONS

The performance of a scanning sensor in background clutter has been investigated. A number of background scenes, supplied by three separate measurement programs, have been characterized in terms of artifacts, imagery, scene radiance statistics, and power spectral density.

Available scene data were processed in several ways to determine the minimum target signature that can be detected in particular scenes. Two techniques were used to derive performance. The first used the scene power spectral density to estimate required target irradiance as a function of sensor resolution (IFOV) assuming a fixed threshold based on a matched-filter (maximum signal-to-noise) analysis.

Since the matched-filter results are based on assumptions that are not met by real scenes, direct processing of the scenes is also done. The analysis includes three levels of scene processing in much the same way as a sensor signal processor detection system. These three levels are:

1. A high-pass, first-order digital filter that whitens the clutter power spectral density and approximately maximizes the target signal-to-clutter ratio. The result is directly comparable to the matched-filter results but gives a better estimate of false-alarm rate. The filter provides good dis-

crimination against large, low-frequency scene features.

2. A high-pass filter, as above, but in addition there is a pulse-width discriminator. The discriminator rejects the high-frequency output of filtered edges while passing the high-frequency output of a target or smaller feature. This technique is shown to reduce significantly the false alarms produced by a scene.
3. A high-pass filter, pulse-width discriminator, and cross-scan, multiple channel logic. Multiple-channel logic enhances the point-discrimination capability of the system by determining the cross-scan spatial extent of linear features and by rejecting those that are significantly greater in cross-scan extent than is expected of point targets. This feature was particularly useful in improving performance against certain terrain scenes that had significant linear feature content.

The results of the direct-processing methods are illustrated in images, graphs, and tables that compare performance of these techniques as well as the effects of spectral bands, scene types, and data spatial resolution. The analysis is concluded with a discussion of the implementation of the background processing in a missile guidance system.

REFERENCES

- ¹ Air Force Armament Laboratory, *Target and Background Information Library System (TABILS) User's Manual* (May 1, 1982).
- ² J. Beard, J. Braitwaite, and R. Turner, *Infrared Background Survey and Analysis*, ERIM 118000-1-F (Jun 1976).
- ³ A. J. LaRocca and D. J. Witte, *Handbook of the Statistics of Various Terrain and Water (1a) Backgrounds from Selected U.S. Locations*, ERIM 139900-1-X (Jan 1980).
- ⁴ R. L. Lucke, et al., "The Navy's Infrared Background Measurement and Analysis Program," in *Proc. IRIS Specialty Group Meeting on Targets, Background, and Discrimination*, San Diego (Feb 11-14, 1986).
- ⁵ R. A. Steinberg, "Navy IR Background Measurements and Analysis Program," in *Proc. Tri-Service Infrared Backgrounds Symp.*, Oct 18-20, 1983, Mitre Corporation, pp. 216-223.
- ⁶ A. Hirschman, "BMAP Surface-Based Background Measurement Activities at Montauk Point, New York, August 1983," Naval Surface Weapons Center, White Oak, Silver Spring, Md., draft report (Nov 1984).
- ⁷ General Dynamics/Pomona Division, *Background Spectral Radiance and Contrast in the Near-UV, Mid-IR, and LWIR Regions*, TM6-125PH-438 (Oct 1976).
- ⁸ General Dynamics/Pomona Division, *Available Target Infrared Spectral Signature Data*, TM6-125PH-450 (Sep 1981).
- ⁹ K. Peacock, *Radiometric Temperature Characteristics of the Ocean Surface*, JHU/APL STD-R-377 (Oct 1980).
- ¹⁰ A. J. LaRocca and B. A. Whaley, *DARPA Infrared Data Library*, ERIM 155300-24-X (Jul 1984).
- ¹¹ J. Shumsky and J. H. Schummers, AFGL-FLIR NKC-135 Aircraft Instrument, AFGL TR-82-0031 (Jan 26, 1982).
- ¹² R. A. Steinberg, *Elimination of Sensor Artifacts from Infrared Data*, NRL Report 8861 (Dec 11, 1984).
- ¹³ R. A. Steinberg and M. J. McHugh, *An Error Detection and Smoothing Algorithm for Infrared Data*, JHU/APL TG 1355 (Apr 1986).
- ¹⁴ A. N. Vavreck, *AFGL Infrared Image Restoration*, JHU/APL F1D(1)83-U-079.
- ¹⁵ A. N. Vavreck, *ERIM Infrared Image Restoration*, JHU/APL F1D(1)84-U-003.
- ¹⁶ H. Samuelson, "Infrared Systems: I. Expressions for Signal and Background Induced Noise with Space Filters," *IEEE Trans. Aerosp. Electron. Syst.* AES-7, 27-33 (1971).
- ¹⁷ R. Yoshitani, "Signal Processing Theory for Linearly Scanning Rectangular Detector," *Proc. IRIS* 18, 117-148 (1973).
- ¹⁸ J. Schroeder, J. H. Schummers, B. P. Sandford, and W. J. Tropf, "Infrared Cloud Backgrounds," in *Proc. Tri-Service Infrared Background Symposium*, AFGL-TR-84-0094 (Mar 16, 1984).
- ¹⁹ L. M. Howser and W. J. Tropf, "Investigation of Infrared Background Clutter," in *Research and Development Programs at The Johns Hopkins University Applied Physics Laboratory*, JHU/APL Quarterly Report RQR/85-1 (Jan-Mar 1985).
- ²⁰ W. J. Tropf, A. N. Vavreck, B. J. Sandford, J. H. Schummers, and J. Schroeder, "Infrared Cloud Backgrounds and Sensor Performance," in *Presentations at the Second Tri-Service Cloud Modeling Workshop*, IDA Report M-9, I, pp. 199-248 (Aug 1, 1984).
- ²¹ L. M. Howser, *Analysis of Background Measurement and Analysis Program (BMAP) IR Images*, JHU/APL F1F(2)85-U-035, Rev 1.
- ²² G. L. Turin, "An Introduction to Matched Filters," *IEEE Trans. Information Theory* IT 6, 311-329 (Jun 1960).
- ²³ L. M. Howser, "Investigation of Infrared Background Clutter," in *Research and Development Programs at The Johns Hopkins University Applied Physics Laboratory*, JHU/APL Quarterly Report RQR/85-2 (Apr-Jun 1985).

Appendix A

BMAP Data Description

Additional information on the Navy Backgrounds Measurement and Analysis Program (BMAP) data are contained in this appendix. Included is a list of the characteristics of the sensor, the long- and mid-wave spectral responses, and curves showing the long- and mid-wave point-source characteristics.

The objective of the BMAP program is to obtain clutter data for design of air- and surface-based IR search and track sensors. The data obtained by APL were the initial surface-based measurements obtained with a Raytheon-owned instrument. Currently, the described instrument is collecting data from a P-3 aircraft. An advanced instrument, with significantly more detector channels, smaller IFOV, and a more capable data acquisition system is being developed to support future measurements.

Primary characteristics of the BMAP sensor of interest to this study are the high-sensitivity, simultaneous dual-band capability, and the availability of oversampled data. Table A-1 gives the basic characteristics of the BMAP sensor. Figure A-1 gives the spectral response of the mid-IR and long-IR spectral bands. Figure A-2 gives the point-source response of typical mid-IR and far-IR detector channels.

Two data sets were available. The first measurement series was conducted at Montauk Point, Long Island, on August 9-19, 1983. These data are primarily over-cast sky and have less contrast than the later Bedford data. Fifty frames of data taken in the 8/8 (8 lines of mid-IR and the corresponding 8 lines of far-IR data) format on August 10, 1983 were provided. The second set of data was taken on September 13, 1984 at Bedford, Massachusetts. Seven scenes of a hole in a cloud deck were taken. Table A-2 summarizes the BMAP data.

Calibration constants to convert digital data counts to radiance are as follows:

Montauk Point

Long-IR $\sim 9.2 \times 10^{-7}$ W/cm²/sr per count
Mid-IR $\sim 1.8 \times 10^{-7}$ W/cm²/sr per count

Bedford

Long-IR 1.000×10^{-6} W/cm²/sr per count
Mid-IR 5.587×10^{-8} W/cm²/sr per count

Multiplying the recorded data by these factors recovers the measured radiance.

Table A-1 Characteristics of the BMAP dual-band IR measurement system.

Parameter	Value
Collecting area (3.9-4.8 μm) (7.6-11.3 μm)	80 cm^2
Optical transmission (3.9-4.8 μm) (7.6-11.3 μm)	85% 80%
Detector collecting efficiency (3.9-4.8 μm) (7.6-11.3 μm)	80%
Total optical efficiency (3.9-4.8 μm) (7.6-11.3 μm)	68% 64%
Detector area (3.9-4.8 μm)	$2.58 \times 10^{-5} \text{ cm}^2$
Detector D_{AV}^* (1 Hz - 1 kHz) (3.9-4.8 μm) (1 Hz - 1 kHz) (7.6-11.3 μm)	$2 \times 10^{11} \text{ cm Hz}^{1/2}/\text{W}$ $1.5 \times 10^{10} \text{ cm Hz}^{1/2}/\text{W}$
Electronic 3 dB bandwidth (3.9-4.8 μm) (7.6-11.3 μm)	0.0 Hz - 1 kHz 0.5 Hz - 1 kHz
Number of channels single color Two-color (per color)	16 ⁽¹⁾ 8
Total FOV ² elevation azimuth	5.33 mrad or 0.31° 2.8°
Instantaneous FOV	$0.33 \times 0.33 \text{ mrad}$
NEI (3.9-4.8 μm) (PV InSb) (7.6-11.3 μm) (PC HgCdTe)	$2.0 \times 10^{-14} \text{ W/cm}^2$ $1.0 \times 10^{-13} \text{ W/cm}^2$
Frame rate	2 forward scans/sec
Scanning speed during data acquisition	36°/sec
Detector element dwell time	520 μsec
Azimuth position resolution	0.096 mrad
Mirror shaft angle encoder	16 bits
Total incremental count (2.8° in azimuth)	512 samples
Dynamic range	12 bits/sample
Sample factor	3.44 samples/dwell
Internal reference cold hot	Narcissus, 77K precision, temp. controlled

¹Channel 1 of the 7.6-11.3 μm band is inactive.

²Internal reference source occupies $\sim 0.6^\circ$ of the azimuth FOV, leaving $\sim 2.2^\circ$.

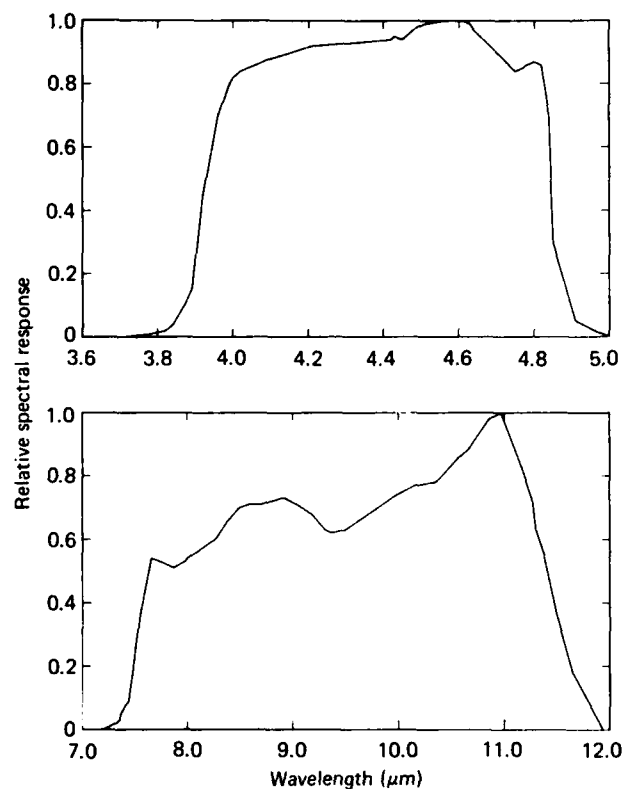


Figure A-1 Spectral response of BMAP mid- and long-wave channels.

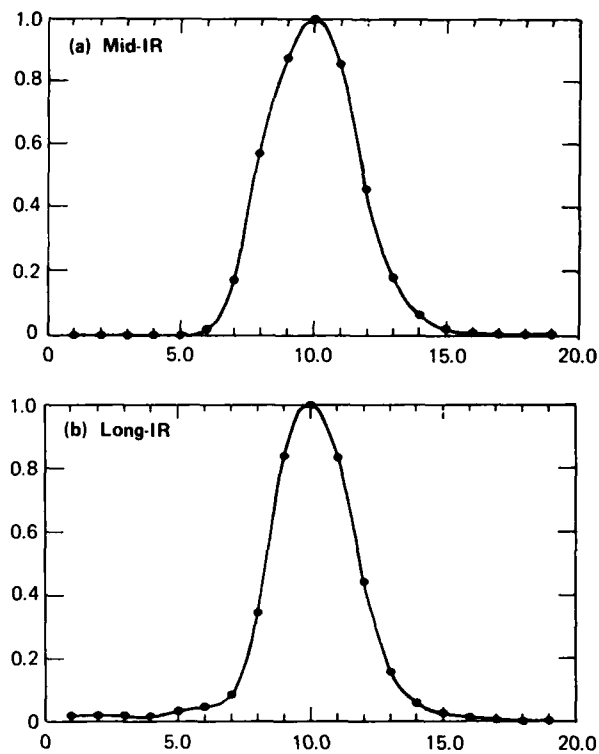


Figure A-2 Point-source response of BMAP detector channels.

Table A-2 Summary of BMAP data.

No.	Scene description	Line-of-sight ¹		Scan mode ²	IRIG local time ³	Frame (No.)	Temp. (°F)	RH (%)	Visibility (mi)	Wind		Sun ¹	
		Az	El							Speed	Dir	Az	El
Montauk Point, Aug 10, 1983													
1	Overcast sky	227	05	8/8		1-50	75	59		10,000 feet/sec	N	110	44
Bedford, Sep 13, 1984													
1	Hole in cloud deck	108	12	A	3,8,52, 21.3	1-61	66	48	>31	calm	—	112	28
2	Hole in cloud deck	112	15	A	3,8,55, 36.8	62-163	66	48	>31	calm	—	112	28
3	Hole in cloud deck	109	19	A	3,8,58, 39.8	164-265	66	48	>31	calm	—	113	29
4	Hole in cloud deck	130	11	A	3,9,07, 51.3	266-347	66	48	>31	calm	—	115	30
5	Hole in cloud deck	113	09	8/8	3,9,11, 47.8	348-389	66	48	>31	calm	—	116	31
6	Hole in cloud deck	93	08	A	3,9,18, 57.8	390-461	67	53	>31	calm	—	117	32
7	Hole in cloud deck	120	14	8/8	3,9,38, 38.8	521-551	67	53	>31	calm	—	121	35

¹Az = degrees clockwise from geographic north; El = degrees above horizontal.

²Scan mode: A = alternate mid-IR and long-IR frames; 8/8 = long-IR channels (5-12) in data channels (1-8) together with mid-IR channels (5-12) in data channels (9-16).

³IRIG time: Day, hour, minute, seconds.

Appendix B

AFGL Data Description

The information provided here is on the Air Force Geophysics Laboratory (AFGL) scenes. These scenes were collected from an IR FLIR Laboratory. The Honeywell IR FLIR is intended primarily for collecting signature data but has also been applied to collecting background data. The principal characteristics of these measurements are high spatial resolution, moderately large images, and a wide variety of available scenes. A description of the instrument is given in Table B-1.

Characteristics of AFGL data are given in Table B-2. All scenes contain clouds and are taken with filter #9 (7.84 to 13.16 μm). Table B-3 gives calibration data for all scenes. Note that scenes designated I21-I29 have a smaller FOV from typical AFGL FLIR data. This higher resolution is achieved by using an objective lens with longer focal length to increase spatial resolution. The system spectral response is given in Fig. B-1; overall response is approximately 80% of that achieved without a filter within the spectral bandpass.

Table B-1 Characteristics of the AFGL-FLIR.

Description	Value
Collecting aperture	25.2 cm ²
Effective focal length	7.67 cm
System $f/\#$	1.22
Detectors	Two 9-element, serially scanned PC HgCdTe arrays
Detector D* (11.5 μm , 10 kHz)	7.6×10^{10} cm Hz ^{1/2} /W
Noise-equivalent differential temperature	~0.2 K
Spectral bands	10-position filter wheel (APL data are all 7.84-13.16 μm)
Scanner	10-facet mirror (horizontal), galvanometer (vertical)
Dynamic range	100:1
Instantaneous FOV	0.43 mrad (V) \times 0.36 mrad (H)
Total FOV	4.93° (V) \times 7.62° (H)
Field rate	60 Hz
Active scan lines	192
Video output	EIA RS-170

Table B-2 Summary of AFGL infrared imagery characteristics.
(footnotes for this table follow Table B-3)

Image	Date	Time	Mission/ run	Scene description	Scene Size Pixels/ scan line, Number of scan lines	Flight Conditions			Pixel Size ⁽¹⁾			Notes	Image	
						Alt. ft x 1000	Vel. M#	Position Lat/Long	Look Dir.	Amb. Temp. (°C)	FLIR Resol. (H/V) (mrad)			Digitized sample size (mrad)
101	810518	164841.354	105/4	Clouds, down viewing	256, 192	33.1	0.68	39°24'/ 67°41'		-42	0.36/0.43	0.50/0.50		101
102	810518	175500.792	105/10	Clouds, water below	256, 192	39.3	0.66	39°24'/ 67°41'		-57	0.36/0.43	0.50/0.50		102
103	810821	182620.7	108/4	Overcast, down viewing	256, 192	31.1	0.76	42°17'/ 99°55'		-33	0.36/0.43	0.50/0.50		103
104	810821	182621.359	108/4	Terrain, down viewing	256, 192	31.1	0.76	42°17'/ 99°55'		-33	0.36/0.43	0.50/0.50		104
105	811111	164642.379	201/1	Horizon, clouds, terrain	256, 192	31.0	0.79	40°01'/ 81°48'		-41	0.36/0.43	0.50/0.50		105
106	811111	164926.145	201/1	Overcast cloud deck	256, 192	31.0	0.79	40°01'/ 81°48'		-41	0.36/0.43	0.50/0.50		106
107	811111	165045.409	201/1	Cloud structure	256, 192	31.0	0.79	40°01'/ 81°48'		-41	0.36/0.43	0.50/0.50		107
108	811111	200735.559	201/3	Cloud tops, horizon	256, 192	31.0	0.80	36°02'/110°01'		-38	0.36/0.43	0.50/0.50		108
109	811111	201713.679	201/3	Monument Valley, clouds	256, 192	31.0	0.80	36°02'/110°01'		-38	0.36/0.43	0.50/0.50		109
110	811111	201729.528	201/3	Monument Valley, clouds	256, 192	31.0	0.80	36°02'/110°01'		-38	0.36/0.43	0.50/0.50		110
111	820317	163706.484	209/1	Clouds	256, 192	33.2	0.80	43°42'/ 97°12'		-47	0.36/0.43	0.50/0.50		111
112	820317	164310.070	209/2	Clouds	256, 192	33.2	0.82	43°35'/ 96°25'		-48	0.36/0.43	0.50/0.50		112
113	821101	190200.296	301/3	Cloud tops, horizon	256, 192	35.0	0.80	36°33'/104°26'		-39	0.36/0.43	0.50/0.50		113
114	821101	190454.857	301/4	Cloud tops, horizon	256, 192	35.0	0.81	36°29'/104°49'		-40	0.36/0.43	0.50/0.50		114
115	821101	190623.029	301/4	Cloud tops, horizon	256, 192	35.0	0.81	36°29'/104°49'		-40	0.36/0.43	0.50/0.50	(4)	115
116	821120	182719.501	312/1	Horizon, clouds	256, 192	29.2	0.80	37°23'/104°29'		-34	0.36/0.43	0.50/0.50		116
117	821120	182911.381	312/1	Clouds, terrain background	256, 192	29.2	0.80	37°23'/104°29'		-34	0.36/0.43	0.50/0.50		117
118	821120	182938.926	312/1	Cloud tops, horizon	256, 192	29.2	0.80	37°23'/104°29'		-34	0.36/0.43	0.50/0.50		118
119	821120	182938.375	312/1	Cloud tops, horizon	256, 192	29.2	0.80	37°23'/104°29'		-34	0.36/0.43	0.50/0.50		119
120	821120	183915.495	312/1A	Clouds, down viewing	256, 192	29.2	0.80	37°23'/104°29'		-34	0.36/0.43	0.50/0.50		120
121	830327	182554.301	320/3	Structured clouds	256, 192	37.	0.76	42°13'/ 88°33'		-39	0.08/0.09	0.10/0.10		121
122	830327	182600.023	320/3	Structured clouds	256, 192	37.	0.76	42°13'/ 88°33'		-39	0.08/0.09	0.10/0.10		122
123	830327	182606.246	320/3	Structured clouds	256, 192	37.	0.76	42°13'/ 88°33'		-39	0.08/0.09	0.10/0.10		123
124	830327	182617.191	320/3	Structured clouds	256, 192	37.	0.76	42°13'/ 88°33'		-39	0.08/0.09	0.10/0.10		124
125	830327	182625.132	320/3	Structured clouds	256, 192	37.	0.76	42°13'/ 88°33'		-39	0.08/0.09	0.10/0.10		125
126	830327	182629.420	320/3	Structured clouds	256, 192	37.	0.76	42°13'/ 88°33'		-39	0.08/0.09	0.10/0.10		126
127	830327	182637.762	320/3	Structured clouds	256, 192	37.	0.76	42°13'/ 88°33'		-39	0.08/0.09	0.10/0.10		127
128	830327	182650.775	320/3	Structured clouds	256, 192	37.	0.76	42°13'/ 88°33'		-39	0.08/0.09	0.10/0.10		128
129	830327	182917.624	320/3	Structured clouds	256, 192	37.	0.76	42°13'/ 88°33'		-39	0.08/0.09	0.10/0.10		129
130	830723	174721.655	325/3	Clouds below horizon	256, 192	29.1	0.76	38°26'/ 81°50'		-25	0.36/0.43	0.50/0.50		130
131	830723	175010.243	325/3	Clouds, down viewing	256, 192	29.1	0.76	38°26'/ 81°50'		-25	0.36/0.43	0.50/0.50		131

Table B-3 Calibration and spectral band data for AFGL infrared imagery.
(footnotes for this table and Table B-2 follow)

Image	Filter	Spectral Band ⁽³⁾ (μm)	Conversion Factors ⁽²⁾ to Radiance ($\mu\text{W}/\text{cm}^2/\text{sr}$)		Image
			Multiplicative	Additive	
I01	I9005A	7.84-13.16	$8.4088 \cdot 10^{-6}$	$1.8064 \cdot 10^{-3}$	I01
I02	I9005A	7.84-13.16	$5.3056 \cdot 10^{-6}$	$2.9287 \cdot 10^{-3}$	I02
I03	I9005A	7.84-13.16	$2.1122 \cdot 10^{-5}$	$1.4909 \cdot 10^{-3}$	I03
I04	I9005A	7.84-13.16	$2.1122 \cdot 10^{-5}$	$1.4909 \cdot 10^{-3}$	I04
I05	I9005A	7.84-13.16	$8.4088 \cdot 10^{-6}$	$1.9456 \cdot 10^{-3}$	I05
I06	I9005A	7.84-13.16	$1.3327 \cdot 10^{-5}$	$1.4152 \cdot 10^{-3}$	I06
I07	I9005A	7.84-13.16	$1.3327 \cdot 10^{-5}$	$1.4126 \cdot 10^{-3}$	I07
I08	I9005A	7.84-13.16	$3.3476 \cdot 10^{-5}$	$-2.4370 \cdot 10^{-3}$	I08
I09	I9005A	7.84-13.16	$1.0586 \cdot 10^{-5}$	$2.0466 \cdot 10^{-3}$	I09
I10	I9005A	7.84-13.16	$1.0586 \cdot 10^{-5}$	$2.5241 \cdot 10^{-3}$	I10
I11	I9005A	7.84-13.16	$8.4088 \cdot 10^{-6}$	$1.0573 \cdot 10^{-3}$	I11
I12	I9005A	7.84-13.16	$8.4088 \cdot 10^{-6}$	$1.3923 \cdot 10^{-3}$	I12
I13	I9005A	7.84-13.16	$1.6778 \cdot 10^{-5}$	$2.9420 \cdot 10^{-4}$	I13
I14	I9005A	7.84-13.16	$1.6778 \cdot 10^{-5}$	$4.1807 \cdot 10^{-4}$	I14
I15	B2180A	7.96-11.39	⁽⁴⁾	⁽⁴⁾	I15
I16	I9005A	7.84-13.16	$1.6778 \cdot 10^{-5}$	$-1.3316 \cdot 10^{-5}$	I16
I17	I9005A	7.84-13.16	$1.6778 \cdot 10^{-5}$	$5.6492 \cdot 10^{-4}$	I17
I18	I9005A	7.84-13.16	$1.6778 \cdot 10^{-5}$	$9.6727 \cdot 10^{-4}$	I18
I19	I9005A	7.84-13.16	$1.6778 \cdot 10^{-5}$	$9.6727 \cdot 10^{-4}$	I19
I20	I9005A	7.84-13.16	$8.4088 \cdot 10^{-6}$	$1.4649 \cdot 10^{-3}$	I20
I21	I9005A	7.84-13.16	$6.6793 \cdot 10^{-6}$	$3.2448 \cdot 10^{-3}$	I21
I22	I9005A	7.84-13.16	$6.6793 \cdot 10^{-6}$	$3.2414 \cdot 10^{-3}$	I22
I23	I9005A	7.84-13.16	$6.6793 \cdot 10^{-6}$	$3.2414 \cdot 10^{-3}$	I23
I24	I9005A	7.84-13.16	$8.4088 \cdot 10^{-6}$	$2.9607 \cdot 10^{-3}$	I24
I25	I9005A	7.84-13.16	$8.4088 \cdot 10^{-6}$	$2.8066 \cdot 10^{-3}$	I25
I26	I9005A	7.84-13.16	$8.4088 \cdot 10^{-6}$	$3.2804 \cdot 10^{-3}$	I26
I27	I9005A	7.84-13.16	$8.4088 \cdot 10^{-6}$	$3.2804 \cdot 10^{-3}$	I27
I28	I9005A	7.84-13.16	$8.4088 \cdot 10^{-6}$	$2.9684 \cdot 10^{-3}$	I28
I29	I9005A	7.84-13.16	$8.4088 \cdot 10^{-6}$	$3.1648 \cdot 10^{-3}$	I29
I30	I9005A	7.84-13.16	$1.0586 \cdot 10^{-5}$	$-1.1037 \cdot 10^{-3}$	I30
I31	I9005A	7.84-13.16	$1.0586 \cdot 10^{-5}$	$-6.1401 \cdot 10^{-4}$	I31

Footnotes for AFGL background data description, Tables B2 and B3

¹ FLIR angular resolution and digitized sample size are given as value in the horizontal (scan) direction followed by value in vertical direction. The images are formed by combining the (delayed) outputs of two serially scanning detector arrays.

² The digital values (0-255) describing the brightness of each pixel are converted to actual scene radiance ($\mu\text{W}/\text{cm}^2/\text{sr}/\mu\text{m}$) by multiplying the digital value (DV) of the data by the multiplicative factor (MF) and adding the additive factor (AF):

$$\text{Brightness} = \text{MF} \times \text{DV} + \text{AF}.$$

The scene has a maximum of 64 gray levels at multiples of 4 (i.e., 0, 4, 8, ..., 248, 252). Therefore the quantization level is $4 \times \text{MF}$.

³ The spectral band is described by the 50% spectral response points. The AFGL FLIR has a 10-position filter wheel. Reference 11 gives spectral response data for all the filters.

⁴ Calibration data supplied for image I15 are not correct.

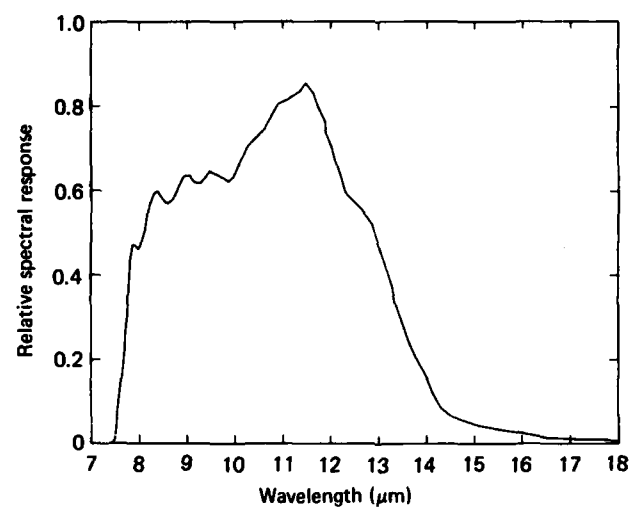


Figure B-1 Spectral response of AFGL FLIR with 7.84-13.16 μm filter.

Appendix C

ERIM Data Description

Information on the Environmental Research Institute of Michigan (ERIM) scenes is provided in this appendix.

Data provided by ERIM consist of surface scenes collected by the M-7 multispectral line scanner or its similar predecessor the M-5. A typical collection run is made at low altitude from a C-47 aircraft. The scanner looks downward (or tilted forward) and is scanned (with a mirror) in the cross-track direction over a 90° sector. Down-track data are gathered as the aircraft flies over the scene. The principal benefit of the ERIM data is the large number of available spectral bands per scene and the large size of some scenes (>1,000,000 pixels).

Table C-1 gives the characteristics of the M-7 scanner. Table C-2 summarizes the scene data provided to APL. Calibration constants to convert digital counts to radiance or apparent temperature (depending on spectral band) are provided in Table C-3. Spectral characteristics of the major detector channels are given in Fig. C-1. There are two infrared detector positions in the M-7 scanner. One is devoted to the long wavelength band and the other to the mid-IR detectors. Several mid-IR detector arrays were used to collect the data. Table C-4 gives the relative geometry of the four detector arrays used to collect these data and data shifts required to bring pixels of different spectral channels into approximate alignment in the center of a scan line. Note that geometric effects will not allow registration across an entire (single) scan line.

Table C-1 Characteristics of the ERIM M-7 scanner.

Parameter	Value
Collecting aperture	5-inch
Spatial resolution	2 mrad
Scan rate	60/sec
NEAT	0.1°C nominal
Spectral bands (μm)	1.0-1.4 2.0-2.6 3.0-4.2 3.5-3.9 3.9-4.7 4.5-5.5 5.1-5.7 8.0-13.5 8.0-14.0 9.0-11.4

Table C-2 Summary of ERIM infrared imagery characteristics.
(footnotes for this table follow Table C-3)

Image	Date	Time	Scene Description	Spectral Bands (μm)								Scene Size Pixels/ scan line, Number of scan lines	Flight Conditions		Pixel Size ⁽¹⁾		Notes	Image		
				1.0-1.4	2.0-2.6	3.0-4.2	3.5-3.9	3.9-4.7	4.5-5.5	5.1-5.7 ⁽⁵⁾	8.0-13.5		9.0-11.4	Alt. (ft)	Vel. ft/s	Dir.			Dep. Ang.	Scanner resol. (mrad)
S01	780323	0930	Camp AP Hill, morning, clear, v = 30km	1					2			3	855, 700	800	168	West	90°	2.0/2.0	1.60/1.60	S01
S02	780323	1330	Camp AP Hill, afternoon, clear	1					2			3	855, 704	800	168	West	90°	2.0/2.0	1.60/1.60	S02
S03	780323	1830	Camp AP Hill, evening, light haze	1					2			3	855, 700	800	168	West	90°	2.0/2.0	1.60/1.60	S03
S04	780323	2300	Camp AP Hill, midnight, clear	1					2			3	855, 1000	800	168	West	90°	2.0/2.0	1.60/1.60	S04
S05	790403	0600	N.M.I. city, predawn, snow, cloudy									2	646, 385	1750	202	NNW	90°	2.5/2.5	4.38/4.38	S05
S06	790403	1230	N.M.I. city, noon, snow, clear						2	3		4	646, 385	1750	202	NNW	90°	2.5/2.5	4.38/4.38	S06
S07	790403	1900	N.M.I. city, sunset, snow, 15% clouds						1	2		3	646, 385	1750	202	NNW	90°	2.5/2.5	4.38/4.38	S07
S08	790403	0030	N.M.I. city, midnight, snow, 60-70% clouds						1	2		2.3	646, 385	1750	202	NNW	90°	2.5/2.5	4.38/4.38	S08
S09	790403	0600	N.M.I. conifers, predawn, snow, -2°C						1	2		2	646, 385	1750	202	NNW	90°	2.5/2.5	4.38/4.38	S09
S10	790403	1230	N.M.I. conifers, noon, snow, 5°C						1	2		3	646, 385	1750	202	NNW	90°	2.5/2.5	4.38/4.38	S10
S11	790403	0030	N.M.I. conifers, sunset, snow, 4°C						1	2		2.3	646, 385	1750	202	NNW	90°	2.5/2.5	4.38/4.38	S11
S12	790403	0600	N.M.I. conifers, midnight, snow -2°C						1	2		2	646, 385	1750	202	NNW	90°	2.5/2.5	4.38/4.38	S12
S13	790403	1230	N.M.I. farms, predawn, snow, cloudy						1	2		3	646, 385	1750	202	NNW	90°	2.5/2.5	4.38/4.38	S13
S14	790403	1900	N.M.I. farms, noon, snow, clear						1	2		3	646, 385	1750	202	NNW	90°	2.5/2.5	4.38/4.38	S14
S15	790403	0030	N.M.I. farms, sunset, snow, 15% clouds						1	2		3	646, 385	1750	202	NNW	90°	2.5/2.5	4.38/4.38	S15
S16	790403	0600	N.M.I. farms, midnight, snow, 60-95% clouds						1	2		2.3	646, 385	1750	202	NNW	90°	2.5/2.5	4.38/4.38	S16
S17	790403	1230	N.M.I. land/water, predawn, snow, -2°C						1	2		2	646, 385	1750	202	NNW	90°	2.5/2.5	4.38/4.38	S17
S18	790403	1900	N.M.I. land/water, noon, snow, 5°C						1	2		3	646, 385	1750	202	NNW	90°	2.5/2.5	4.38/4.38	S18
S19	790403	0030	N.M.I. land/water, sunset, snow, 4°C						1	2		3	646, 385	1750	202	NNW	90°	2.5/2.5	4.38/4.38	S19
S20	790403	0600	N.M.I. land/water, midnight, snow, -2°C						1	2		2.3	646, 385	1750	202	NNW	90°	2.5/2.5	4.38/4.38	S20
S21	690722	1340	Black Hills-I (M-5 scanner)	1	2				3			4	311, 732	1500	200	East	90°	3.5/6.6	3.75/9.90	S21
S22	680923	0952	Mono Lake (M-5 scanner)	(8)	(8)				1			(8)	311, 265	4000	200	South	90°	3.5/6.6	10.00/26.40	S22
S23	780307	1215	Port Hueneme (HUM1), port/water	1	2				3			4	646, 1982	1750	202	West	90°	2.5/2.5	4.38/4.38	S23
S24	780307	1420	Port Hueneme (HUM2), port/water/sun	1	2				3			4	646, 1761	1000	202	West	35°	2.5/2.5	4.36/7.60	S24
S25	780225	0926	Nellis AFB (NVG1), mountains	1	2				3			4	646, 1535	1750	202	West	90°	2.5/2.5	4.38/4.38	S25
S26	780225	1051	Nellis AFB (NVH1), desert	1	2				3			4	646, 882	1000	202	East	35°	2.5/2.5	4.36/7.60	S26
S27	780225	1528	Nellis AFB (NEVJ), mountains	3	2	1							646, 883	1000	202	South	35°	2.5/2.5	4.36/7.60	S27
S28	780225	1548	Nellis AFB (NEVK), mountains	3	2	1							646, 883	1000	202	North	35°	2.5/2.5	4.36/7.60	S28
S29	780225	1554	Nellis AFB (NEVL), desert	3	2	1				3			646, 883	1000	202	East	35°	2.5/2.5	4.36/7.60	S29
S30	780226	1022	Nellis AFB (NEVM), mountains	3	2	1							646, 883	1000	202	East	35°	2.5/2.5	4.36/7.60	S30
F03	780307	1130	Pt Mugu (NEVA1), water/sun	1	(8)				2	3			646, 271	2000	202	SW-SE	90°	2.5/2.5	5.00/5.00	F03
F04	780307	1156	Pt Mugu (NEVA4), water, sun						2	1		3	646, 215	2000	202	SW-SE	90°	2.5/2.5	5.00/5.00	F04
F05	780225	1511	Nellis AFB (NEVB), mountains						2	1		3	646, 899	1000	202	East	35°	2.5/2.5	4.36/7.60	F05
F06	780225	1424	Nellis AFB (NEVE), mountains						2	1		3	646, 179	5000	202	East	35°	2.5/2.5	21.79/38.00	F06
F07	780225	1056	Nellis AFB (NEVC), desert						2	1		3	646, 898	1000	202	West	35°	2.5/2.5	4.36/7.60	F07
F08	780225	0914	Nellis AFB (NEVD), mountains						2	1		3	646, 1541	1750	202	West	90°	2.5/2.5	4.38/4.38	F08
F09	780225	1034	Nellis AFB (NEVF), mountains						2	1		3	646, 899	1000	202	East	35°	2.5/2.5	4.36/7.60	F09

Table C-3 Calibration and spatial registration for ERIM infrared imagery.
(footnotes for this table and Table C-2 follow)

Image	Spectral Channel Scaling Constants ⁽¹⁾										Spectral Bands (μm)				Spatial Registration ⁽²⁾								
	Channel 1		Channel 2		Channel 3		Channel 4		conversion factors		conversion factors		conversion factors		conversion factors		Spectral band						
	conversion factors		conversion factors		conversion factors		conversion factors		conversion factors		conversion factors		conversion factors		conversion factors		Spectral band						
	Multipl.	Additive	Unit	Multipl.	Additive	Unit	Multipl.	Additive	Unit	Multipl.	Additive	Unit	Multipl.	Additive	Unit	Multipl.	Additive	Unit	1	2	3	4	
S01	1.48649	- 65.405	rad	0.109412	272.368	K	0.153566	266.193	K	0.153566	266.193	K	0.153566	266.193	K	1	2	3	4	1	2	3	4
S02	1.12245	- 35.9184	rad	0.125966	269.518	K	0.187140	270.335	K	0.187140	270.335	K	0.187140	270.335	K	1	2	3	4	1	2	3	4
S03	0.88000	- 26.4000	rad	0.0465351	277.899	K	0.0724006	273.729	K	0.0724006	273.729	K	0.0724006	273.729	K	1	2	3	4	1	2	3	4
S04	0.758621	- 48.5517	rad	0.0895737	270.923	K	0.0946701	270.911	K	0.0946701	270.911	K	0.0946701	270.911	K	1	2	3	4	1	2	3	4
S05	0.0216759	273.283	K	0.0161324	273.498	K	0.0432885	273.730	K	0.0432885	273.730	K	0.0432885	273.730	K	1	2	3	4	1	2	3	4
S06	7.23158	- 435.394	rad	0.420110	206.309	K	0.0164292	273.567	K	0.0164292	273.567	K	0.0164292	273.567	K	1	2	3	4	1	2	3	4
S07	0.115987	254.821	K	0.0215169	273.222	K	0.0163306	273.144	K	0.0163306	273.144	K	0.0163306	273.144	K	1	2	3	4	1	2	3	4
S08	0.0214671	273.277	K	0.0485744	269.979	K	0.0677925	272.808	K	0.0677925	272.808	K	0.0677925	272.808	K	1	2	3	4	1	2	3	4
S09	0.0208554	273.815	K	0.0162540	273.779	K	0.0437711	273.310	K	0.0437711	273.310	K	0.0437711	273.310	K	1	2	3	4	1	2	3	4
S10	7.25525	- 532.456	rad	0.424625	204.173	K	0.0164120	273.519	K	0.0164120	273.519	K	0.0164120	273.519	K	1	2	3	4	1	2	3	4
S11	0.118226	254.210	K	0.0215993	273.150	K	0.0164120	273.519	K	0.0164120	273.519	K	0.0164120	273.519	K	1	2	3	4	1	2	3	4
S12	0.0215332	273.216	K	0.0488683	269.839	K	0.0162578	273.333	K	0.0162578	273.333	K	0.0162578	273.333	K	1	2	3	4	1	2	3	4
S13	0.0216452	273.175	K	0.0162578	273.333	K	0.0441579	272.913	K	0.0441579	272.913	K	0.0441579	272.913	K	1	2	3	4	1	2	3	4
S14	7.24848	- 586.506	rad	0.462976	194.149	K	0.0165250	272.875	K	0.0165250	272.875	K	0.0165250	272.875	K	1	2	3	4	1	2	3	4
S15	0.120342	253.514	K	0.0222503	271.750	K	0.0165250	272.875	K	0.0165250	272.875	K	0.0165250	272.875	K	1	2	3	4	1	2	3	4
S16	0.0215734	273.139	K	0.0491603	269.634	K	0.0164407	273.644	K	0.0164407	273.644	K	0.0164407	273.644	K	1	2	3	4	1	2	3	4
S17	0.0209377	273.666	K	0.0164407	273.644	K	0.0438113	273.153	K	0.0438113	273.153	K	0.0438113	273.153	K	1	2	3	4	1	2	3	4
S18	7.23321	- 493.026	rad	0.459405	195.496	K	0.0215725	273.117	K	0.0215725	273.117	K	0.0215725	273.117	K	1	2	3	4	1	2	3	4
S19	0.119521	253.896	K	0.0215725	273.117	K	0.0164225	273.053	K	0.0164225	273.053	K	0.0164225	273.053	K	1	2	3	4	1	2	3	4
S20	0.0215725	273.226	K	0.0488549	269.852	K	0.0816904	288.905	K	0.0816904	288.905	K	0.0816904	288.905	K	1	2	3	4	1	2	3	4
S21	27.9646	- 27.9646	rad	1.58301	- 3.16601	rad	0.0816904	288.905	K	0.0816904	288.905	K	0.0816904	288.905	K	1	2	3	4	1	2	3	4
S22	0.111804	276.747	K													(b)	(b)	(b)	(b)				
S23	2.22000	- 126.550	rad	- 0.0901961	300.000	K	0.141262	282.061	K	0.141262	282.061	K	0.141262	282.061	K	1	2	3	4	1	2	3	4
S24	1.73522	- 113.347	rad	0.696934	169.417	K	0.157527	277.397	K	0.157527	277.397	K	0.157527	277.397	K	1	2	3	4	1	2	3	4
S25	1.06352	- 28.9010	rad	0.491094	199.472	K	0.0998831	270.780	K	0.0998831	270.780	K	0.0998831	270.780	K	1	2	3	4	1	2	3	4
S26	2.89031	- 26.8297	rad	0.526944	209.378	K	0.137019	276.542	K	0.137019	276.542	K	0.137019	276.542	K	1	2	3	4	1	2	3	4
S27	0.124586	269.122	K	0.521030	191.812	K	1.00000	- 56.7006	rad	1.00000	- 56.7006	rad	1.00000	- 56.7006	rad	1	2	3	4	1	2	3	4
S28	0.102839	269.941	K	0.495677	190.411	K	1.00000	- 56.8537	rad	1.00000	- 56.8537	rad	1.00000	- 56.8537	rad	1	2	3	4	1	2	3	4
S29	0.0878207	276.758	K	0.436174	208.743	K	- 0.090196	300.000	K	- 0.090196	300.000	K	- 0.090196	300.000	K	1	2	3	4	1	2	3	4
S30	0.0504308	275.229	K	0.492889	195.697	K	1.00000	- 129.555	rad	1.00000	- 129.555	rad	1.00000	- 129.555	rad	1	2	3	4	1	2	3	4
F03	3.0932	- 14.9566	rad	0.0316129	283.956	K	0.255415	261.200	K	0.255415	261.200	K	0.255415	261.200	K	1	2	3	4	1	2	3	4
F04	0.178320	277.694	K	0.626448	226.579	K	0.0704379	284.457	K	0.0704379	284.457	K	0.0704379	284.457	K	1	2	3	4	1	2	3	4
F05	0.085632	277.476	K	0.484893	201.702	K	0.517669	199.105	K	0.517669	199.105	K	0.517669	199.105	K	1	2	3	4	1	2	3	4
F06	0.127561	268.445	K	0.644889	173.319	K	0.537182	193.200	K	0.537182	193.200	K	0.537182	193.200	K	1	2	3	4	1	2	3	4
F07	0.155668	276.012	K	0.504799	224.004	K	0.14172	279.92	K	0.14172	279.92	K	0.14172	279.92	K	1	2	3	4	1	2	3	4
F08	0.0966366	267.812	K	0.469730	193.632	K	0.127765	269.867	K	0.127765	269.867	K	0.127765	269.867	K	1	2	3	4	1	2	3	4
F09	0.111736	270.111	K	0.538573	193.809	K	0.139151	273.470	K	0.139151	273.470	K	0.139151	273.470	K	1	2	3	4	1	2	3	4

Footnotes for ERIM background data description, Tables C-2 and C-3

¹ Angular resolution and ground sample distance given as value in scan (cross-track) direction followed by value in flight (in-track) direction. Resolutions given are for middle-infrared bands; specifically the resolution of long-wavelength bands that differ from values in the table are:

File	Channel	Spectral band	Resolution
S21	4	8.0-13.5	3.5 mrad
S23-S26	4	9.0-11.4	2.9 mrad
S29, F03, F05-F06	3	5.1-5.7	2.9 mrad
F04, F07-F09	3	9.0-11.4	2.9 mrad

² The digital values (0-255) describing the brightness of each pixel is converted to actual scene radiance ($\mu\text{W}/\text{cm}^2/\text{sr}/\mu\text{m}$) or apparent temperature (K) by multiplying the digital value (DV) by the multiplicative factor (MF) and adding the additive factor (AF):

$$\text{Brightness} = \text{MF} \times \text{DV} + \text{AF}.$$

The units of the brightness result are given in the units column. MF is the data quantization increment.

³ Spatial registration is given as the relative pixel number in a scan line that brings the images of different channels into approximate spatial alignment. Alignment is a function of the scan angle; best alignment is achieved in the center of scan. See Table 3, Fig. 4, and Ref. 10 for more information.

⁴ Channel 3 data are preferred to channel 2 data for the 9.0-11.4 μm spectral band.

⁵ Data for the 5.1-5.7 μm channel are noisy and may not be usable.

⁶ Data file contains discontinuous images:

F03 and F04 contain small segments (approximately 15 scan lines per segment) of a much larger image.

F07 has two subimages of 449 scan lines each.

⁷ Tilted scanner images have vignetting on the edges of the image. Only center 400 pixels are completely free of vignetting effects.

⁸ Original channel 2 (3.0-4.3 μm) of image F03 has been dropped (bad data); other channels were renumbered. Data available for 1.0-1.4, 2.0-2.6, and 8.0-13.5 μm channels were not provided to APL.

⁹ Long-wavelength channels of M-5 scanner cannot be easily brought into spatial alignment with other channels.

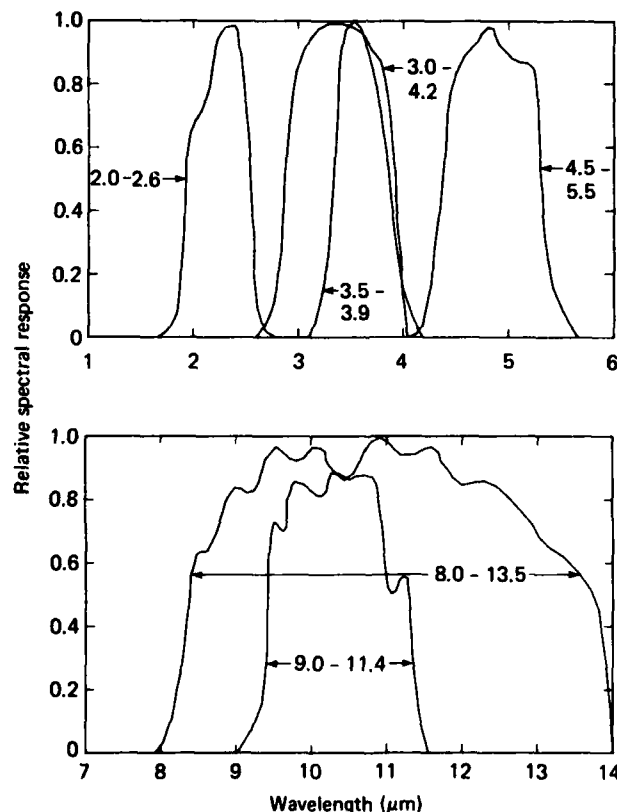


Figure C-1 Spectral characteristics of ERIM M-7 detector channels.

Table C-4 ERIM middle-infrared detector arrays.

Array ⁽¹⁾	Spectral Bands ⁽²⁾			Images
	Detector 1	Detector 2	Detector 3	
InSb 3-3	2.0-2.6 μm	1.0-1.4 μm	4.5-5.5 μm	S21-S22
InSb 3-7	3.9-4.7 μm	2.0-2.6 μm ⁽³⁾	3.5-3.9 μm	S27-S30, F04-F09
InSb 3-8	3.0-4.2 μm	2.0-2.6 μm	4.5-5.5 μm	S01-S04, S23-S26, F03
InSb 3-9	3.5-3.9 μm	2.0-2.6 μm	4.5-5.5 μm	S05-S20

¹Detectors are circular with center-to-center spacing of 2.5 times the detector diameter.

²5.1-5.7 μm and long-wavelength detectors are at a different focal plane of the M-7 scanner and are in spatial registration with the center detector of the above arrays.

³Detector inoperative.

Illustration of detector shifting to achieve spatial coincidence

Detector footprints at successive samples		Pixels in spatial registration at the indicated point	
Time ↓	<div style="display: flex; justify-content: space-around; align-items: center;"> <div style="text-align: center;"> <div style="border: 1px solid black; padding: 2px;">3</div> <div style="border: 1px solid black; padding: 2px;">2</div> <div style="border: 1px solid black; padding: 2px;">1</div> </div> <div style="margin-left: 20px;"> <div style="border: 1px solid black; padding: 2px;">3</div> <div style="border: 1px solid black; padding: 2px;">2</div> <div style="border: 1px solid black; padding: 2px;">1</div> </div> <div style="margin-left: 20px;"> <div style="border: 1px solid black; padding: 2px;">3</div> <div style="border: 1px solid black; padding: 2px;">2</div> <div style="border: 1px solid black; padding: 2px;">1</div> </div> </div>	Detector 1	(pixel i - 2)
			(pixel i - 1)
	<div style="display: flex; justify-content: space-around; align-items: center;"> <div style="text-align: center;"> <div style="border: 1px solid black; padding: 2px;">3</div> <div style="border: 1px solid black; padding: 2px;">2</div> <div style="border: 1px solid black; padding: 2px;">1</div> </div> <div style="margin-left: 20px;"> <div style="border: 1px solid black; padding: 2px;">3</div> <div style="border: 1px solid black; padding: 2px;">2</div> <div style="border: 1px solid black; padding: 2px;">1</div> </div> <div style="margin-left: 20px;"> <div style="border: 1px solid black; padding: 2px;">3</div> <div style="border: 1px solid black; padding: 2px;">2</div> <div style="border: 1px solid black; padding: 2px;">1</div> </div> </div>	Detector 2	(pixel i)
			(pixel i + 1)
	<div style="display: flex; justify-content: space-around; align-items: center;"> <div style="text-align: center;"> <div style="border: 1px solid black; padding: 2px;">3</div> <div style="border: 1px solid black; padding: 2px;">2</div> <div style="border: 1px solid black; padding: 2px;">1</div> </div> <div style="margin-left: 20px;"> <div style="border: 1px solid black; padding: 2px;">3</div> <div style="border: 1px solid black; padding: 2px;">2</div> <div style="border: 1px solid black; padding: 2px;">1</div> </div> <div style="margin-left: 20px;"> <div style="border: 1px solid black; padding: 2px;">3</div> <div style="border: 1px solid black; padding: 2px;">2</div> <div style="border: 1px solid black; padding: 2px;">1</div> </div> </div>	Detector 3	(pixel i + 2)

Appendix D

Power Spectral Density of Background Data

PSDs of many of the scenes used in this analysis are shown in this appendix. It is evident that the AFGL scenes flatten far before the cutoff of the system. This flattening shows the level of the internal noise of the

sensor. Some of the ERIM scenes show this flattening to a degree, while other scenes continue straight with no flattening trend.

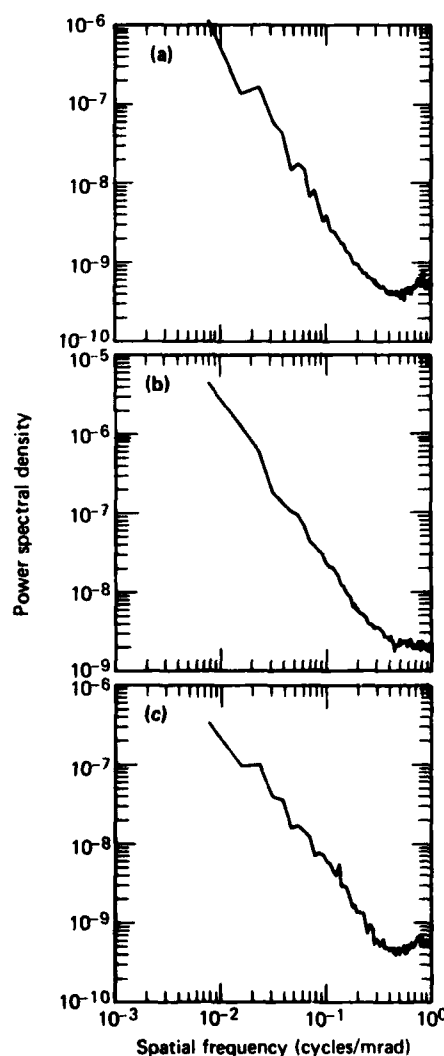


Figure D-1 Power spectral densities of AFGL scenes, 7.84-13.16 μm spectral band (0.5 mrad sample size). (a) Clouds, down viewing (I01). (b) Terrain, down viewing (I04). (c) Monument Valley, clouds (I09).

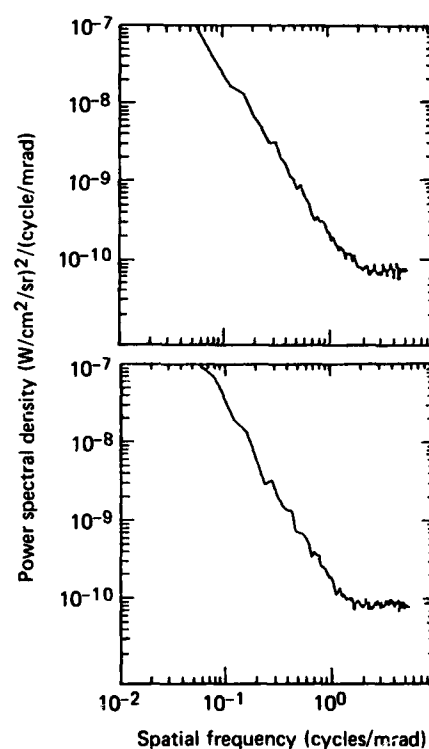


Figure D-2 Power spectral densities of AFGL scenes, 7.84-13.16 μm spectral band (0.1 mrad sample size).

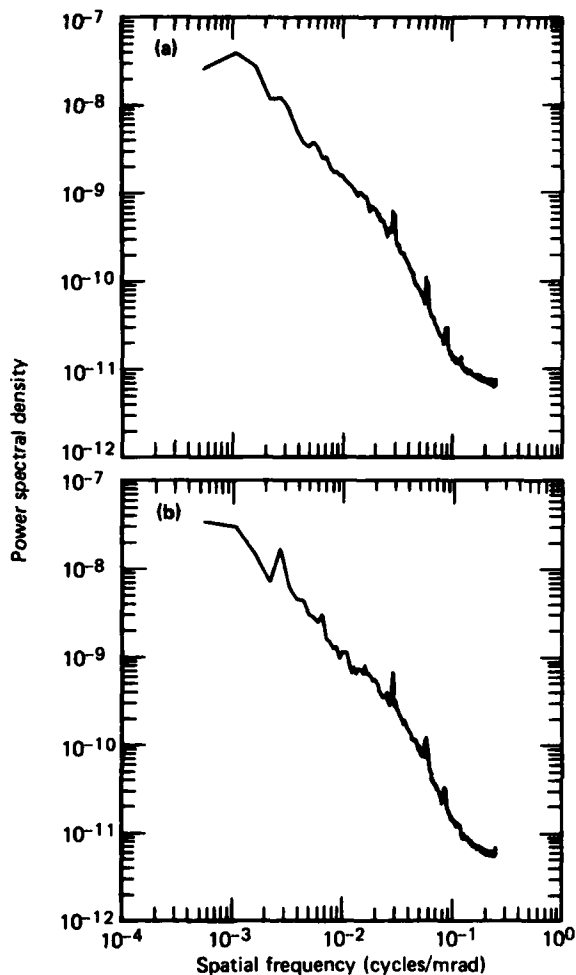


Figure D-3 Power spectral densities of ERIM scenes of Camp A.P. Hill, 2.0-2.6 μm spectral band. (a) Morning (S01CH1). (b) Afternoon (S02CH1).

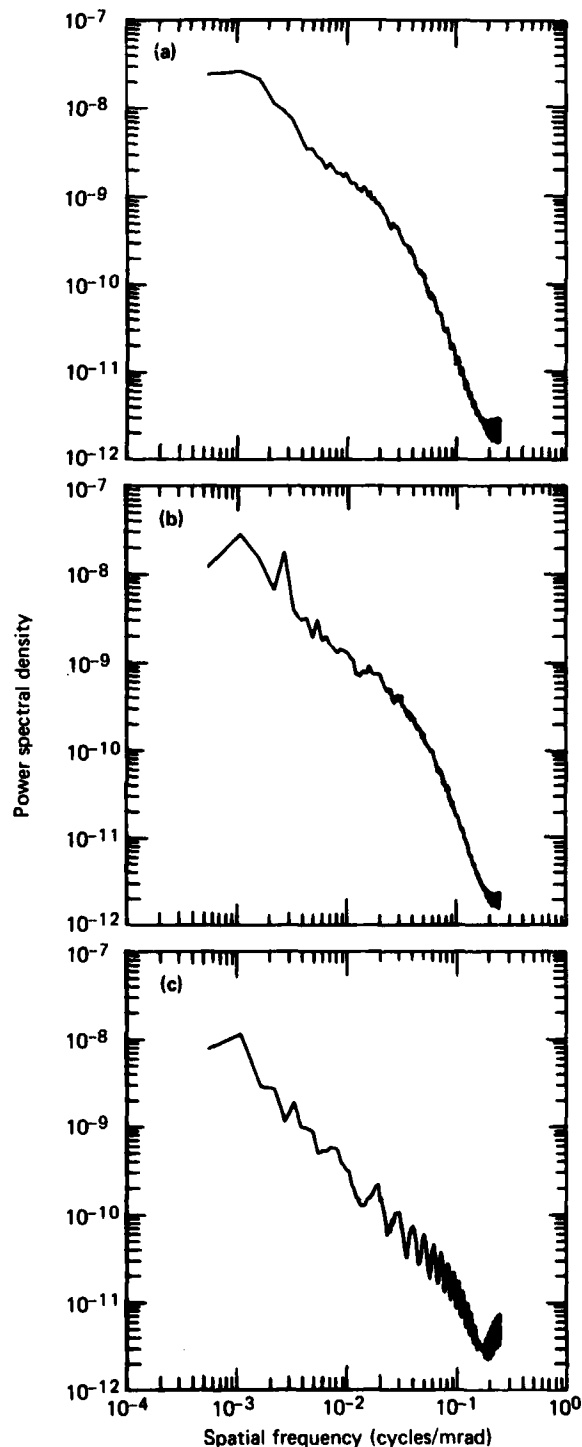


Figure D-4 Power spectral densities of ERIM scenes of Camp A.P. Hill, 4.5-5.5 μm spectral band. (a) Morning (S01CH2). (b) Afternoon (S02CH2). (c) Evening (S03CH2).

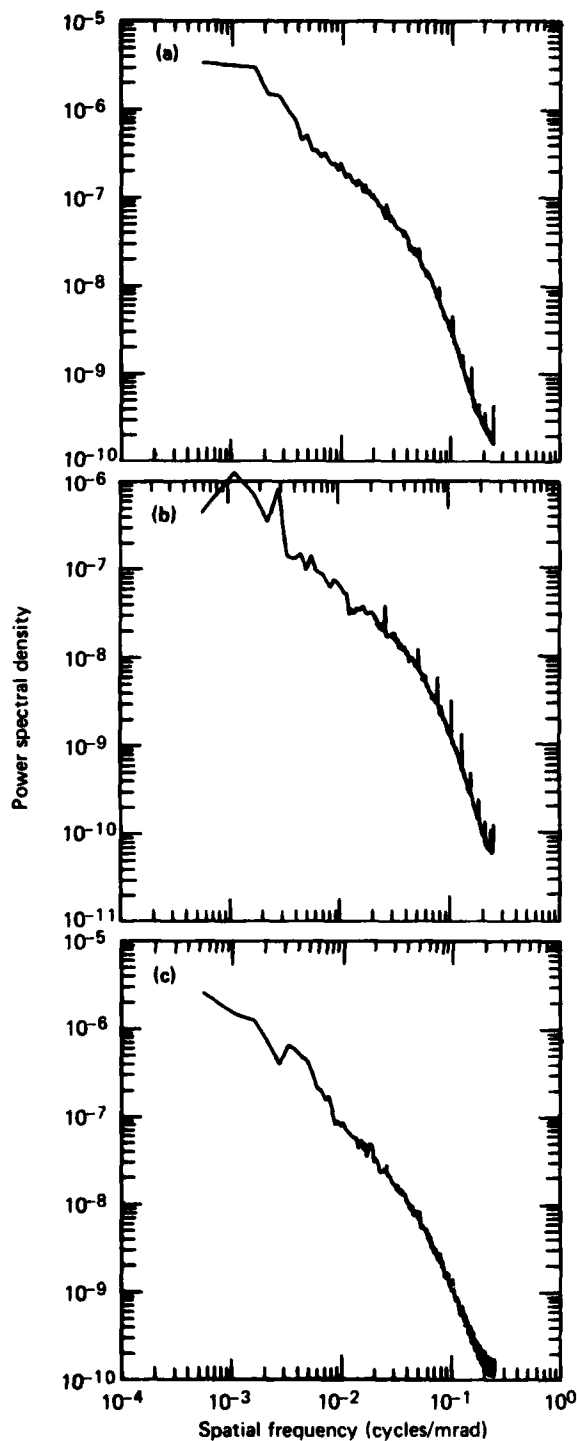


Figure D-5 Power spectral densities of ERIM scenes of Camp A.P. Hill, 8.0-14.0 μm spectral band. (a) Morning (S01CH3). (b) Afternoon (S02CH3). (c) Evening (S03CH3).

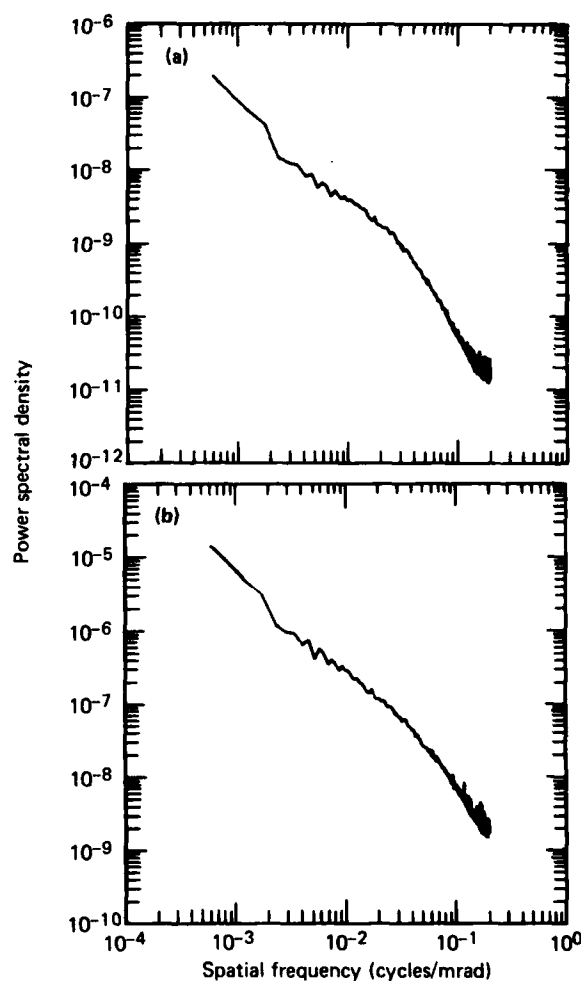


Figure D-6 Power spectral densities of ERIM scenes of Port Hueneme (port and water). (a) 4.5-5.5 μm spectral band (S23CH3). (b) 9.0-11.4 μm spectral band (S23CH4).

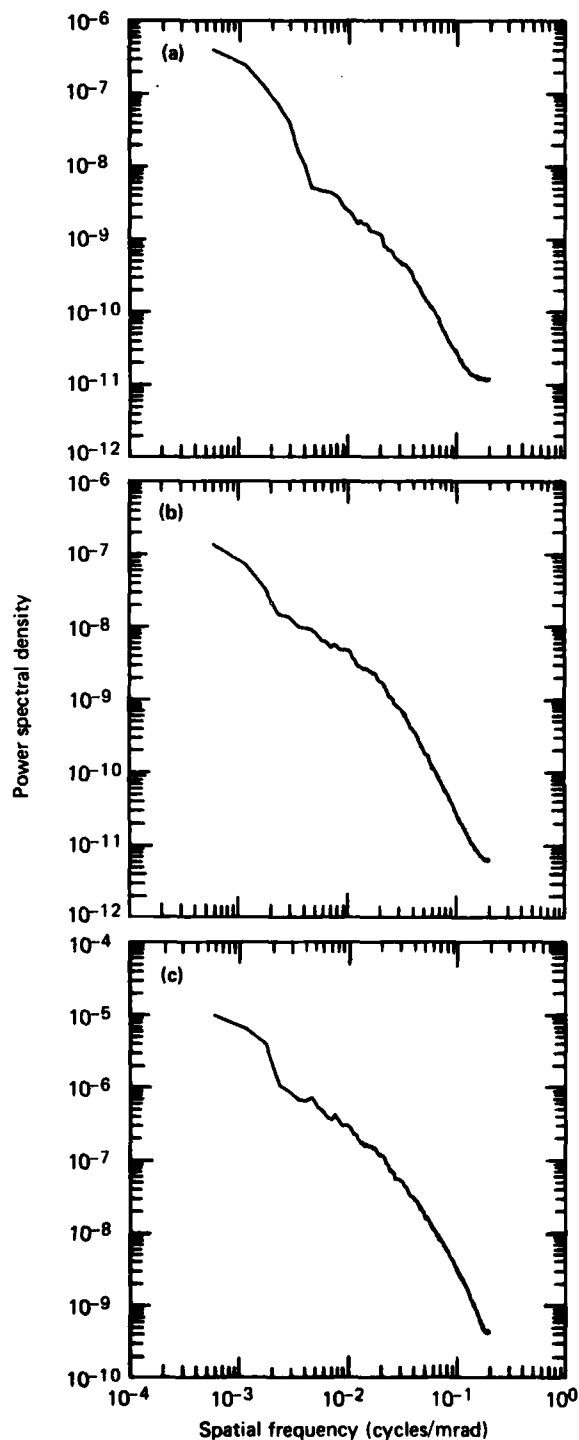


Figure D-7 Power spectral densities of ERIM scenes of Port Hueneme (port, water, and sun). (a) 2.0-2.6 μm spectral band (S24CH1). (b) 4.5-5.5 μm spectral band (S24CH3). (c) 9.0-11.4 μm spectral band (S24CH4).

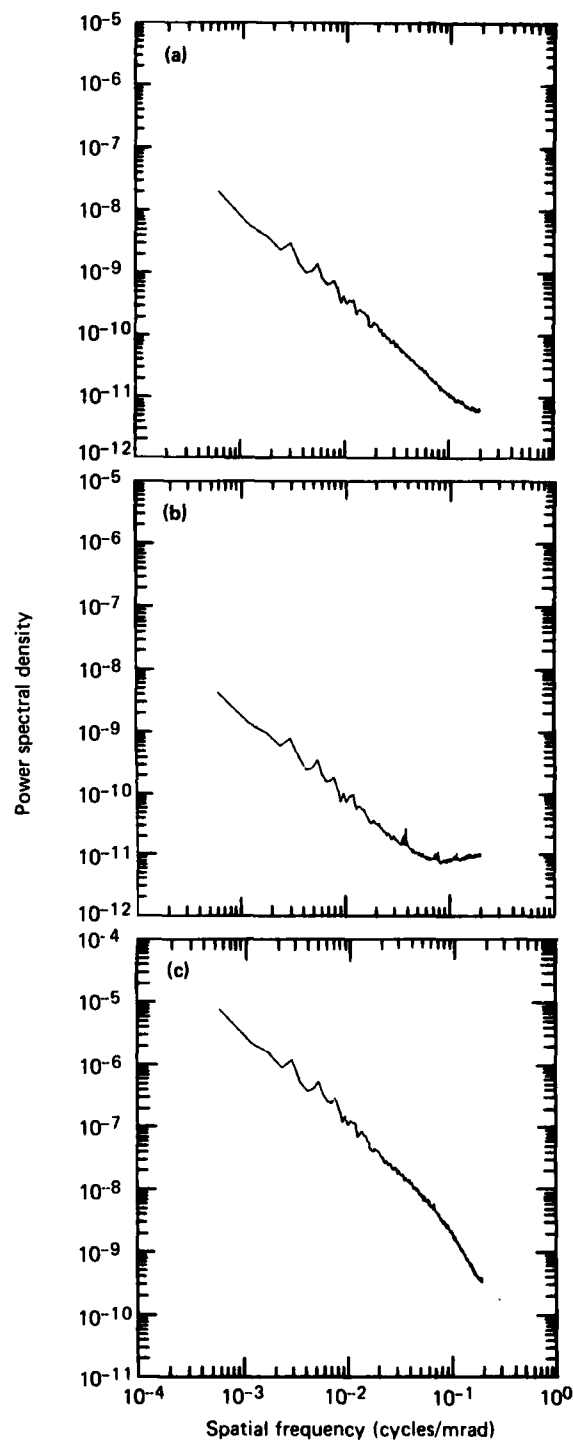


Figure D-8 Power spectral densities of ERIM scenes of mountains near Nellis AFB (F08). (a) Channel 1 (3.9-4.7 μm). (b) Channel 2 (3.5-3.9 μm). (c) Channel 3 (9.0-11.4 μm).

Appendix E

Power Spectral Density of Filtered Scenes

PSDs of many of the filtered scenes are included in this appendix. The BMAP plot is of the scene after a bandpass filter was applied. This PSD looks like a low-pass filter.

The AFGL and ERIM scenes have been filtered with

a high-pass filter. These plots show that the AFGL PSDs were approximately flattened by the filtering. The ERIM1 scenes are not nearly as flat as the AFGL PSDs. The ERIM3 and ERIM5 PSDs, however, were flattened by the filtering.

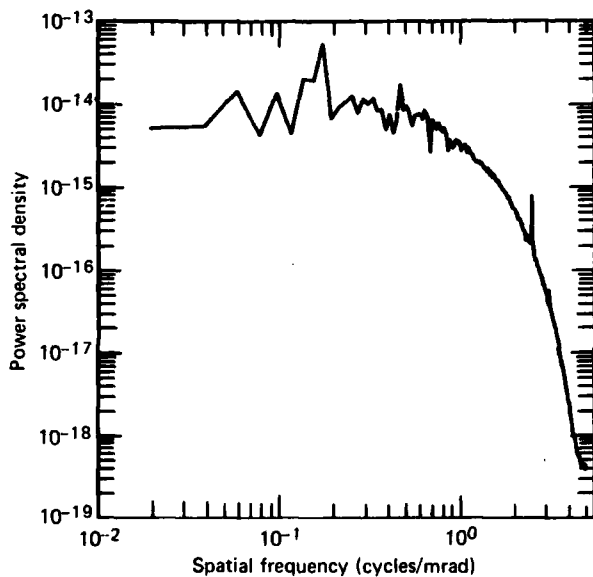


Figure E-1 Power spectral density of BMAP mid-IR scene from Montauk Point after bandpass filter.

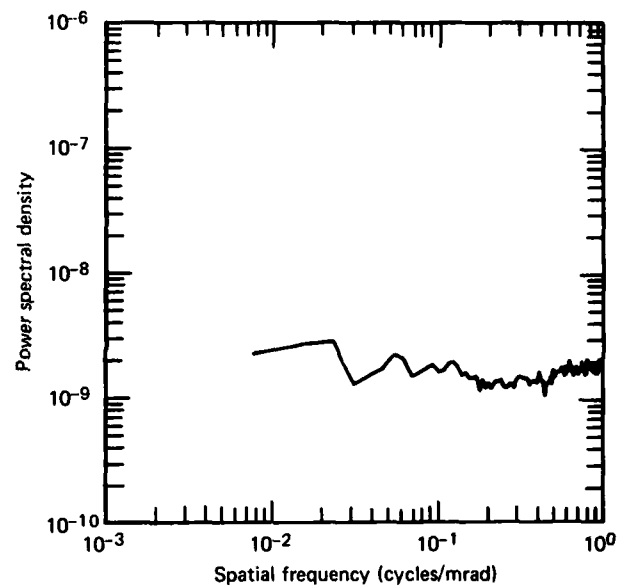


Figure E-2 Power spectral density of AFGL terrain scene (104) after high-pass filter.

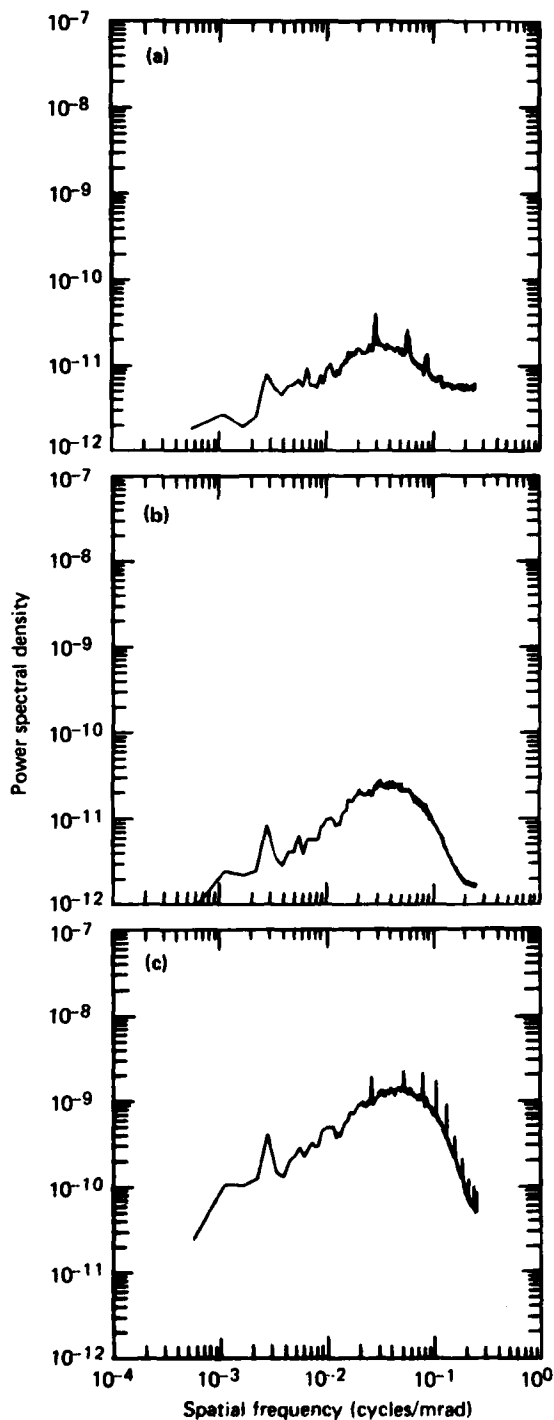


Figure E-3 Power spectral densities of ERIM afternoon scene of Camp A.P. Hill after high-pass filter. (a) 2.0-2.6 μm spectral band (S02CH1). (b) 4.5-5.5 μm spectral band (S02CH2). (c) 8.0-14.0 μm spectral band (S02CH3).

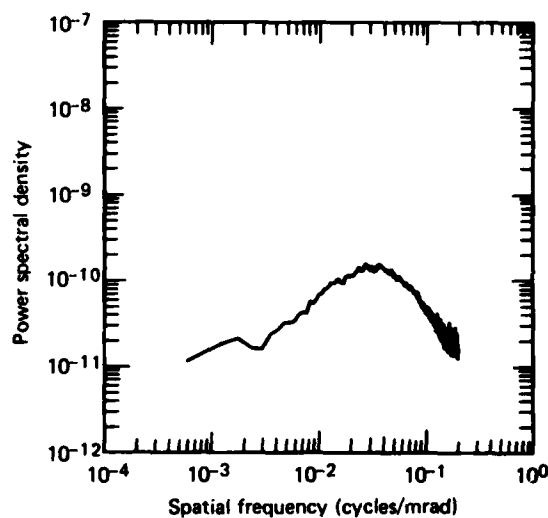


Figure E-4 Power spectral density of ERIM scene of Port Hueneme, spectral band 4.5-5.5 μm , after high-pass filter (scene S23CH3).

INITIAL DISTRIBUTION EXTERNAL TO THE APPLIED PHYSICS LABORATORY*

The work reported in TG 1360 was done under Navy Contract N00024-85-C-5301 and is related to Task A3DO, supported by Naval Surface Weapons Center.

ORGANIZATION	LOCATION	ATTENTION	No. of Copies
DEPARTMENT OF DEFENSE			
Secretary of Defense Defense Technical Information Center	Washington, DC 20301 Alexandria, VA 22314	G. C. Kopesak, OUSDRE (ET) Accessions	1 12
DEPARTMENT OF THE NAVY			
CNO	Washington, DC 20350	OP 98 OP 983 OP 987 OP 987B OP 35 OP 35E OP 352 OP 352L OP 355 OP 355W OP 507D	1 1 1 2 1 1 1 1 1 1 1
Office of the Assistant Secretary of the Navy (RE&S)	Washington, DC 20350	Edward Donalson Charles Kincaid J. R. Whalen R. L. Rumpf Ann Berman T. A. Jacobs	1 1 1 1 1 1
NAVSEASYS COM	Washington, DC 22202	SEA 06 SEA 06A SEA 06AT SEA 06AX SEA 06P SEA 06R SEA 62 SEA 62B SEA 62D SEA 62D1 SEA 62D2 SEA 62D22 SEA 62D3 SEA 62D4 SEA 62D52 SEA 62Z SEA 62Z1 SEA 62Z2 SEA 62Z3 SEA 62Z3B SEA 62Z31 SEA 62Z31F Lib., SEA 9961 PMS 400 PMS 400B	1 1 1 1 1 1 1 1 2 2 2 1 1 1 1 1 1 1 1 1 2 1 2 1 1
NAVAIRSYS COM	Washington, DC 22202	AIR 320 AIR 320B AIR 320D AIR 320R AIR 06 AIR 0623 Lib., AIR 7226	1 1 1 1 1 1 2
NAVPRO	Laurel, MD 20707		1
Naval Surface Weapons Center	Dahlgren, VA 22448	NSWC/DL D2W NSWC/DL G06 NSWC/DL G21 NSWC/DL G22 NSWC/DL G24 Library NSWC/VO G40 NSWC/VO K22 NSWC/VO N12 Library	1 1 1 1 1 2 1 1 1 2
	White Oak, MD 20903-5000		
Requests for copies of this report from DoD activities and contractors should be directed to DTIC, Cameron Station, Alexandria, Virginia 22304-6145 using DTIC Form 1 and, if necessary, DTIC Form 55.			

*Initial distribution of this document within the Applied Physics Laboratory has been made in accordance with a list on file in the APL Technical Publications Group.

INITIAL DISTRIBUTION EXTERNAL TO THE APPLIED PHYSICS LABORATORY

ORGANIZATION	LOCATION	ATTENTION	No. of Copies
Naval Weapons Center	China Lake, CA 93555-6001	3906 3921 3941 3942 3854 Library	2 1 1 1 1 1
Office of Naval Technology	Arlington, VA 22209	ONT 07C ONT 0712 ONT 0713	1 1 1
Pacific Missile Test Center	Pt. Mugu, CA 93042	4045	1
U.S. Naval Academy	Annapolis, MD 21402	Dir. Research	2
DEPARTMENT OF THE ARMY			
Missile Command	Redstone Arsenal, Huntsville, AL 35898	DRSMI OD DRSMI RR	1 1
Ballistic Missile Defense Advanced Technology Center	Huntsville, AL 35807	ATC-0 Gene Tidwell, SDC-HEDI Claud E. Martin, DASD- H-4B Tony Street, DASD- H-WK Price Boyd, DASD-H-WK	1 1 1 1 1 1
DEPARTMENT OF THE AIR FORCE			
Air Force Armament Division	Eglin AFB, FL 32542	AD/XRG	1
Aeronautical Systems Division	Wright-Patterson AFB, Dayton, OH 45433	YYM	1
CONTRACTORS			
Acurex Corporation Aerojet Electro Systems Co. Coors Porcelain Co. General Dynamics	Huntsville, AL 35806 Azusa, CA 91702 Golden, CO 80401 Pomona, CA 91766	F. Strobel Irwin Weiss D. Roy H. J. Meltzer R. M. Pietrasz R. Parker J. Stamper W. H. Rhodes R. R. Miller A. V. Funari Dennis Quan R. L. Sendall Richard Murray John Sura A. E. Davidoff J. F. Reilly L. B. Anderson A. E. Franz R. L. Gentilman	1 1 1 2 1 1 1 1 2 1 1 1 1 2 1 2 1 2 1
GTE Laboratories, Inc. Hughes Aircraft Co.	Waltham, MA 02254 Canoga Park, CA 91304		
Martin Marietta Corp.	Orlando, FL 32805		
McDonnell Douglas Aircraft Co. MIT Lincoln Laboratories Raytheon Corporation Raytheon Corporation Research Div.	St. Louis, MO 63166 Lexington, MA 02173 Bedford, MA 01730 Lexington, MA 02173		

END

5-87

DTIC